Politecnico
di Torino

Numerical-Experimental Modelling of a Vertical Axis Wind Turbine

Author:
Simone Martelli - 305988

Supervisors:
Prof. Gaetano Iuso
Prof. Gioacchino Cafiero

Ingegneria Aerospaziale - Aerogasdinamica

DIMEAS
Politecnico di Torino

December 2025

Contents

1. Introduction

In the last 30 years the need to transition away from fossil fuels towards more environmentally sustainable methods of energy production has become apparent.

The last decade saw a doubling in the production of energy from renewable sources[13]. While hydroelectric generation remains the principal source of green energy, there's also been an increase in interest in wind power generation. This is principally due to lower environmental impact and the wide availability of wind. The majority of installed wind power comes from Horizontal Axis Wind Turbines (HAWT), typically installed in onshore wind farms. While these are fairly efficient machines, they have some drawbacks, namely the relatively high environmental impact, both in terms of noise and disturbance to the ecosystem, and high costs, upfront and for the up-keep over the service life, due to the size and geometry of the devices. Finally, HAWT can't be installed anywhere: indeed the mode of operation of the device requires a fairly constant wind direction in the zone of installation; while yaw control devices can be installed, these become increasingly complex and difficult to install, other than constituting an additional point of failure, as the size of the machines grow.

Due to these difficulties, in the first half of the last century a new class of devices for wind power extraction started to developed: the Vertical Axis Wind Turbine (VAWT). This type of machine has the benefit of being omnidirectional, thus eliminating the need for yaw devices and the impossibility of production in case of wind in unfavourable directions, and has significantly lower costs of production and maintenance, by virtue of the geometry of the turbine: the vertical axis of rotations removes the need to install a raised generator; instead it can be placed directly on the ground even in the case of large turbines.

In general VAWT have lower efficiency compared to HAWT, this is however not a drawback: VAWT and HAWT are not aimed at the same market; while HAWT are used for large energy production, VAWT are born with small scale production in mind, indeed their main use could be in off-grid power generation, in conjunction with other renewable sources and accumulation devices.

The main drawback of VAWT is intimately tied with its most prominent characteristic: while the polar symmetry of the devices makes them insensible to wind directions, it also implies a complicated flow field: the flow that wets the blades is highly unstationary, with complex flow phenomena such as dynamic stall, boundary layer transition and separation, oscillating angles of attack and of course the fact that each blade is always in the wake of the preceding one. For all these reasons turbulence is prominent in the flow field and therefore its accurate simulation is essential. This makes the simulation of VAWT with reduced-order methods very complicated and obtaining accurate results with them is nearly impossible.

Even when using finite-volumes methods (FVM) to discretize the full system of balance equations, results are not always satisfactory: indeed there are differences in numerical studies and they are concerned mainly with 2D simulations. While a bi-dimensional

simulation is easier to set-up and requires less computational power, they are intrinsically flawed: the object of study is fully tridimensional with important finite aspect-ratio effects and, as said before, turbulence is predominant in the flow field. However, it should be reasonable that in case of turbines with straight blades, and structs placed on their extremity, a 2D simulation could accurately predict the flow field on the mid-plane of the turbine where extremity effects should be negligible.

The aim of this thesis is then to use computational fluid dynamics (CFD) to investigate the aerodynamic behaviour of a Vertical Axis Wind Turbine and to compare this results with those obtained with low-order methods, using the experimental data as an important baseline in evaluating accuracy.

Firstly a review of existing literature will be conducted to find what the consensus is on the computational settings and to compare various methodologies.

An overview of the experimental campaign is presented with the acquired data, this will then be compared with the results obtained with the low-order method implemented in the software QBlade.

Then a 2D set-up will be implemented and validated against available experimental data. Once all simulation parameters are correctly calibrated, a series of 2D simulations will be carried out in order to have a first estimate of the turbine's performance.

1.1. Concerning VAWTs

Several types of VAWT have been developed over the years, the principal division accounts from the mechanism used to extract energy from the wind:

- Savonius Turbine: these drag-based devices have all the benefits of VAWT, while also allowing for an efficient self starting behaviour and increased simplicity. This all comes at the cost of reduced efficiency;
- Darrieus Turbine: this second class of VAWT uses lift, or better tangential force, on the blades of the turbines, which are therefore shaped like airfoils, to convert wind energy in rotational energy. Although they are more efficient, they are significantly more difficult to manufacture because the geometry requires more in-depth studies.

(a) Savonius-type Turbine

(b) Eolito's Darrieus Turbine

(c) Hybrid configuration

Figure 1.1.: Examples of various VAWT configurations

Several types of Darrieus turbine have been studied and produced. The simplest one is the *H-Darrieus* where the blade are straight; to reduce the limitations of this type of turbine, solutions with *helical* blades have been studied: while the curved blade is significantly more aerodynamically efficient, after all the blade can be swirled along its length in order to optimize the angle of attack, this type of turbine presents complications from a structural point-of-view and is difficult to build. There are also hybrid turbines where a Savonius-type turbine is placed on the shaft of a Darrieus rotor in order to mitigate the self-starting difficulties presented by the latter type.

Since we're interested in the study of a Darrieus H-type turbine this section will briefly present their operating principle.

In studying VAWT behaviour, the correct control parameter to employ is the Tip-Speed Ratio (TSR),

$$\lambda = \frac{\omega r}{V_\infty},$$

where:

- ω is the rotational speed of the turbine;
- r is its radius;

- V_∞ is the undisturbed wind speed;

The product ωr therefore represent the tangential speed of the blade and is termed *Tip Speed*.

The Reynolds number is not used because it's difficult to determine which velocity to use: the wind speed, while significant, does not uniquely determine the flow field, i.e.: a turbine rotating at $100RPM$ will have a drastically different behaviour from one with a rotational speed of $200RPM$ even tough the local Reynolds number may coincide. The relative speed could be a better parameter but that in turn depends on freestream velocity, TSR and, more importantly, on the angular position θ. It is then evident how the Reynolds number varies heavily during a full revolution. This is in part the root cause of the aforementioned complications: since the Reynolds on the blade varies continuously so does the behaviour of the flow on the blades. Therefore the TSR is used as control parameter for the global behaviour of the turbine while the Reynolds number remains important only for fluid dynamics, and even then only locally.

As said before, the resulting force on each blade is decomposed in tangential, F_t, and radial, F_r, components rather then the usual lift and drag. This decomposition is more useful in determining the resulting torque on a single blade, it can be computed simply as

$$\vec{T_b} = \vec{r} \times \vec{F_t},$$

while the radial component results only in dynamic loading on the structure. It is then evident that a well designed turbine should maximize the tangential force while limiting the radial one. Given the polar symmetry of the system and the instantaneous variation of the tangential force, it's more useful to consider the *average* tangential force during a revolution and then using this value to compute the total torque per revolution as

$$\vec{T} = n\vec{T_{ave}},$$

where n is the number of blades.

To better understand the dynamic behaviour, an illustration of the blade in a generic position θ is reported in Fig. 1.2.

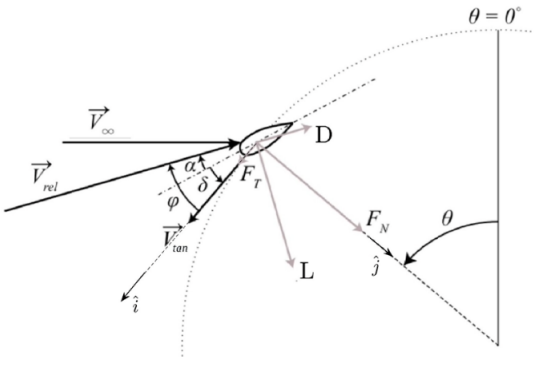

Figure 1.2.: Free-body diagram of the blade in position θ.

It is evident how the relevant aerodynamic velocity is a vectorial sum between the wind velocity and the tangential velocity of the blade due to rotation. Since the direction of the latter velocity changes instant by instant, so does the angle of attack. In fact it can

be shown that

$$|\vec{V_{rel}}| = V_d\sqrt{\left(\frac{V_\infty}{V_d}\lambda + sin(\theta)\right)^2 m + cos^2(\theta)}$$

where V_d is the speed at the turbine disk, altered from the freestream value due to the disturbances caused by the turbine and the extraction of energy. Finally the angle of attack can be computed as

$$\alpha = arctan\left(\frac{cos(\theta)}{\frac{V_\infty}{V_d}\lambda + sin(\theta)}\right) + \delta$$

where δ is the incidence of the blade. (See Fig. 3.1)

As is always the case in fluid dynamics, it is preferred to use adimensional coefficients instead of dimensional quantities because data reported in this way has wider applicability. Then the relevant parameter in VAWT is not the net torque but rather the power coefficient:

$$C_p = \frac{P}{\frac{1}{2}\rho S V_\infty^3}$$

where P is the net power extracted by the turbine during a revolution $P = \vec{T_{ave}} \cdot \vec{\omega}$ and therefore relates the extracted power to the total available wind power. It has been shown by Betz[7] that this coefficient has an upper limit of $\frac{16}{27} \approx 0.59$.

2. Literature Review

A review of existing literature has been conducted in order to evaluate the current state of simulations and experiments on VAWT. While there's certainly been an increased interest in VAWT, there's nowhere near the amount of data available for HAWT.

Nevertheless, several analysis have been conducted in recent years studying the behaviour of VAWT using CFD, with 2D[1], 2.5D[2] and 3D domains. A general consensus on the use of RANS over LES has been observed; while He et al. [12] showed that, especially for low TSR cases in 2.5D, LES results show greater agreement with empirical data, this comes at a greater computational cost and overall simulation complexity. It must be brought to attention that the authors used the two-equations SST (Shear-Stress Transport)[3] model in their simulations. In fact, several articles [6, 9, 26] investigated different turbulence models and confronted them with experimental data: all agree that the Transition SST model gives the most accurate results although Barnes et al.[6] found that there still is a significant inaccuracy in the prediction of the flow field both in the immediate vicinity of the blades and in the turbine's wake. It must be kept in mind that the model also has increased computational cost due to the higher number of equations to solve.

Franchina et al. [10] conducted a numerical study both in 2D and 3D. They found that at lower TSRs (λ <2.4) bi-dimensional simulations underpredict the value of C_p while the opposite is true for higher values of λ. On the contrary the curve $C_p(\lambda)$ obtained from 3D simulation follows the same pattern of the experimental data. It can also be observed how the difference between 2D and 3D results grows with the TSR; this can be explained by the importance of dynamic effects on lower TSRs compared to extremity effects. They also found that two-equation turbulence models are not adequate in simulating low TSR conditions (namely $\lambda = 1.5$) due to the importance in those cases of flow separation.

Balduzzi et al. [2] conducted a thorough numerical study on the effects of several computational settings and validated their results with wind tunnel data. A similar study was conducted by Rezaeiha et al. [27]. Balduzzi found a direct proportionality between time-step and revolution speed, while Rezaeiha indicated two-different time-steps for different operating conditions. In summary, Balduzzi reported that, for $\lambda = 2.2$, a time-step corresponding to $\Delta\theta = 0.27°$ is sufficient as further refinements resulted in no variation; they suggested that further analyses should conduct a sensitivity analysis on the time-step in order to find the optimal value that maximises accuracy and minimises computational cost. On the other hand, Rezaeiha suggests $\Delta\theta = 0.1°$ for low TSR regimes

[1] In the following section, D is employed at times for dimension, others for the diameter of the turbine. As is evident which of the two cases should be considered, further clarification is not given for the sake of brevity.

[2] 2.5D are properly 3D simulations but they do not investigate the full domain thus reducing the computational cost. They instead typically simulate only a section of the blade, typically reported in multiples of chord length.

[3] see Section 3.3

($\lambda < 2.4$) while $\Delta\theta = 0.5°$ is sufficient in case of higher revolution speeds.

Rezaeiha suggests a significantly smaller computational domain, both spatial and temporal. Indeed Balduzzi suggests a spatial domain of $140D \times 60D$ while Rezaeiha found a $35D \times 20D$ domain to be sufficient. On the same note, Balduzzi imposes a stricter convergence criterion: while the general consensus for convergence is a difference in torque inferior to 1% between subsequent revolutions, they report an error of 9% relative to the final value (after 100 revolutions) when this threshold is met, therefore they suggest a delta inferior to 0.1%. On the contrary, Razaeiha reports $20 - 30$ revolutions to be sufficient in every operating condition.

Recently Barnes et al. [5] and Li, Yang, Feng et al. [17] conducted a survey of available literature and presented a summary of the computational settings employed. Here are reported the recommended numerical settings as found by Barnes

Turbulence Model	IDDES or k-ω SST
Pressure-Velocity Coupling	Coupled
2D or 3D Analysis	3D
Inlet Length	20D
Outlet Length	40D
Blockage Ratio	2.5%
Rotational Domain Diameter	1.25D
Rotational Step(2D)	0.25°
Rotational Step(3D)	1.2°

Li, Yang, Feng et al. instead limit themselves to a simple report of the literature, however some trends can be extrapolated:

- for the pressure-velocity coupling the SIMPLE algorithm is found to be the most widely used;
- domain dimension is highly variable and dependent on operating conditions, however positioning the inlet 15D upstream and the outlet 30D downstream seem to be sufficient for every situation;
- for the time-step, they confirm what was found by Balduzzi et al. [2] and Rezaeiha et al. [27], however they consider a timestep of 1° to be sufficient for TSRs higher than 3.3;
- concerning the turbulence model, like Barnes et al. [5], they found that IDDES and k-ω SST give the best results overall.

Across all examined studies there is agreement on the use of $2nd$-order discretization both in time and space, with $1st$-order discretization being used for a faster initialization of the solution. For temporal discretization, an unsteady implicit approach is almost always employed, Concerning the computational grid, a sensitivity analysis must be carried out in order to find the minimum allowable grid refinement that still gives accurate results. Due to the nature of the flow-field care must be given that the airfoils are discretized with an adequate number of points in order to accurately capture all dynamic

phenomena.

To summarize, a sensitivity analysis must be conducted in order to establish the appropriate grid-resolution and the maximum time-step employable. The flow field should be considered as incompressible, owing to the very low speeds involved, but there's not a definitive answer on the pressure-velocity coupling algorithm to employ; the majority of analyses were conducted with the SIMPLE algorithm, however in [2] it was proved how the Coupled approach is more robust and less sensitive to the internal time-step, allowing a reduction in inner iterations number. The PISO algorithm is generally considered not employable in this case. Concerning the turbulence model, the Transition SST model must be employed in order to have the best results.

For the computational domain, the geometry of the system imposes the use of an inner, rotating region where the rotor is situated; this region is typically a disk with an extension of $1.5D$ to $2D$. Barnes [6] suggests employing a ring instead of a disc in order to reduce mesh cell count without sacrificing accuracy. As a comparison of results between the two options was not reported, this choice must be correctly validated. The domain should be large enough in order to reproduce the flow-field as it would develop in an undisturbed situation, but in this case also there's not a real consensus on the minimum dimensions that would satisfy the requirements.

The majority of validations were conducted against the experiments of Tescione et al. [31] and Raciti Castelli et al. [8]. The former conducted an experimental campaign using Stereo Particle Image Velocimetry while the latter conducted a numerical study and used values of C_p measured in a wind tunnel for validation.

3. Numerical Simulation of VAWT

In simulating VAWT behaviour, the nature of the flow-field should be kept in mind in order to correctly choose the simulation set-up.

The flow is highly instationary and turbulence is predominant in the flow-field. This is mainly due to the oscillations of the apparent angle of attack of the rotating airfoil as seen in Section 1.1.

Plotting the resulting angle of attack, supposing $\lambda = 1.5$ and $\frac{V_d}{V} = 0.9$, results in:

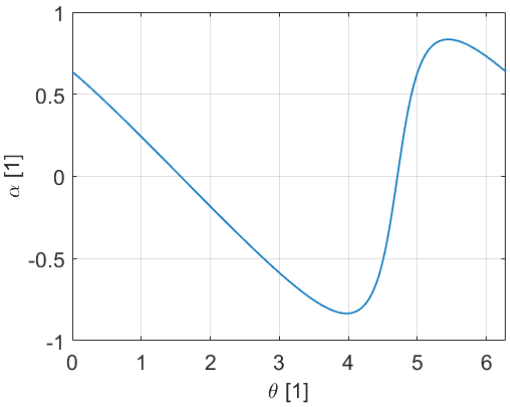

Figure 3.1.: Angle of attack during revolution

As can be imagined this variation induces periodic oscillations in the behaviour of air over the airfoil. Even considering this as one of the most critical cases, in fact the osciallatory behaviour is emphasized as the TSR lowers, qualitatively this is true in the full operating range of the turbine. Therefore, since the angles of attack go well past the stall point of the airfoil, flow separation should be expected with subsequent reattachments, thus causing dynamic stall. In conclusion the main flow field is highly turbulent.

This is not true locally, indeed another major problem is the phenomenon of transition: similar oscillations can be observed for the relative velocity, and therefore the airfoil Reynolds number. This causes the boundary layer to periodically transition from laminar to turbulent. This, coupled with adversed pressure gradients, further justifies separation.

On the other hand the low wind speeds at which VAWT are typically operated, usually around $10m/s$, allow for the usage of incompressible models; even accounting for the acceleration of the flow over the airfoil, its speed remains well below the incompressible limit. This simplifies the governing equations and therefore their numerical treatment.

Nonetheless, due to the turbulent nature of the flow field, an exact simulation, in the mathematical sense, would require direct discretization of the full balance equations on a scale small enough to capture at least the Taylor scale of turbulence. In practical applications this results in non feasible simulation times. Pope[25] estimates simulation times in the order of years for Reynolds numbers as low as 10^5. Even allowing for the

increased computational power in the last years, DNS (Direct Navier-Stokes) Simulations remain impractical for industrial applications.

In contrast, LES (Large Eddies Simulations) aim to leverage the nature of turbulence in order to reduce the computational cost. As shown by Kolmogorov[15], at small enough scales turbulence is isotropic and shows *universal* behaviour. Therefore LES solvers apply a spatial filter in order to cut all length scales below a specified threshold and simulate the resulting filtered equations. There remains a non-linear term in the equations, namely $u_i\bar{u}_j$[1]. This term, in theory, requires the unfiltered velocity field. To supplant this need Sub-Grid Scales models have been developed that, as the name suggests, compute this term for scales lower than the simulation Δx. As seen in Section 2, LES models can achieve higher accuracy but are still computationally intensive, especially in external flows.

For this reason RANS (Reynold-Averaged Navier-Stokes) are usually preferred in the simulation of turbulence. In contrast to the filter employed in LES, RANS resort to averaging of the flow-field. In principle this is an ensemble average, as in a value averaged over a certain number of experiments, that results in the Reynolds decomposition

$$W(x,t) = \bar{W}(x,t) + w(x,t),$$

where $\bar{W}(x,t)$ is the averaged value of a generic variable while $w(x,t)$ represents the instantaneous fluctuations around the averaged value.

Both LES and RANS sacrifice accuracy for reduced computational cost. Even with the added complications, such as the SGS models for LES, they allow to simulate industrial flow-fields with reasonable accuracy in engineering applications. Since RANS will be used in the simulations, further information on them will be given in the next sections.

3.1. Low-order models

While computational fluid dynamics offers significant accuracy, its high computational cost makes it impractical in some applications, especially in preliminary design where multiple configurations need to be evaluated. On the other hand, low-order methods allow the simulation of various configurations in a relatively small amount of time. Obviously these results shouldn't be taken as quantitative and instead have only qualitative value.

Several low-order methods have been developed for the study of wind turbines, from the Blade Element Model, which has been widely used since its inception in 1878 by Froude[11], to the more recent DMS[4]. These methods, while useful in view of their reduced computational cost, lack a physical connection with the real problem by virtue of their numerous assumption. This led to the necessity of developing a more accurate model for the study of wind turbines. In 2016 Marten et al. [19] introduced a Lifting Line-Free Vortex Model within the software QBlade, developed at the Chair of Fluid Dynamics at the Technical University of Berlin.

This models simulates the blade as a lifting line located at the quarter chord point, similarly to Prandtl's method; in each time-step an iterating algorithm computes the converged circulation distribution on the lifting line that results in the available lift and drag coefficients for the effective angle of attack and local Reynolds number. In practice

[1]Standard Einstein notation, the repeated indices signify a sum over all available indices

this corresponds in obtaining the correct $\partial\Gamma$ in

$$\partial C_L(\alpha) = \rho V_{rel} \times \partial\Gamma,$$

where V_{rel} is the vectorial sum of the free-stream velocity, the motion of the blade, and the induced velcity,

$$V_{ind}(x) = -\frac{1}{4\pi}\int \Gamma \frac{r \times \partial l}{r^3},$$

which accounts for the contribution of all vortex elements. After convergence is reached, the rotor is rotated and the vortices on the trailing edge are convected in the wake with a certain velocity, dependent on the chosen method. This allows a more sound physical modelling whilst maintaining acceptable simulation times. The algorithm is modifiable, allowing the selection of various modelling solutions depending on the configuration to be studied and the desired compromise between simulation accuracy and cost, e.g.: integration can be done with a simple first order Euler method or a second order predictor corrector. More informations are given in Section 5.1 where the selected models are discussed.

3.2. Reynolds-Averaged Navier Stokes

Since we've concluded that the equations of motion can be considered in their incompressible form, we will consider only this form of the balance equations.

Both mean and fluctuating field are solenoidal for the mass balance and, substituting in the continuity equation, the final RANS equation can be obtained as

$$\nabla \cdot \bar{U} = 0.$$

Taking the mean of the Navier-Stokes equation is less simple due to the convective terms. These are non-linear and represent the major problem in simulating RANS equations. In any case, as shown in [25], the resulting mean-momentum equation is

$$\frac{\partial \bar{U}_j}{\partial t} + \bar{U}_j \cdot \frac{\partial \bar{U}_i}{\partial x_i} = \nu \nabla^2 \bar{U}_j - \frac{\partial u_i \bar{u}_j}{\partial x_i} - \frac{1}{\rho}\frac{\partial \bar{p}}{\partial x_j}.$$

This is formally equivalent to the Navier-Stokes equation but for the covariance terms making the system unclosed. Just as in LES, the exact computation of this term requires the complete velocity field. A correct simulation of the convariance terms is then at the heart of any RANS model in order to close the system and the different strategies employed identify the different models.

3.2.1. Reynolds' stresses

The covariance terms are also given the name of Reynolds stresses and can be determined either by a transport equation or by employing the turbulent viscosity hypotesys. According to this hypotesys, Reynolds stresses can be computed as

$$u_i \bar{u}_j = \frac{2}{3} k \delta_{ij} - \nu_T \left(\frac{\partial \bar{U}_i}{\partial x_j} + \frac{\partial \bar{U}_j}{\partial x_i} \right),$$

now, if ν_T is known throughout the flow-field, the system is closed. By itself, for the majority of flow-fields the accuracy of the hypotesis is quite poor and requires flow-dependent variables rendering the implementation of a general model complicated.

Therefore several models have been developed in order to limit the downsides of the hypotesis and obtain complete models, where flow-dependent specifications are not required. These are all at least *2-equations* models and they allow the computation of length- and time-scale and a viscosity.

The first succeful model, developed in the 70s by Jones, Launder and Sharma[1, 14] is the $k-\epsilon$ model. As the name suggests, the model consists of two transport equations, one for the turbulent kinetic energy, k, and one for its rate of dissipation, ϵ. Finally, the model specifies the turbulent viscosity as

$$\nu_T = C_\mu \frac{k^2}{\epsilon},$$

where $C_\mu = 0.09$ is one of the model constants.[2]

Due to its semplicity in both nature and implementation, this model is present in virtually all CFD codes. While it is acceptably accurate for relatively simple flows, in more complex cases, especially wall-bounded ones, the computed flow-field is often even qualitatively incorrect, i.e. erroneous flow structures etc. This is mainly due to the behaviour in the near-wall region where the model isn't capable of correctly predicting the flow-field without changing some of the flow constants. For these reasons, over the years many modifications of the base model have been proposed with varying results. Even with wall treatements, the model performance remains non-satisfactory.

For this reason a second class of models have been developed where the second transport variable is chosen to be the specific rate of dissipation, ω. It must be noted how the equation for ω is implied by the ϵ equation. Notably, this choice was first proposed in Kolmogorov's 1942 paper. The modern implementation has been developed by Wilcox since 1988 and it's been an ongoing effort. While the results of this formulation are appreciably superior, especially in flows with stream-wise pressure gradients and in near-wall regions, it isn't free of limitations, the most important one being the necessity of a non-physical (non-zero) boundary condition on ω on non-turbulent boundaries, with the resulting flow-field being extremily sensitive to the imposed value.

Finally, in 1994, Menter proposed a combined model, aiming to leverage the upside of both models while eliminating the limitations.

3.3. SST Model

The original $k-\omega$ model as proposed by Wilcox[33] is formulated as follows:

- turbulent kinetic energy equation:

$$\frac{\partial}{\partial t}(\rho k) + \frac{\partial}{\partial x_j}(\rho u_j k) = \tau_{ij}\frac{\partial u_i}{\partial x_j} - \boldsymbol{\beta}^*\rho\omega k + \frac{\partial}{\partial x_j}\left[(\mu + \boldsymbol{\sigma}^*\mu_T)\frac{\partial k}{\partial x_j}\right],$$

[2] For details on the viscosity hypotesis and the $k-\epsilon$ model see Appendix A.1 and A.2

- specific dissipation rate equation:

$$\frac{\partial}{\partial t}(\rho\omega) + \frac{\partial}{\partial x_j}(\rho u_j \omega) = (\boldsymbol{\gamma}\omega/k)\tau_{ij}\frac{\partial u_i}{\partial x_j} - \boldsymbol{\beta}\rho\omega^2 + \frac{\partial}{\partial x_j}\left[(\mu + \boldsymbol{\sigma}\mu_T)\frac{\partial \omega}{\partial x_j}\right],$$

where the eddy viscosity, μ_T, is defined as

$$\mu_T = \boldsymbol{\gamma}^* \frac{\rho k}{\omega}.$$

Several closure coefficient are needed and are represented in bold in the preceeding equations. Wilcox gives values and justification for the values and his results are here summarised:

- $\gamma^* = 1$: this follows by a change of variable in the model's equations, namely $\omega^* = \omega/\gamma^*$. By inspecting the resulting equations, it can be observed how this rescaling is equivalent to setting this parameter as unity;
- $\beta^*/\beta = 6/5$: in the case of decaying, homogeneous, isotropic turbulence, the model's equations can be simplified as

$$\frac{\partial k}{\partial t} = -\beta^*\omega k \quad \text{and} \quad \frac{\partial \omega}{\partial t} = -\beta\omega^2,$$

  the resulting solution for k is $k \to t^{-\beta^*/\beta}$, from experimental observation, the exponent is 1.2;
- $\beta^* = 9/100$: this value is obtained by considering an incompressible, constant-pressure boundary layer and forcing the equations to follow the law of the wall results;
- $\gamma = \frac{\beta}{\beta^*} - \frac{\sigma\kappa^2}{\sqrt{\beta^*}}$ is obtained in the same line of reasoning;
- concerning σ and σ^* Wilcox wasn't able to find a satisfactory argument for their values; however they obtained $\sigma = \sigma^* = 1/2$ by brute-forcing the computations, indeed it appears that these values constitute a saddle point in parameter space and even small variations lead to pronounced deviations from the expected behaviour.

From this starting point, in 1994 Menter [21] introduced the Shear-Stress Transport method that greatly improves accuracy while maintaining a similar computational cost. The key concept is the use of a blending function, namely F_1, that serves as a switch between the two models, it is designed to be unity in the near wall region, where the ω formulation is employed, and 0 in the freestream where the ϵ formulation shows better performance. The function is then constructed as

$$F_1 = tanh(arg_1^4)$$

$$arg_1 = min\left[max\left(\frac{\sqrt{k}}{0.09\omega y}; \frac{500\nu}{y^2\omega}\right); \frac{4\rho\sigma_{\omega 2}k}{CD_{kw}y^2}\right]$$

For brevity's sake the definition of CD_{kw} is reported in Appendix A.3 along with the formulation of the transformed $k-\epsilon$ model employed(Appendix A.3.1).

After multiplying the transformed model by $(1 - F_1)$ and the $k - \omega$ model by F_1, the corresponding equations are then added togheter to arrive at the final model:

$$\frac{D\rho k}{Dt} = \tau_{ij}\frac{\partial u_i}{\partial x_j} - \beta^*\rho\omega k + \frac{\partial}{\partial x_j}\left[(\mu + \sigma_k\mu_t)\frac{\partial k}{\partial x_j}\right]$$

$$\frac{D\rho\omega}{Dt} = \frac{\gamma}{\nu_t}\tau_{ij}\frac{\partial u_i}{\partial x_j} - \beta\rho\omega^2 + \frac{\partial}{\partial x_j}\left[(\mu + \sigma_\omega\mu_t)\frac{\partial \omega}{\partial x_j}\right] + (1 - F_1)2\rho\sigma_{\omega 2}\frac{1}{\omega}\frac{\partial k}{\partial x_j}\frac{\partial \omega}{\partial x_j}$$

All the constants of the model are obtained with a similar principle, starting from the original models' constants, ϕ_i, the final value will be

$$\phi = F_1\phi_1 + (1 - F_1)\phi_2$$

Numerical values for the constants are also given in Appendix A.3.2.

More accurately, the model presented is defined as the Baseline Model by Menter, the SST model tries to bridge the gap between Reynolds-stress models, which account for the transport of the Reynolds stresses with a classic transport equation, and two-equation models which resort to the eddy-viscosity hypotesis. In the former, the stress are computed as $\tau = \rho a_1 k$, where a_1 is a constant, while the latter compute it as $\tau = \mu_t\Omega$, where Ω is the absolute value of vorticity. This last equation can be rewritten[20] as

$$\tau = \rho\sqrt{\frac{Production_k}{Dissipation_k}}a_1 k.$$

Unfortunately this leads to overprediction of τ in situations of adverse pressure gradiens. The remedy is then to redefine the eddy viscosity as

$$\nu_t = \frac{a_1 k}{max\left(a_1\omega; \Omega F_2\right)}.$$

The choice of F_2 limits this modification to wall-bounded flows while the original formulation is reteined in free-shear flows. The sole added cost of this method is the computation of the functions F_1 and F_2 which can however be done at the start and doesn't need to be updated as long as there are no grid deformations nor moving boundaries.

3.4. Transition modeling

Classical 2-equations models have significant difficulties in predicting transition due to the highly complex nature of the phenomenon and the moltitude of possible causes that can lead to transition. While there are several methods attempting to predict transition, they are either unsatisfactory, such as low-Reynolds models, using wall damping functions where transition is correlated to the viscous sub-layer formulation, or too complex to implement in general purpouse codes, such as experimental correlations, needing non-local values, which is incompatible with the parallel nature of modern commercial codes, and being case-dependent.

To avoid these problems, Menter[22] proposed a modification of the former model with two-additional equations, one for intermittency, γ, resposible for the transition modeling, and a second transport equation used to avoid non-local operations. It's important to

stress that this model does not attempt to model transition in a phyically sound manner but simply to implement correlation based models in a way that is compatible with commercial codes.

The basic idea is to use the vorticity Reynolds number,

$$Re_\nu = \frac{\rho y^2}{\mu}\frac{\partial u}{\partial y}$$

to trigger transition; this value needs only local properties and can therefore be computed for each cell without needing additional infromation. The value is then rescaled in order to have a maximum value of unity inside the boundary layer. This is done via the momentum thickness Reynolds number, Re_θ, so that

$$1 = \frac{Re_{\nu max}}{2.193 Re_\theta}.$$

When strong pressure gradients develop this relationship is no longer valid and instead becomes a function of the boundary layer shape factor, H; this is however used to advantage: it is shown how the increase in vorticity Reynolds number with increasing shape factor can be used to predict separation-induced transition.

3.4.1. Intermittency's transport equation

The formulation is such that the intermittency is set to 1 in the free-stream so that there's less interference with the turbulence model in stagnation regions and near the boundary layer edge[3].

The transport of intermittency follows

$$\frac{\partial \rho\gamma}{\partial t} + \frac{\partial \rho u_j \gamma}{\partial x_j} = P_{\gamma 1} - E_{\gamma 1} + P_{\gamma 2} - E_{\gamma 2} + \frac{\partial}{\partial x_j}\left[\left(\mu + \frac{\mu_t}{\sigma_f}\right)\frac{\partial \gamma}{\partial x_j}\right].$$

Terms with subscript 1 are transition source, while subscript 2 denotes destruction/relaminarization sources; they are defined as follows:

$$P_{\gamma 1} = F_{length}\rho S[\gamma F_{onset}]^{c_{a1}},$$

$$E_{\gamma 1} = c_{e1} P_{\gamma 1}\gamma,$$

where F_{length} contains the actual information about transition via correlations, while F_{onset} controls the intermittency production. Formulation for F_{onset}, along with a complete mathematical description of the model is reported in Appendix A.4. In any case, in the definition of F_{onset} is introduced $Re_{\theta c}$, the critical Reynolds number where intermittency starts to increase, this happens always upstream of the transition Reynolds number, and can be obtained via an empirical correlation, $Re_{\theta c} = f(\widetilde{Re}_{\theta t})$.

$$P_{\gamma 2} = c_{a2}\rho\Omega\gamma F_{turb},$$

$$E_{\gamma 2} = c_{e2} P_{\gamma 2}\gamma,$$

where F_{turb} disables the destruction terms outside of the laminar boundary layer. These

[3]In previous models γ was assigned a small value in the free-stream.

two terms ensure that intermittency remains null in a laminar boundary layer and allow to predict relaminarization.

3.4.2. Transition momentum-thickness Reynolds number's transport equation

As said before the Reynolds number of transition onset can be related with free-stream quantities via correlations. The main drawback is that the architecture of current commercial codes is such that accessing these values while evaluating cells in the boundary layer is computationally expensive. The aim of this equation is then to treat $Re_{\theta t}$ as a standard scalar variable, compute it in the free-stream and allow it to diffuse in the boundary layer so that it is readily available in each cell for the necessary computations. This diffusion is governed by

$$\frac{\partial \rho \widetilde{Re_{\theta t}}}{\partial t} + \frac{\partial \rho u_j \widetilde{Re_{\theta t}}}{\partial x_j} = P_{\theta t} + \frac{\partial}{\partial x_j}\left[\sigma_{\theta t}\left(\mu + \mu_t\right)\frac{\partial \widetilde{Re_{\theta t}}}{\partial x_j}\right].$$

The source term, $P_{\theta t}$ is designed to force the transported quantity, $\widetilde{Re_{\theta t}}$, to match the local value of $Re_{\theta t}$ and is defined as

$$P_{\theta t} = c_{\theta t}\frac{\rho}{t}\left(Re_{\theta t} - \widetilde{Re_{\theta t}}\right)\left(1.0 - F_{\theta t}\right).$$

Similarly to the preceeding equation, $F_{\theta t}$ turns off the source term in the boundary layer to allow the free-stream value to diffuse.

3.4.3. Model calibration

Evidently, the model is sensitive to a series of parameters and closure coefficients obtained by experimental correlation, and formulations for F_{length} and $Re_{\theta c}$ remain proprietary. Even with the result shown in[16], it stands to reason that the results of computations should be sensible to variations of some of these parameters. This can possibly account for the deficiencies reported in Section 2.

Indeed P.A.C. Rocha et al. in [29] and [28] showed how there is a significant improvement from the baseline model in the evaluation of C_p for HAWT and VAWT; this was achieved by changing the value of β^*. It must be noted however how this case is fundamentally different from the subject of study, both in geometry and TSR. It is expected that at lower λs the importance of this parameter should significantly decrease, due to the different nature of the flow-field.

From an analysis of the model and its parameters, the following ones are considered the most promising for calibration:

- a_1: this parameter directly influences both the turbulent viscosity and the shear stresses, therefore it seems reasonable that if could significantly modify the flow field;
- s_1: as described in Appendix A.4, this parameter controls the size of the separation bubbles. Since separation is one of the critical phenomena in the flow-field, if the computational results where not in accordance with experimental data with regard

to the shape and size of said bubbles, calibration of this parameter could lead to more accurate solutions;

- as explained in Section 3.3, the value of β^* follows from a fit to the law of the wall;
- $c_{\theta t}$ and $\sigma_{\theta t}$ control the production and diffusion, respectively, of the Critical Reynolds number. As explained, this is the quantity that governs transition; therefore if there's evidence of delayed or anticipated transition, tweaking these parameters could improve simulation quality.

The scarcity of empirical data however didn't allow for a correct and complete calibration of the model and this can therefore be the subject of a subsequent study.

4. Wind Tunnel Test

Having reached the end of the design process of the current prototype developed by Eolito Students Team, of which details are given in Section 4.1, it was decided to obtain empirical data about the performance of the turbine.

The test campaign was conducted in DIMEAS' Modesto Panetti Laboratory wind tunnel. Salient characteristics of the wind tunnel and a schematic are reported in Section 4.2.

The data acquisition chain and the control ones were thoroughly tested in order to guarantee both the safe operation of the turbine and the correct acquisition of data.

Control of the turbine was accomplished via the generator. As explained in the next section, the generator is coupled directly with the main shaft, thus rendering redundant the need for a gearbox, this allows to control the rotation speed of the turbine with a variable electrical load, a rheostat with a total capacity of $1kW$.

The three voltage signals from the generator are then rectified via external circuitry and sent to a data acquisition module. National Instruments' **NI 9215** was docked to **NI cDAQ-9174** which was them grounded and linked to a laptop running Matlab's **Data Acquisition App**, used both for storing the data and monitoring live signals.

NI 9215	
# of channels	4 differential
Resolution	$16bits$
Operational range	$-40° - 70°$
Input Range	$\pm 10.0V$
Error @ 25°	0.014%
Maximum polling frequency	$1e5Hz/channel$
Simultaneous sampling	Yes

The output signals were all voltage ones, the first two were then converted in effective voltage and current in the generator, while the last contained frequency data: using the generator internal geometry it was possible to find a correlation between the phase of this last signal and the number of revolutions. Correct operation of the entire chain was verified by linking it to a signal generator and an oscilloscope. Additionally, the correspondence between the effective number of revolutions and the data in output was tested via a photodetector.

Finally, voltage and current are multiplied to obtain the electrical power

$$P = Vi.$$

If the system is in equilibrium, reached before the acquisition begins, this is equivalent to the aerodynamic power that the rotor extracts from the airflow, once the mechanical and electrical efficiencies are accounted. Given that for the mechanical efficiency only rough

estimates are available without designing an additional test, and that the electrical one is dependent on the rotational regime of the generator and its voltage, for simplicity's sake the former was considered as an exact equivalency, so that

$$P_{aer} = Vi.$$

This of course results in lower values of C_p than the effective ones, but since we can expect that all values should be transformed by a roughly uniform scaling factor, we can infer that the qualitative behaviour of the turbine was correctly measured, even if quantitatively the numbers could be off by some percentage points. In any case this results in a conservative estimation of the performance and therefore can be considered an adequate result. Credit for the operation and realization of the control circuit goes to Eolito's Electrical Division, especially Davide Ferrero.

Once satisfied with the behaviour of the acquisition and control chains, the turbine was fully installed and the testing campaign begun.

After a couple of test runs, a redesign of the endplates was necessary as it was found that they could not withstand the centrifugal forces. Being 3D-printed, this was easily accomplished and a new, reinforced model was produced and installed. Credit for the design and printing of the endplates goes fully to Nicola Cardone.

During these test runs, the braking capacity of the system was tested, by increasing gradually the angular velocity of the rotor and then abruptly breaking. While the system was found to be adequate, a criticality was evidenced in the behaviour of the turbine: namely approaching $50Hz$ the central axis began a slight precession motion, the oscillations then decreased and re-appeared more strongly at around $100Hz$. It was concluded that this was clearly the result of a not accounted coupling between the aerodynamic forces and the natural frequencies of the structure. In order to preserve the structural integrity of prototype and wind tunnel both, it was decided to stop the tests and find a solution.

The prototype was then reassembled, having additional care for all alignments using laser pointers as evident in Fig. 4.1, and a third bearing was added in the lower part of the shaft with the hope of reducing oscillations. While these were clearly dampened by these measures, it was still found unsafe to increase the angular velocity over $125Hz$. This severely limited the ambit of the test, indeed we were able to obtain sufficient data in only one of the four test cases.

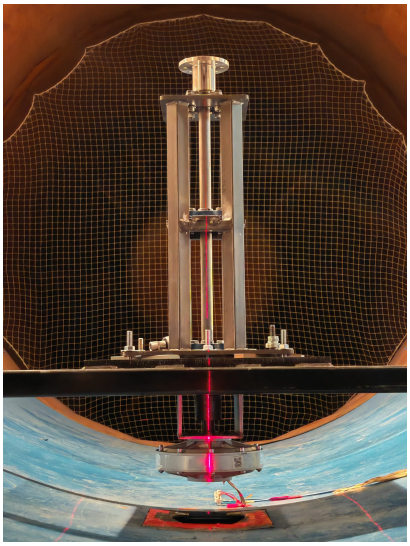

Figure 4.1.: Using a system of lasers, all relevant orthogonalities were verified

4.1. Eolito's wind turbine

The prototype of vertical axis wind turbine was entirely designed by Eolito Student Team. A simple configuration was chosen: being a still young project ease and speed for both design and realization of the prototypes were chosen instead of maximum performances. Indeed the prototype tested was the last of a chain of subsequent redesigns and small modifications.

The turbine is composed of three straight NACA 0024 blades with a chord of $0.257m$, orthogonal to the struts.

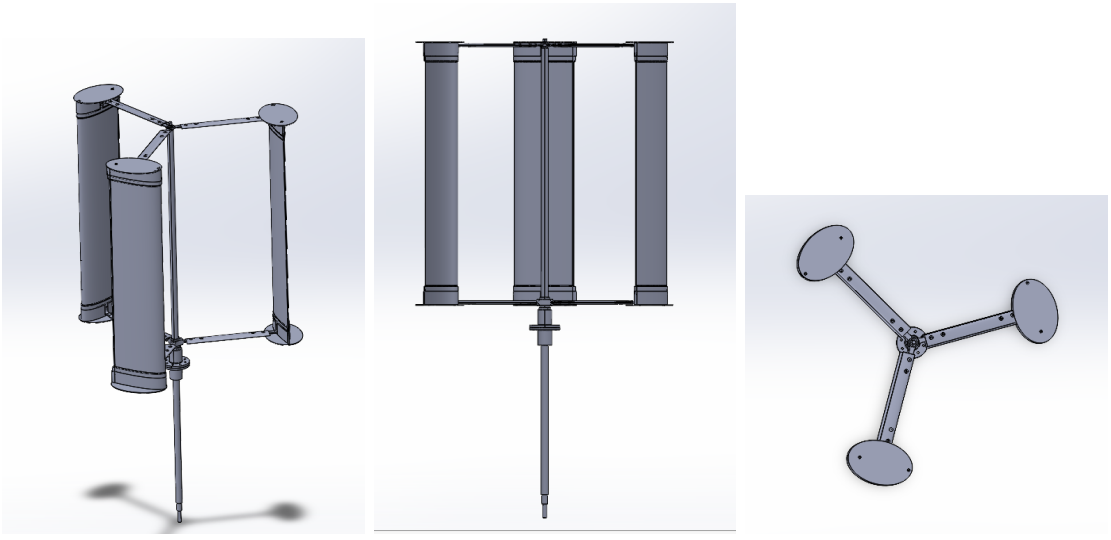

(a) 3D view (b) Lateral projection (c) Vertical projection

Figure 4.2.: Eolito's VAWT CAD

Type	H-Darreius
Profile	NACA 0024
Incidence	0°
Blade height	1.0m
Blade Chord	0.257m
# of blades	3
Radius[1]	0.515
Total height	2.15m

The rotor's central shaft is coupled with a secondary shaft that allows the aerodynamic surfaces to be further from the ground. This second shaft is then coupled directly with the generator. This has the main advantage of eliminating a possible point of failure, i.e. the gearbox, in the design and improving the maintainability of the turbine, but on the other hand requires a generator able to work at low RPMs This results in a higher initial cost for this component.

As can be seen in Fig 4.3, the turbine was anchored with a metal support, jointed at the test section walls. In turn this was coupled with the support structure of the rotor, on top, while the generator was attached from below with a specifically designed support.

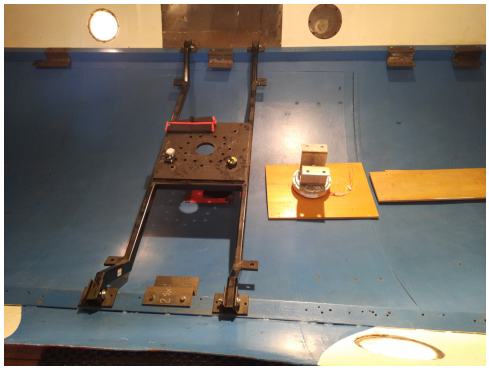

(a) Anchorage to the test section

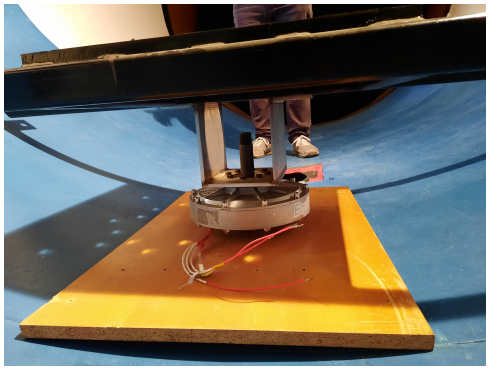

(b) Generator's support

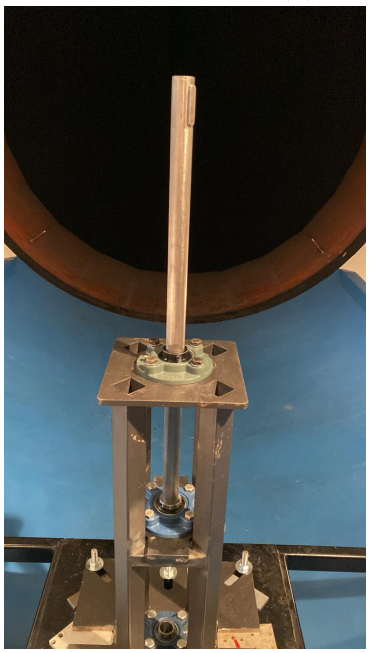

(c) Rotor' support structure: here is visible the central bearing added during the testing campaign

Figure 4.3.: Turbine installation

4.2. Wind Tunnel and test section

The measurement campaign was conducted in DIMEAS' D3M subsonic wind-tunnel. It's a closed-circuit design, driven by a 1MW fan, located directly after the test section for logistical reasons, capable of accelerating the flow to 90m/s in the test chamber. The test section has a diameter of 3m and a length of 5m with a small divergence to compensate for the boundary layer.

(a) Turbine as installed in the test section

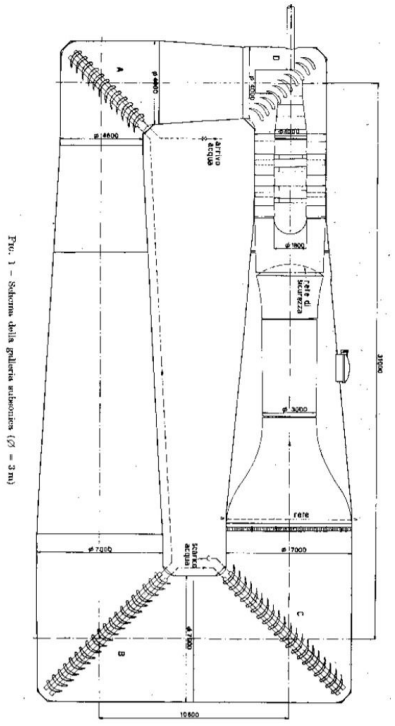

(b) Wind tunnel

Figure 4.4.: Experiment set-up

4.3. Results

Given the capabilities of the Data Acquisition Module, a polling frequency of $1000Hz$ was selected. This choice was guided by three main factors:

- the rectifying circuit has its own inertia, and extreme values may interfere with the proper pre-processing of the electrical signals;
- the need to store data from three channels in a multitude of tests;
- it was considered sufficient given the technical imposition of limiting the angular velocities: at a maximum of $120RPMs$ we can expect a revolution to occur in $0.5s$, thus resulting in 500 data points for each revolution as a lower bound.

The acquisition time varied from 15s to 30s, in order to guarantee the statistical significance of the data: lower $RPMs$ results in higher acquisition times in order to have a sufficient number of revolutions.

The tests were conducted in three separate days, with the following schedule:

- Day 1: tests were conducted at $4.5m/s$ and $6m/s$;

- Day 2: after an initial post-processing of the acquired data, tests were repeated at the same wind speed in order to obtain more data points;
- Day3: tests were conducted at $8m/s$ and $10m/s$.

Given the limitations discussed above, this last battery of tests was less significant: increasing the wind speed, at the same angular velocity the TSR decreases, therefore only data at really low λs was obtained. The situations was further aggravated by the fact that we can expect the aerodynamic forces to scale with the square of the upstream velocity, thus increasing the resulting stress on the structure. This was observed empirically: stopping the blade in a stalled position gave rise to strong oscillations; while this was not measured, oscillations grew appreciably with wind speed.

4.3.1. Post-Processing

Post-processing of the data was executed on Matlab. This was mainly dictated by the acquisition procedure: the Matlab App stored the data in a `.mat` file as a `timetable`, an example of which is reported below.

data.V6rpm15_8

	Time	1 cDAQ1Mod4_ai1	2 cDAQ1Mod4_ai2	3 cDAQ1Mod4_ai3	4	5	6	7	8	9	10
1	0 sec	0.0688	0.0914	2.6465e-04							
2	0.001 sec	0.0685	0.0927	-5.1440e-05							
3	0.002 sec	0.0682	0.0920	-5.1440e-05							
4	0.003 sec	0.0682	0.0917	2.6465e-04							
5	0.004 sec	0.0685	0.0917	-5.1440e-05							
6	0.005 sec	0.0682	0.0927	2.6465e-04							
7	0.006 sec	0.0679	0.0914	-6.8362e-04							
8	0.007 sec	0.0672	0.0914	-5.1440e-05							
9	0.008 sec	0.0663	0.0914	2.6465e-04							
10	0.009 sec	0.0669	0.0920	-5.1440e-05							
11	0.01 sec	0.0669	0.0911	2.6465e-04							
12	0.011 sec	0.0657	0.0911	2.6465e-04							
13	0.012 sec	0.0657	0.0911	2.6465e-04							
14	0.013 sec	0.0657	0.0911	-5.1440e-05							
15	0.014 sec	0.0650	0.0904	-5.1440e-05							
16	0.015 sec	0.0653	0.0907	2.6465e-04							
17	0.016 sec	0.0635	0.0901	5.8074e-04							
18	0.017 sec	0.0641	0.0904	-3.6753e-04							
19	0.018 sec	0.0638	0.0904	-3.6753e-04							
20	0.019 sec	0.0628	0.0901	2.6465e-04							
21	0.02 sec	0.0628	0.0891	-3.6753e-04							
22	0.021 sec	0.0631	0.0895	-5.1440e-05							
23	0.022 sec	0.0631	0.0891	2.6465e-04							
24	0.023 sec	0.0628	0.0888	-3.6753e-04							
25	0.024 sec	0.0625	0.0888	2.6465e-04							
26	0.025 sec	0.0628	0.0885	-3.6753e-04							
27	0.026 sec	0.0625	0.0885	2.6465e-04							
28	0.027 sec	0.0625	0.0885	2.6465e-04							
29	0.028 sec	0.0625	0.0872	-3.6753e-04							
30	0.029 sec	0.0622	0.0875	-5.1440e-05							
31	0.03 sec	0.0622	0.0875	-5.1440e-05							

Figure 4.5.: Example of `timetable` data

The first column refers evidently to the time, the other three represent the voltage signal already pre-processed by the DAQ: the two differential signals in input are already scaled and the final calibrated datum is acquired by the PC. The first channel collects the generator voltage, with a scaling factor of $1V_{signal} = 20V$, the second the current, acquired as voltage and then transformed again with the conversion factor $1V_{signal} = 4A$. The third channel contains internal phase data and can be left as is, in so far as we need only its frequency and not its amplitude.

The `timetable` is then converted in a series of arrays and the main frequency of the data is computed via a fast-Fourier-transform on the phase signal. The validity of this result was verified a third time by executing the same operation on both voltage data: being tied to the aerodynamic forces during a revolution we expect to find the same main frequency.

In Fig. 4.6 is reported an example of this signal in frequency space. Peaks are well defined, and repeat regularly with their harmonics. Furthermore, the number of revolutions thus computed matches almost perfectly with the one annotated at acquisition time obtained with the photodetector with an offset of a couple of RPMs that tends to decrease as the revolution speed increases.

Once the frequency is obtained we can compute the RPMs of the test and from this the number of samples expected for each revolution. This data is then stored in `samplesPerRevolutions` $\times$ `nRevolutions` Matrices in order to facilitate the next operations. Via a piecewise multiplication between voltage and current the instantaneous power was computed at each point in the data-series, this allows to then compute the mean power for each revolution.

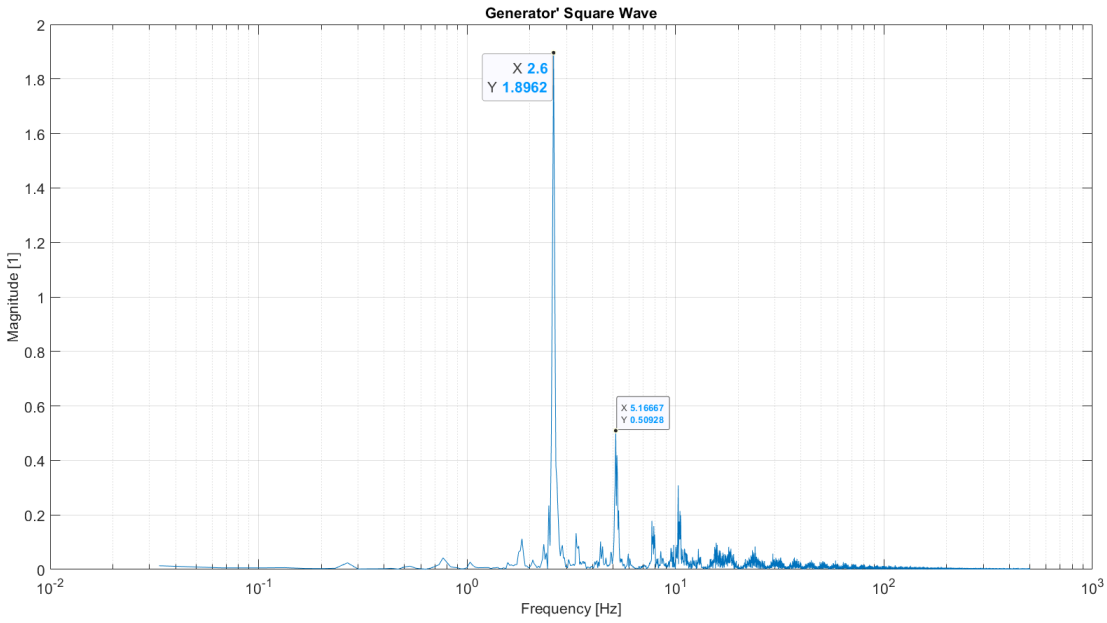

Figure 4.6.: Signal analysis result in the case of $V_w = 6m/s$ and $RPM = 17$

The final result will then be mean power over all complete revolutions, the first revolution is discarded to further guarantee equilibrium conditions, while data not fitting in the prescribed window is also discarded to simplify computations.

The mean power can then be readily transformed in mean power coefficient, this was done by using *ISA* air at a temperature of 28°, equivalent to the air temperature during testing sessions, heating of air in the test section was discarded as we expect the effect to be less significant.

Finally, standard deviation was computed as

$$\sigma = \sqrt{\frac{\sum_{i=0}^{N} (P_i - P_m)^2}{N}},$$

and from this follows the standard error

$$SE = \frac{\sigma}{\sqrt{N}},$$

where N is the expected number of revolutions but in practice coincides with the number of windows used in the averaging process.

An analogous process was followed to obtain the mean RPM and its standard error.

Given the magnitude of the standard errors obtained, all graphs in next section present error bars relative to 50 standard errors. Precise and complete data is reported in Appendix **??**.

4.3.2. Results

A coherent behaviour was observed across all three tests, even if it was possible to acquire a complete power curve only for the lower wind speed of 4.5 m/s.

As can be seen from the graph below, we can expect a greater efficiency at higher wind speeds in the same rotational regime. Given that the effective power outputs scales with the cube of the upstream velocity, even greater effective power is produced. Indeed it can be observed how, for $\lambda \approx 0.5$, for $V_\infty = 6$ we have $C_p = 0.03$, while for $V_\infty = 10$ we have $C_p = 0.05$. This can seem like a small difference but in practice results in an output power delta of $30W$, rising from $5W$ to $35W$.

For clarity's sake the data is reported as a least-square fit to a third-degree polynomial. [2]

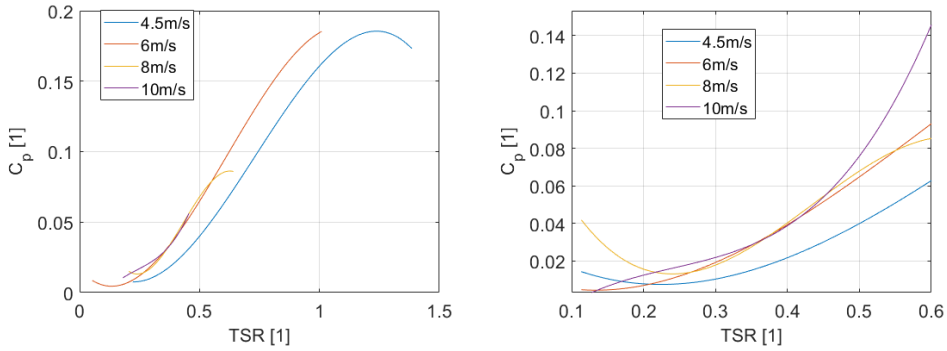

(a) $C_p(TSR)$ (b) Detail for $\lambda < 0.6$

Figure 4.7.: Aerodynamic Characteristics at different Reynolds' numbers - Fitted data

The difference in efficiency between $V_\infty = 6m/s$ and $V_\infty = 4.5m/s$ is clearly evident, as is the similarity in curve shape. As said before, data for the last two test cases is lacking and therefore satisfying conclusions can not be drawn from them. However, as can be seen in the detail above, the performance for $V_\infty = 6, 8, 10m/s$ seems to coincide in the examined range: while slight differences in efficiency can be observed, the power curves seem to be largely the same. This can be justified as follow:

- as said before, this trend is related to the efficiency and not net power output, it is therefore reasonable to obtain similar values;

[2] A complete representation of the fitting data and the resulting polynomials are reported in Appendix C.3

- the scarcity of data doesn't permit to judge the generality of this trend;
- the TSR range of the data, namely $\lambda < 0.6$, is a critical one: in this range instability effects are predominant, additionally the high blockage ratio could have some effects on the effective velocity seen by the rotor-disk.

As observed above, only for $V_\infty = 4.5m/s$ a complete curve was obtained, while for the higher velocities the structural limit didn't allow the investigation at higher TSRs, and the data remains therefore incomplete.

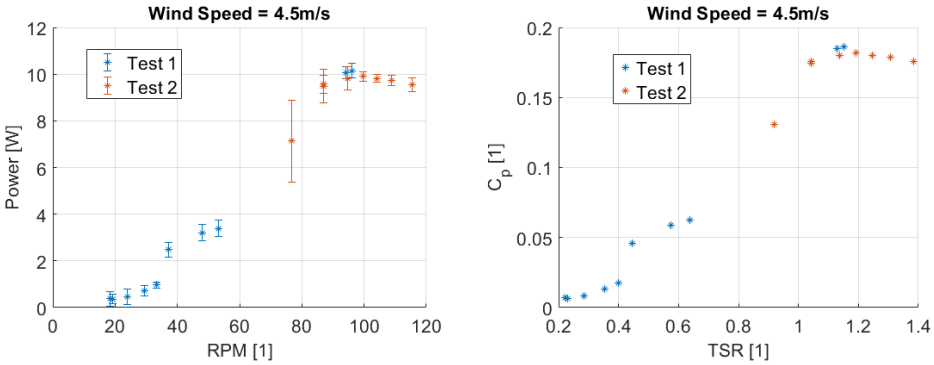

(a) $P(C_p)$ (b) $C_p(TSR)$

Figure 4.8.: Test results for $V_\infty = 4.5m/s$

Error bars are reported only in the case of output power mainly because this is the data directly measured, while in order to obtain C_p further processing is needed. The error bars reported are relative to $50 * SE$ for readability.

A repeatability test was conducted for $RPM = 88$ with satisfactory results as evident in the graph. Additionally the two tests, conducted on separate days, fit remarkably well into each other, as evident in the zone around 90 RPM.

Data for $V_\infty = 6m/s$ shows a similar trend but a significant amount of noise is present in the data acquired in the third test; this doesn't seem to be due to an inconsistency of the rotational speed, as we can see in Fig. C.2, while we could maybe attribute it to pulsations: the low velocities and the continual access to the test section between tests are not ideal for the correct operation of the driving fan.

A general doubling of the net power output is observed between this case and the former one.

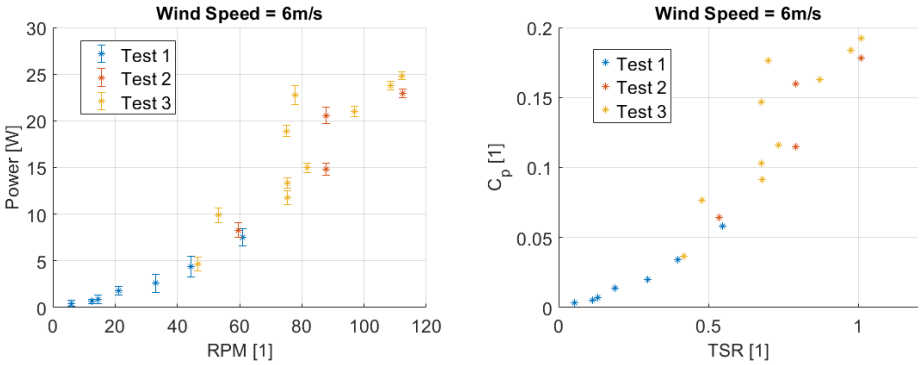

(a) $P(C_p)$ (b) $C_p(TSR)$

Figure 4.9.: Test results for $V_\infty = 6m/s$

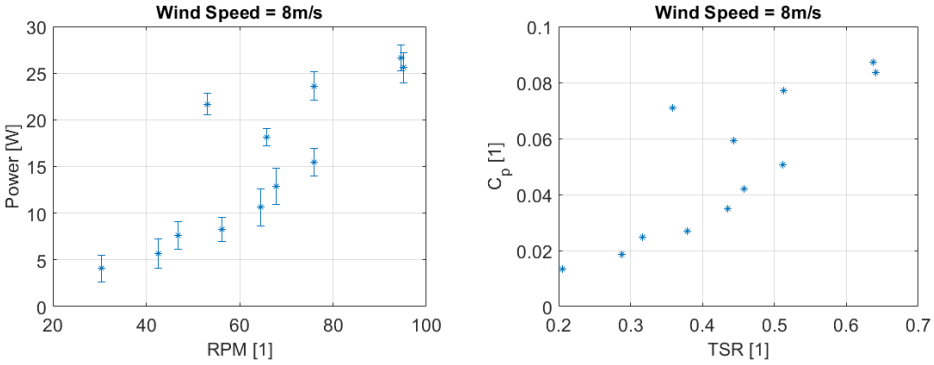

(a) $P(C_p)$ (b) $C_p(TSR)$

Figure 4.10.: Test results for $V_\infty = 8m/s$

Some noisiness is present also for $V_\infty = 8m/s$ namely for 50 RPM, but the general curve trend remains coherent with the ones observed above.

For $V_\infty = 10m/s$, higher uncertainty is present for $RPM = 50, 85$, this is expected given the low number of revolutions considering also flow-field instability in this TSR-range.

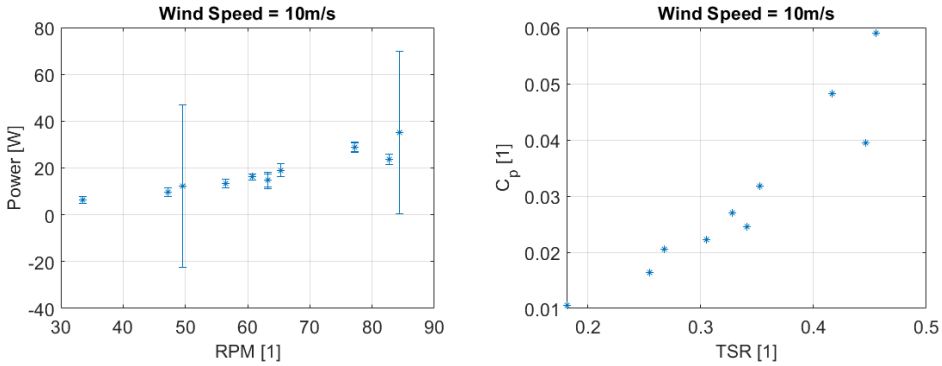

(a) $P(C_p)$ (b) $C_p(TSR)$

Figure 4.11.: Test results for $V_\infty = 10m/s$

The noisiness of the results encouraged a different post-processing methodology: instead of processing the data in windows determined by the rotational speed, all acquired data, for each condition, was mediated.

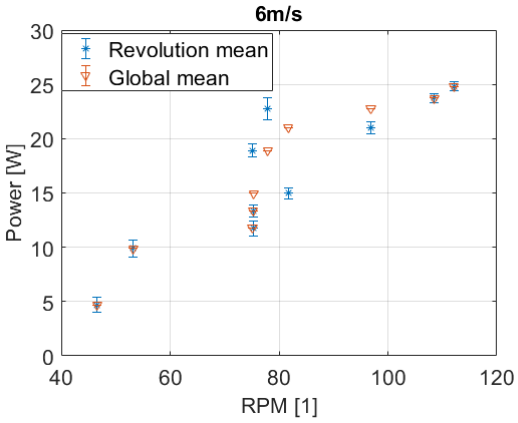

Figure 4.12.: Comparison between the two post-processing methodologies

We can see that the results do not vary substantially between the two cases.

For this reason, the RPM value annotated at acquisition time was used. As we can see in Fig. 4.13 this results in much cleaner data, therefore it is probable that for some tested conditions the accuracy of the methodology used to acquire angular velocity failed. This is not however a general trend, but is rather confined to those points in the graphs above that seem to be affected by errors, either in the acquisition phase or the processing one. This set of data will therefore be used for all future comparison with simulations. Since the annotated RPM were obtained with a more accurate instrument, namely a photodetector, this choice is further justified. Successive investigations and a reproduction of the specific conditions that resulted in problematic data may shed some light on the nature of the problem, random or systematic, in which last case a redesign of the whole procedure would be necessary.

This third methodology eliminates the problematic points leaving the general trends unchanged: we can see the same marked difference between $4.5m/s$ and $6m/s$, while the curves at really low TSRs tend to overlap.

We can conclude that the turbine shows excellent performance at lower TSRs; the efficiency in regimes of low-TSR, low-wind-speed, was found to be remarkably high given the data available in literature, where designs favour operational regimes at higher velocities. The high efficiency at low wind speed is particularly adept to fulfil the rotor mission of power generation in all conditions, while the low rotational regimes allow for a simpler, and therefore cheaper, structure. It must be noted, however, how the maximum instantaneous power output reached was of only $35W$, this underlines the main drawback of this design philosophy, namely the low power output: while the values of C_p are average, the low wind speeds and rotational regimes present an hard limit on the extractable energy. In order to obtain greater performance a new design is needed, capable of producing energy at higher TSRs: as can be seen in Fig. 4.13 this turbine reaches its maximum power output around $\lambda = 1$, which is considered low-TSR regime: the flow is still governed by high-levels of turbulence, dynamic stall and instability. A redesign capable of operating efficiently at high-TSRs, > 2, both aerodynamically and mechanically would in theory

grant greater instantaneous power. In any case, extrapolating the results obtained for $V_\infty = 4.5m/s$ to the curve at $V_\infty = 10m/s$ we can reasonably theorize a maximum C_p of 0.2, resulting in a peak power output of more than $100W$. While this would be an adequate power output given the turbine's size, such wind speed are not to be expected in all locations, thus reducing the applicability of the prototype, although it remains suited to operate in insular or mountainous environments.

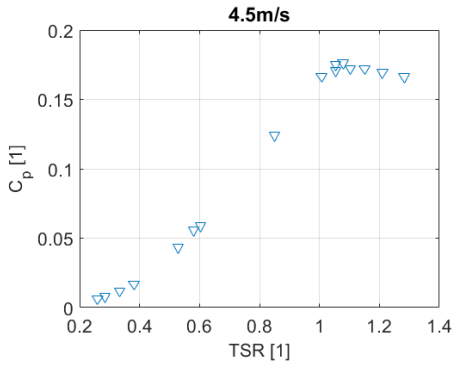

(a) $C_p(TSR) - 4.5m/s$

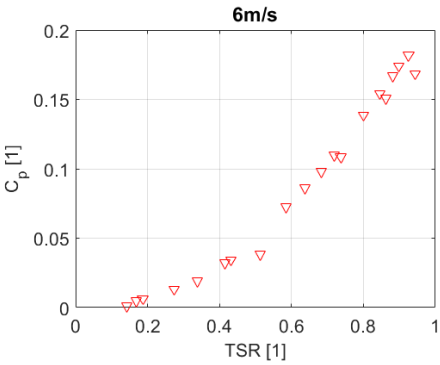

(b) $C_p(TSR) - 6m/s$

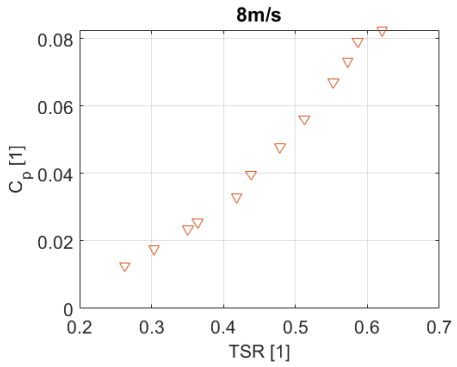

(c) $C_p(TSR) - 8m/s$

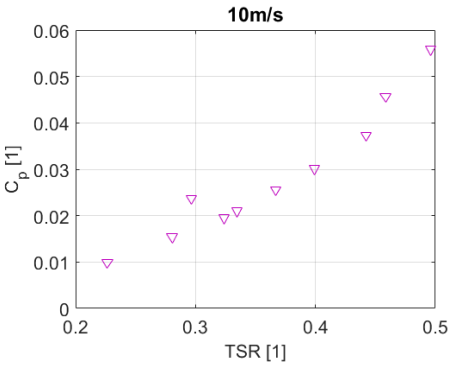

(d) $C_p(TSR) - 10m/s$

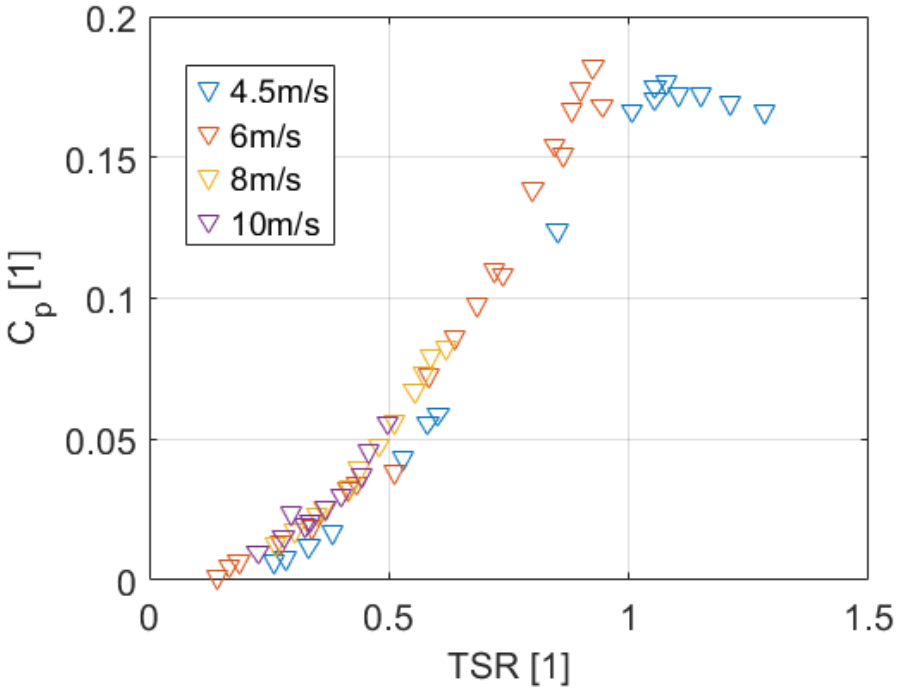

(e) $C_p(TSR)$

Figure 4.13.: Test results using annotated RPM

5. Low-Order Analyses

In the first phase of this study the software QBlade was employed to obtain the power curves of the rotor at different wind speeds. This was done in order to obtain a first estimate of the turbine's performance in different operating conditions.

Furthermore, prior studies showed how, even though the specific pairs (C_p, λ) are not representative of the actual efficiency, the shape of the curve is representative of the real one, with a general overestimation of the C_p values.

5.1. Simulation set-up

The first step of the analysis is the design of all necessary airfoils, this is usually done by importing its coordinates. Once this is done, the aerodynamic properties of the airfoil must be evaluated. QBlade offers the option to do this in an integrated module, which essentially calls an instance of XFoil. Since an higher degree of accuracy was desired, CFD simulations were carried out with Siemens' STAR CCM+ for the NACA 0024 profile at different Reynolds number in order to take advantage of the multi-polar functionality of QBlade. C_l, C_d, and C_m values were computed in the software and imported in QBlade, where they are then extrapolated with the Viterna model[32] to a 360° polar.

The simulations were conducted with a profile of $0.1m$ chord (c in the following) in a rectangular domain of $40c \times 50c (W \times L)$. The range of Reynolds numbers, 2e5 to 4e5, resulted in low enough velocities to justify the use of the 2nd-order **Segregated Flow** model with constant density, with a steady state solver. A grid independence study was conducted, resulting in a polygonal mesh with ≈ 28000 cells[1], using the **Wake Refinement** model an isotropic mesh region was realized down-stream of the airfoil extending for $20c$ with a cell diameter of $0.08c$ and an angular aperture of 14°. In the near wall region a prism layer mesher was used with 25 layers taking care to obtain $y^+ < 1$ in the first cell.

The simulations were conducted in batch using the **Simulation Operations** tools. Once the Reynolds number is selected, the software autonomously launches the simulation, once the lift and drag coefficients doesn't vary more than 0.1% across 500 iterations, the simulations is saved, and all relevant data exported. Finally the angle of attack is increased and the process repeated.

With a 6 core CPU and 16 GB, 3600 MHz memory, simulations time varied from the low end of $2 \cdot 10^2 s$ to $7 \cdot 10^2 s$, increasing with the angle of attack and Reynolds number.

Finally, the drag coefficient at $\theta = \pi/2$ was computed in a similar manner to be employed in polar extrapolation.

[1] The number of cells varies slightly with the angle of attack.

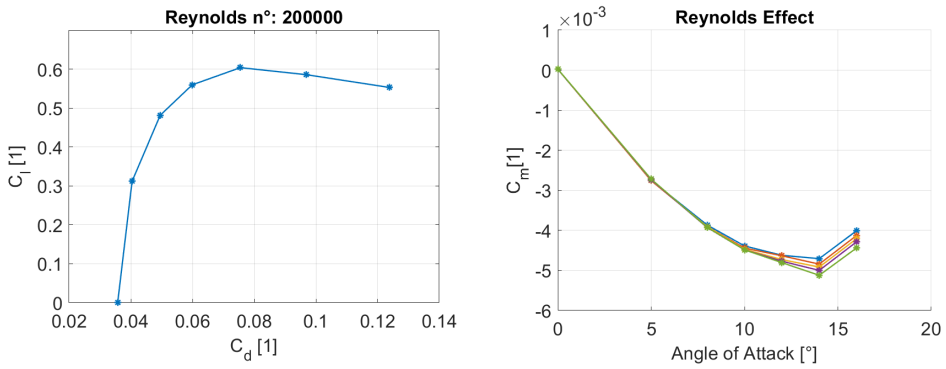

(a) $C_d - C_l$ Polar (b) C_m

Figure 5.1.: Aerodynamic Characteristics at different Reynolds' numbers

Complete results are reported in Appendix B.1.

Once this is done, the blade can be designed. The software allows to do this by defining different sections along its length. At this point the number of blades, the radius of the turbine, and the struts must also be defined.

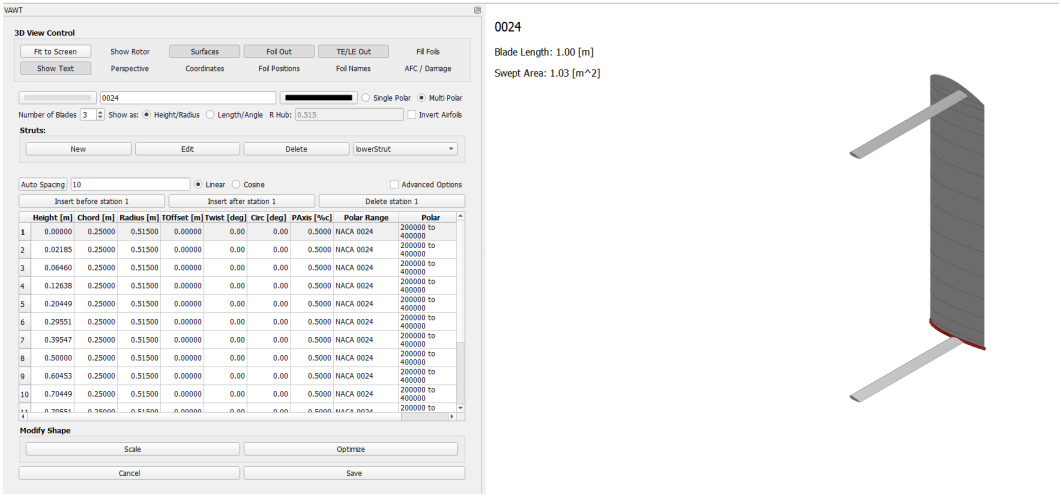

Figure 5.2.: Blade Design Interface

The simulation proper is defined in the *Turbine Definition* module, where additional geometric parameters are defined and several numerical options can be selected.

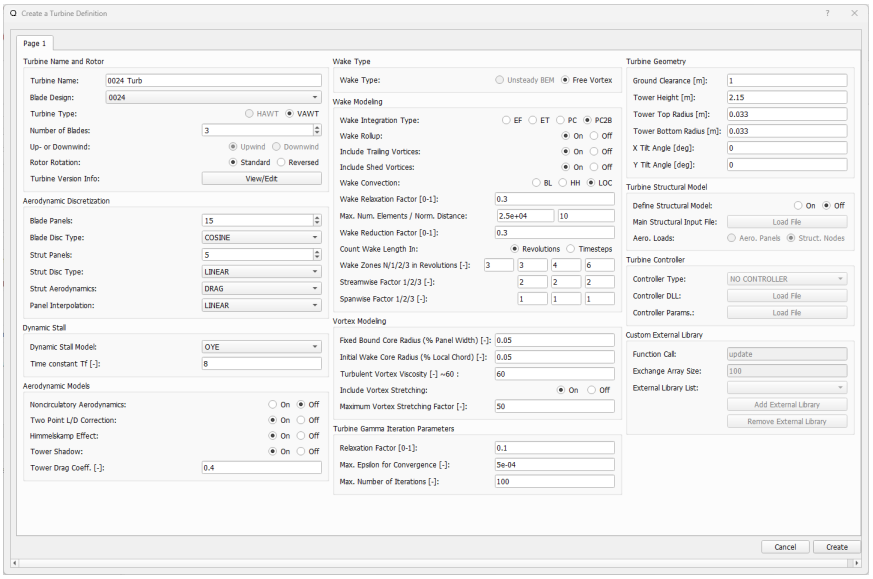

Figure 5.3.: Turbine Definition Mask

For the modelling of dynamic stall, the solution proposed by Oye in [24] was employed. While Bangga et al. [3] showed how their IAG model can have significantly improved accuracy, this method also requires the fine tuning of several parameters in order to be employed.

3D correction are accounted by the Himmelskamp effect which increases lift at inner blade stations as explained in [30].

The Tower Shadow options allows the blending of potential flow around the shaft with the Free Vortex Wake downwind and is based on the work of Moriarty and Hansen[23].

For wake modelling the second-order predictor corrector method was chosen and both trailing vortices and shed ones were included in the simulation. This resulted in greater accuracy with negligible increases in simulation time. As Manter showed in [18], in a steady state simulation shed vortices can be optionally disabled, being proportional to a temporal term; in the low-TSR regime in which this turbine operates it was found how not only this reduces the accuracy of the simulation, but also increases the number of time-step needed for convergence; the reduction in computation time per time-step was found to be insufficient compared to the increase in simulation time and shed vortices were therefore included. A wake reduction factor of 0.30 was chosen: this removes the 30% of lower circulation wake elements. Menter suggests that up to 50% of these elements could be removed. This was partly independently verified: simulations were conducted with a wake reduction factor of both 0.30 and 0.15 and no difference was found in the resulting C_p.

In the mask below, each simulation is defined. First, the wind speed was chosen, and then the TSR was made to vary from 0.5 to 3.0, initially with 0.1 steps and then more roughly after $\lambda = 2$ was reached.

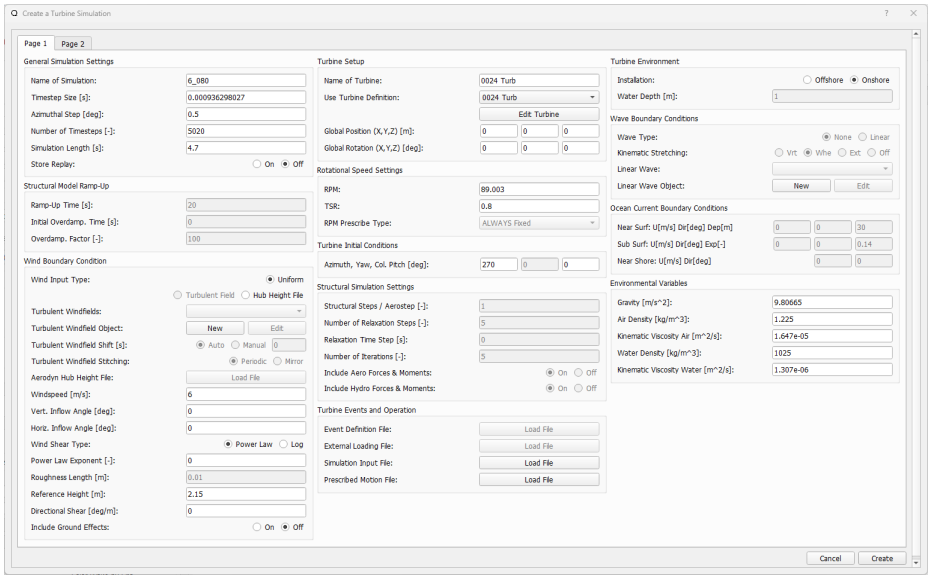

Figure 5.4.: Turbine Simulation Definition Mask

The software allows the definition of the time-step both as a temporal value than as an angular rotation, the same is true for simulation duration, which can be defined both as a total time as a maximum number of time-steps.

For the time-discretization a rotational time-step of 0.5° was chosen, which resulted in a time step of around $5 \cdot 10^4 s$, this is well below the value suggested by Manter of $0.001s$. The total number of time-steps necessary to reach convergence was set with the most stringent case and then utilised for every simulation. This criteria resulted in 5040 iterations, or 7 revolutions.

5.2. Results

Two different analyses were conducted:

- the turbine's operational range for various wind speeds was evaluated;
- the second analysis was a more aimed one: following the experimental campaign, each tested condition was simulated.

So while the former analysis allowed an overall view of the turbine's performance, the latter was used to evaluate the applicability of these results.

5.2.1. Operational range

The analyses were conducted starting from $\lambda = 0.5$ to $\lambda = 3.0$ for $V_w = 4, 6, 8 m/s$. This was the first analysis conducted, and therefore it was necessary to have an estimate of the salient points to investigate, both empirically and with more accurate numerical methods. After the wind tunnel investigation and the CFD simulations, an additional simulation was set-up at $V_w = 9 m/s$.

A qualitative discussion of the results follows. Exact results are presented in Appendix B.2 in tabular form.

As can be seen from the graph below (Fig 5.5), all curves present a peak at $\lambda = 2$, with a maximum C_p value of 0.447 for $V_w = 9m/s$. Already it can be observed how this is an extremely high value: given the hard limit imposed by Betz's theory, $C_{p,max} \approx 0.59$, it would seem that the turbine reaches almost the maximum theoretical efficiency. While this could be possible, it seems unreasonable with an unoptimized design.

All curves show a near identical behaviour at low-TSRs, indeed it can be seen from Fig. 5.5.(a) how the C_p assumes identical values for $V_w = 4m/s$ and $V_w = 6m/s$. This could be due the low order accuracy of the simulation. More precisely, given the low wind speeds and the low rotational velocities, a regime of low Reynolds number is expected for the flow around the blades. This could constitute a problem for the solver: if both conditions result in a similar lift coefficient, indeed it was observed how, especially for low angles of attack, the Reynolds Effect is almost negligible in the examined range (Fig. 5.1, also see Appendix B.1), expressing at most a variation of $\approx 15\%$ with $\Delta Re = 2e5$, both conditions could result in a similar circulation, and therefore the solver *should* converge to the same induced velocity field. Given that both the angular velocity, and therefore the tip-speed, and the free-stream one assume small values in these cases it seems reasonable that the induced velocity could dominate the vectorial sum, resulting in the same net C_p. This is further justified by the nature of the flow-field in this regime. It is however important to observe how even with the same power coefficient the output power is different between those conditions.

Behaviour then begins to diverge around $\lambda = 1.2$, as evident in Fig.5.5.(b) and is completely heterogeneous past $\lambda = 1.5$ even tough all curves follow the same trend of a soft peak followed by a sharp decline until the we reach the final data point at $\lambda = 3$; in this condition the power output is similar to the one in the $\lambda = 0.5 - 0.8$ region.

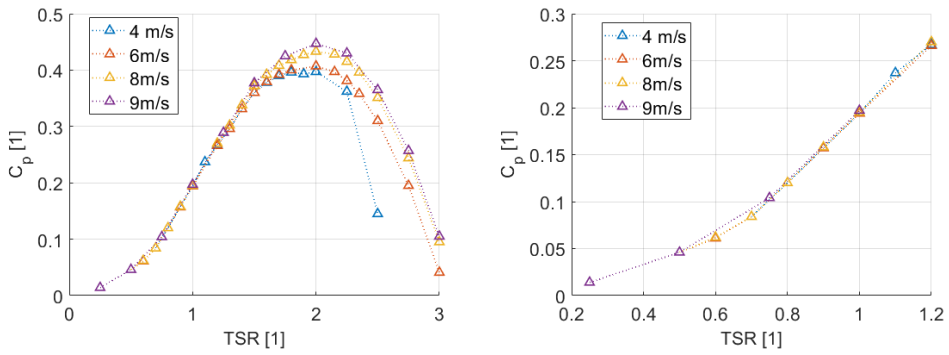

(a) $C_p(TSR)$ (b) $C_p(TSR)$ -Detail

Figure 5.5.: QBlade results over the operational range

5.2.2. Comparison with wind tunnel data

After the empirical tests were completed a second study was conducted in order to obtain a simulated data point for every experimental one, this allowed to do a 1-to-1 comparison and therefore a more funded judgement of the investigation methodology.

Since the tests were RPM-controlled, the same was done for this batch of simulations, replicating each test condition in both free-stream velocity and number of revolutions per minute. A couple of important differences should here be noted:

- it was not possible to replicate the entire support structure of the turbine, instead the software allows only for blades, struts, and central shaft;
- while the tests were conducted in high-blockage environment, indeed the ratio between the diameters of test section and turbine is nearly 3:1, QBlade simulates a free field; the effects of the ground are accounted and it is possible to configure the free-stream velocity in its cross-plane, but as of now stream-wise pressure gradients are not included.

For the level of accuracy desired from this kind of simulation, the first difference can be ignored while the second should result in a tangible difference. As seen in Section 4.2, even accounting for the test section wall divergence, a significant pressure gradient should be expected to develop. At this point it is not clear *how* this gradient influences the turbine's performances. Fig. 6.1 represents the main velocity field of a 2D CFD simulation in the same configuration as that of the tests. As can be seen a strong pressure gradient develops and the flow outside the rotor wake is visibly accelerated aft of the turbine.

Keeping this in mind, the final results show remarkable agreement with the empirical data. Even if in some cases the relative errors seem to be rather large, it must be noted that these results are of the order of 10^{-2}, even small variations in absolute value result in significant errors. At the same time, the magnitude of the results is equivalent to estimated precision of the simulation. This is better observed in Fig. 5.6.(g), where, having obtained only small values of C_p the scale permits to clearly see how the two curves follow the same trend, with QBlade always overestimating the results.

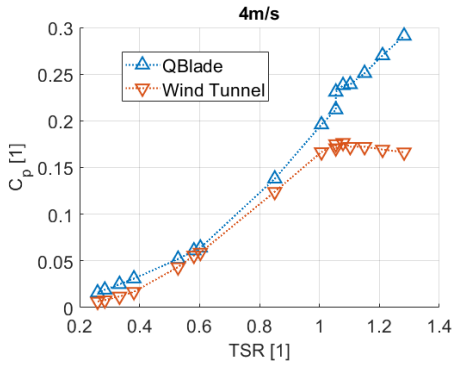

(a) $4m/s - C_p(TSR)$

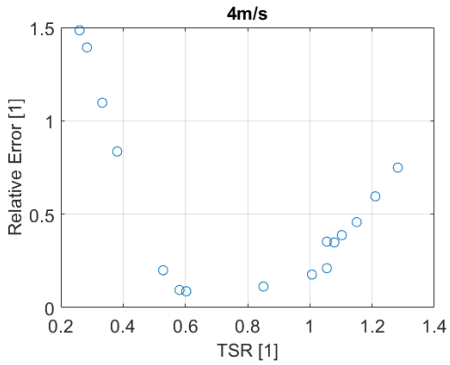

(b) $4m/s$ - Relative Error

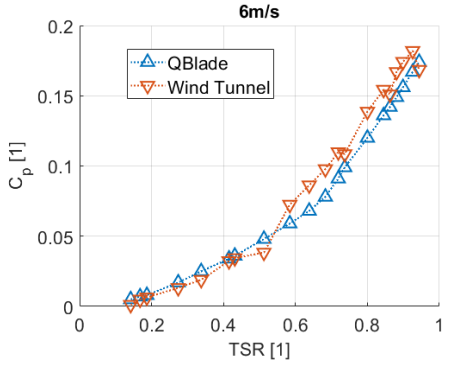

(c) $6m/s - C_p(TSR)$

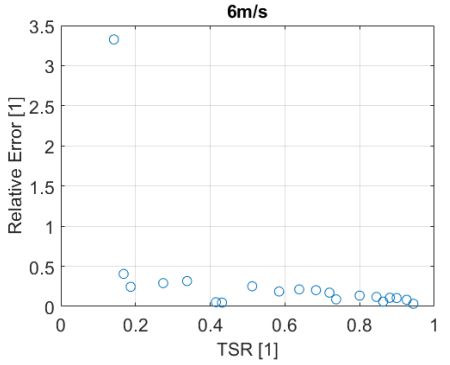

(d) $6m/s$ - Relative Error

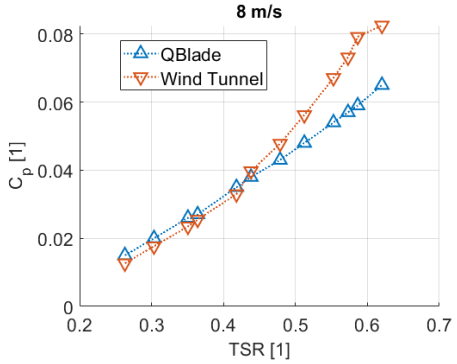

(e) $8m/s - C_p(TSR)$

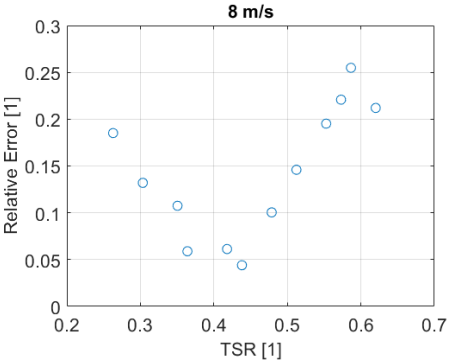

(f) $8m/s$ - Relative Error

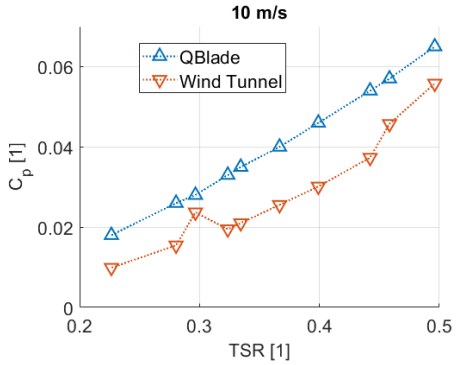

(g) $10m/s - C_p(TSR)$

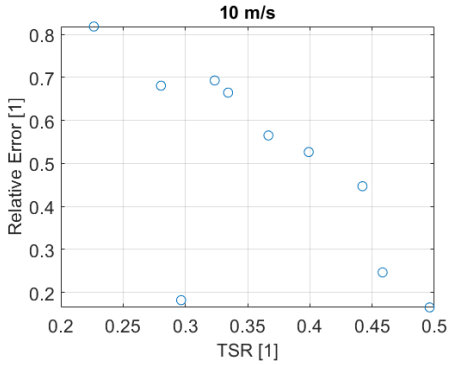

(h) $10m/s$ - Relative Error

Figure 5.6.: Comparison between QBlade data and experimental ones

From the graphs in Fig. 5.6, a general behaviour is observed: the relative error reaches a minimum approaching $\lambda = 0.5$ to then increase again. Looking at the larger picture,

justification for this can be found in the cases in Fig. 5.6.(c) and 5.6.(e): in both occurrences there's a clear inflection point near $\lambda = 0.5$ where the wind tunnel data starts to diverge and increase faster then the numerical one. As seen in the last section, this is not a general trend. Indeed, comparing the two results, it is evident how on the whole QBlade overestimates the turbine's performance and fails in denoting the maximum point as clearly seen in Fig. 5.7.(a).

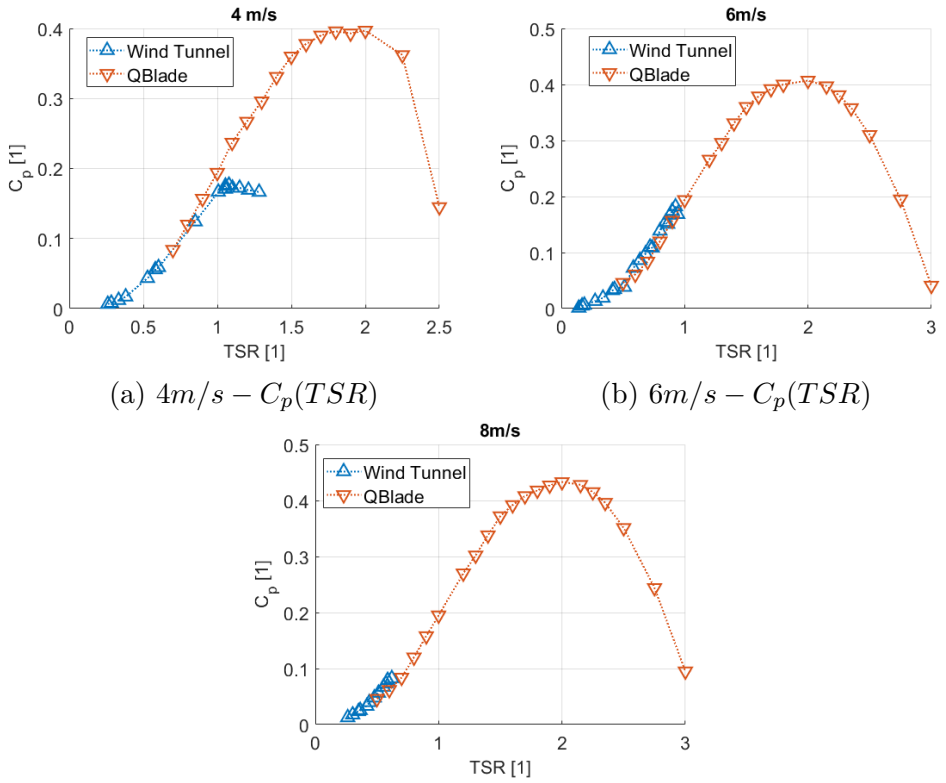

(a) $4m/s - C_p(TSR)$ (b) $6m/s - C_p(TSR)$

(c) $8m/s - C_p(TSR)$

Figure 5.7.: Comparison between QBlade data and experimental ones

Additional empirical data, specifically at higher free-stream velocities, is required to establish if this is a general trend or a peculiarity of the low speed of the first case.

With this results, the use of QBlade for an initial estimation of a new design performances is feasible as long as the operative range is reduced to very low TSRs ($\lambda < 1.25$). However, the strong match observed in this region is clearly ground to justify further investigations and refinements of the procedure: using different stall models, and calibrating their parameters, together with other simulation ones, namely those relative to the Vortex Modelling, with additional empirical data, may results in stronger results for a wider range of λs. To this should be added CFD data in a wider range of AoAs for a better outcome.

6. CFD analyses

The literature review was used as an essential stepping stone in the development of the Computational Fluid-Dynamics model.

Initially the simulation were set-up for a reproduction of the wind-tunnel data, however this was found to be unpractical for mainly two-reasons:

- as said before the high blockage ratio caused a significant stream-wise acceleration across the turbine, while this is certainly expected behaviour, the absence of wind-tunnel data on the matter makes this a possible additional criticality, in that it isn't impossible to establish if the *magnitude* of the acceleration is a coherent one;
- the second reason was more practical: given the dimensions of the turbine, the rotating region needed to simulate the movement of the turbine would be much too close to the wind tunnel walls, therefore opening the door to artefacts in the flow-field.

As can be seen in the figure below, the test-section dimensions are not significantly larger than those of the rotor; this causes a strong interaction between the flow-field that would naturally develop around the rotor and the wind-tunnel walls. Even accounting for the slight divergence of the test-section in the stream-wise direction, there is a significant pressure-gradient due to the developing boundary layer on the walls; the rotor presence further increases this effect.

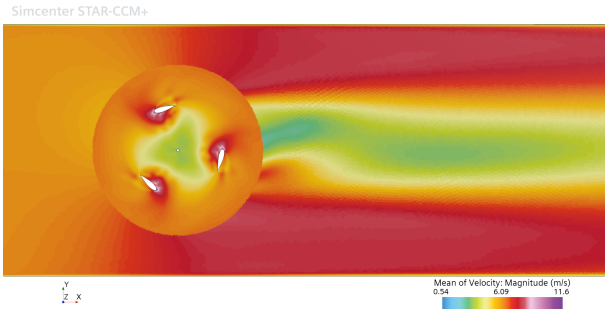

Figure 6.1.: Mean velocity field in the test section as simulated on Star CCM+

This is clearly illustrated in Fig. 6.1, where the mean velocity field is represented for $\lambda = 1$ and $V_w = 6m/s$. Aft of the turbine and outside its wake the flow is significantly accelerated compared with the upstream condition. Furthermore, in figure 6.2 the pressure gradient along one of the test-section walls is reported. Here the influence of the turbine, with its shaft centred on the reference frame origin, is evident.

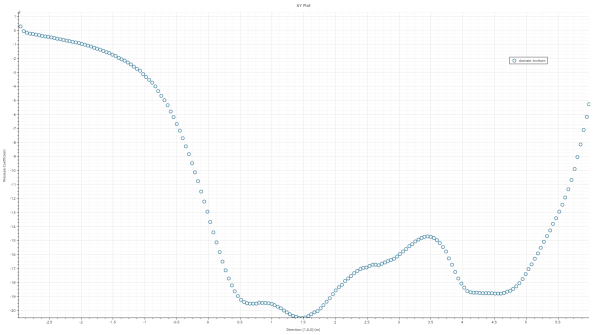

Figure 6.2.: Pressure gradient on the bottom wall

It's important to note however how the simulated 2D condition is significantly more affected by this phenomenon than the real case of a fully developed 3D flow.

All simulations were conducted with STAR CCM+ on a 12-core CPU with 128GB, 3200MHz memory, with an average computation time per time-step of $1.95s$.

6.1. Simulation Set-Up

In this section the model implementation is discussed.

The **Segregated model** was preferred to the coupled one. The magnitude of velocities in the flow-field allows for the use of the incompressibility hypothesis, however as discussed by Balduzzi et al. [2] the coupled option results in a more accurate simulation, additionally, given the low-TSR regime of the simulations, this results in more *stable* (i.e. dampened oscillations between revolutions) solution. In this case, as a 1-st order discretization was chosen, this damping effect was found to be unnecessary and therefore the lower computational cost was preferred.

For the same reason a rotational time-step of $\theta = 0.5°$ was selected and found to be sufficient. The number of inner iterations is kept consistent throughout the simulation to 40: this value was chosen by taking an already converged simulation and gradually lowering the number of inner iterations and observing residuals' behaviour: since the residuals maintained an asymptotic behaviour to the same magnitude, 40 was chosen as the optimal number.

The choice of turbulence model was straight-forward: as shown in Section 2, the $\gamma - Re_\theta$ **SST** model is the most accurate and was therefore employed with a second order discretization. The model was used with the default parameters.

Rotation of the rotor was handled with an **Direct Rotating Motion Value**: a rotating region of diameter $1.36D$ is created separate from the domain and then subtracted to the same, this allows to create two regions, connected seamlessly, withh an **Internal Interface** allowing the fluid to move across the two regions. The correct value of ω, computed as

$$\omega = \frac{\lambda V}{r},$$

is then assigned as a boundary condition.

For meshing operations, STAR CCM+ **polygonal mesher** was employed with a prism layer mesher in the near wall regions.

Several meshing strategy were investigated; ultimately, given the dimensions of the domain, a isotropic refinement in the wake region, using the **Wake Refinement** model,

was employed while for the fore region with a volumetric control a quadrangular area was selected for the same refinement. Extension and location of this area were based on previous test runs of the simulations by examining the expansion bubble.

This meshing strategy resulted in $3.6e4$ cells in the main domain and $4.0e4$ in the significantly more refined rotating part. In the figures below a general view and details of the final mesh are presented.

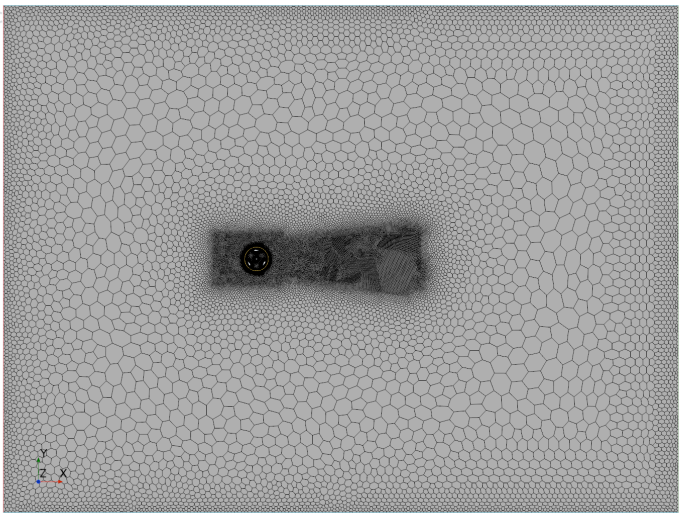

(a) Global Mesh

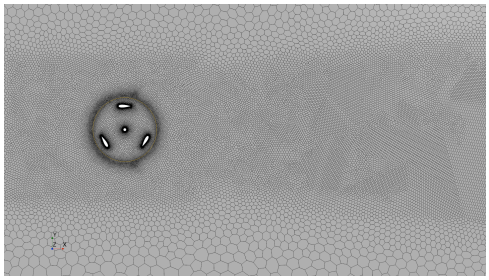

(b) Refinement in the aft and fore zones

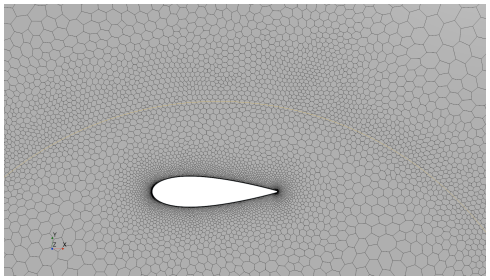

(c) Interface zone

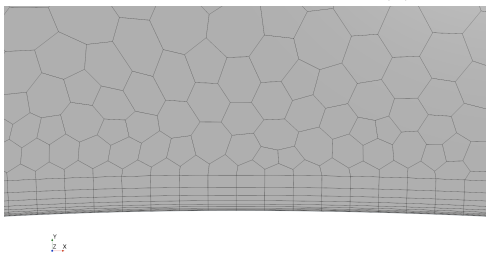

(d) Prism layer

Figure 6.3.: Mesh

In Fig. 6.3.(c) we can observe how at the interface between the two parts the cells are cut in half: this is due to the meshing procedure that guaranteed the same cell dimension at the interface. This is only true for this particular mesh position, during the revolution inner cells shift while the outer ones stays in place. For this reason cells in this region *must* have the same dimension in order to limit differences in volumes in the balances across the

interface. This also guided the choice of time-step: for convergence it's preferable that a cell does not move more than its width over a time-step. The prism layer in Fig. 6.3.(d) was found to be adequate for all tested conditions: in the more stringent one, namely $V_w = 9m/s$, $\lambda = 1.75$, an average $y+$ of 0.3272 was found across all relevant surfaces. This value is averaged not only on all the surfaces but across a revolution: as can be seen in the following figure the dimensionless wall distance varies with the apparent velocity on the no-slip surface.

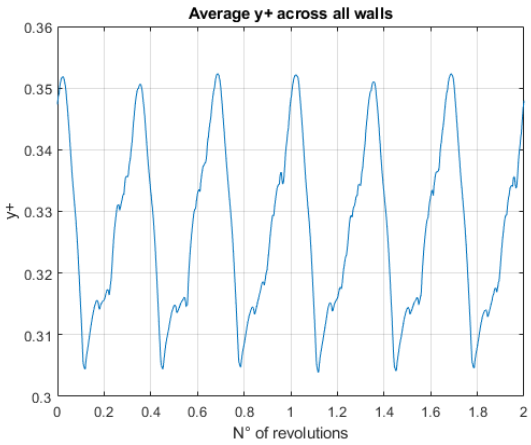

Figure 6.4.: Average value of y+ across two revolutions

The **Simulation Operation** tool was once again used: using the same mesh for all simulations allowed to automate the launch, export of relevant data, and saving of the simulations. An adequate stopping criterion was chosen to guarantee convergence.

Turbulence Model	k-ω SST
Pressure-Velocity Coupling	Segregated
2D or 3D Analysis	2D
Inlet Length	15D
Outlet Length	25D
Blockage Ratio	3.4%
Rotational Domain Diameter	1.36D
Rotational Step(2D)	0.5°
Cell Count	$8e4$

6.2. Results

Simulations were conducted for the following cases:

- wind speed:
  - $4m/s$;
  - $6m/s$;
  - $9m/s$;
- TSR: from 0.25 to 1.75, with 0.25 increments;

for a total of 21 simulations.
Fig. 6.5 shows the results across all simulated conditions.

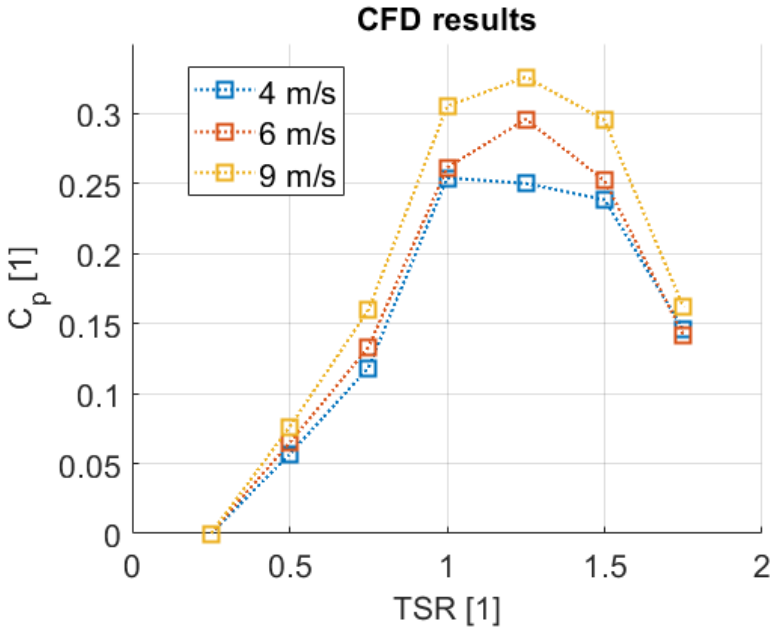

Figure 6.5.: Complete CFD results

For $V_w = 4.5m/s$ the turbine presents a different behaviour: while the other cases have a sharp peak, as in a significant decline after the maximum value is reached, in this case the decrease in power coefficient is initially more gentle. The cases at $V_w = 6m/s$ and $9m/s$ show instead coherent behaviour. So while in the first case we have $C_{p,max} = 0.254$ for $\lambda = 1.00$, in the latter ones the maximum is located at $\lambda = 1.25$, with $C_{p,max} = 0.296$ and $C_{p,max} = 0.326$, respectively. This difference can be justified by the low value of the in-flow velocity, this in turn results in very low Reynolds number, thus delaying separation. This in turn allows the device to more efficiently extract energy from the airflow.
The following table resumes all results.

	$C_p[1]$						
$\lambda[1]$	0.25	0.50	0.75	1.00	1.25	1.50	1.75
$4.5m/s$	0.000	0.056	0.118	0.254	0.250	0.238	0.146
$6m/s$	0.000	0.065	0.133	0.261	0.296	0.252	0.142
$9m/s$	0.000	0.076	0.160	0.305	0.326	0.295	0.162

Comparing this results with the wind tunnel ones once again shows a clear overestimation of the performances: we can see in Fig. 6.6.(a) how the point of maximum efficiency is correctly captured by the computational model, but with a significantly inflated value. It is therefore reasonable to expect the same behaviour for the other tested conditions.

In the same vein, the region of low-λs shows a remarkable agreement between simulation and empirical data, with a slight overshoot.

In Section 5.2.2 we highlighted the presence of an inflection point in the power curve around $\lambda = 0.5$ for wind tunnel data, while QBlade presented near-linear growth in this

region. This same inflection point is present in the CFD data, although it appears to be delayed at higher TSRs. We once again have to stress the significant differences between the experimental case and the simulated one as a possible cause of this difference in behaviour. Additionally the wide spacing of data points doesn't allow to correctly locate this point.

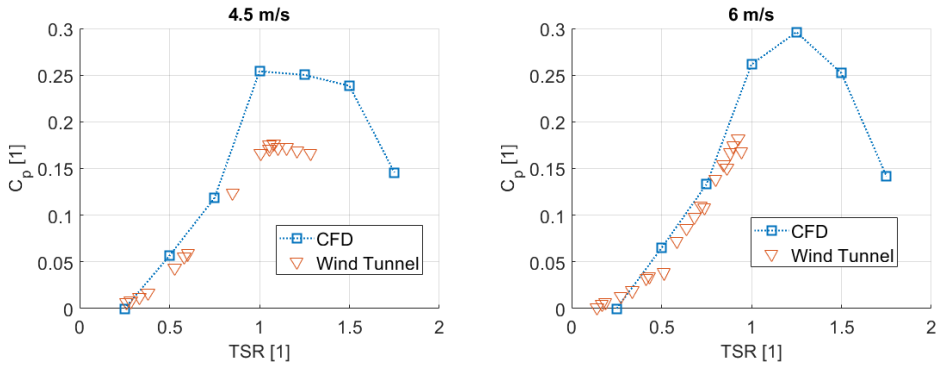

(a) $V_w = 4.5m/s$ (b) $V_w = 6m/s$

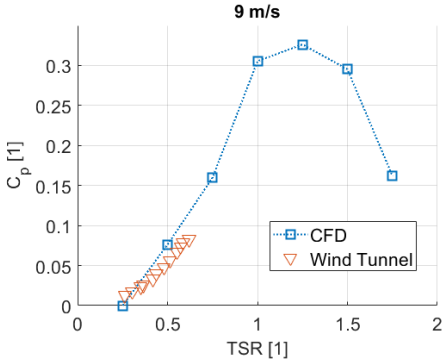

(c) $V_w = 9m/s$[a]

[a] The wind tunnel results are actually relative to the test at $8m/s$.

Figure 6.6.: Comparison with wind tunnel results

6.2.1. Flow-field characteristics - Influence of velocity

Fig. 6.7 shows the flow-field for $\lambda = 1.0$ for the different wind-speeds.

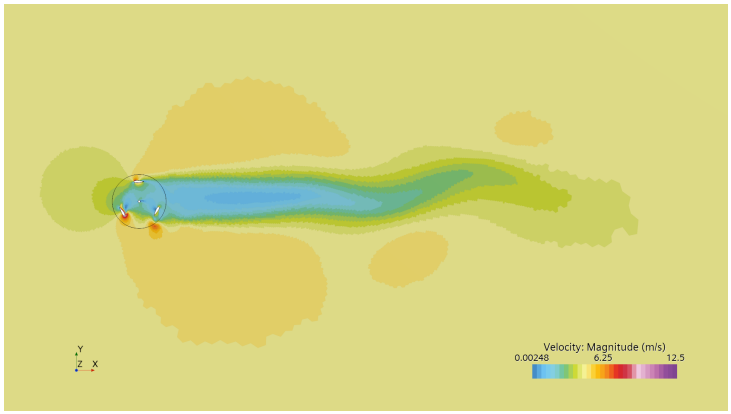

(a) $V_w = 4.5m/s$

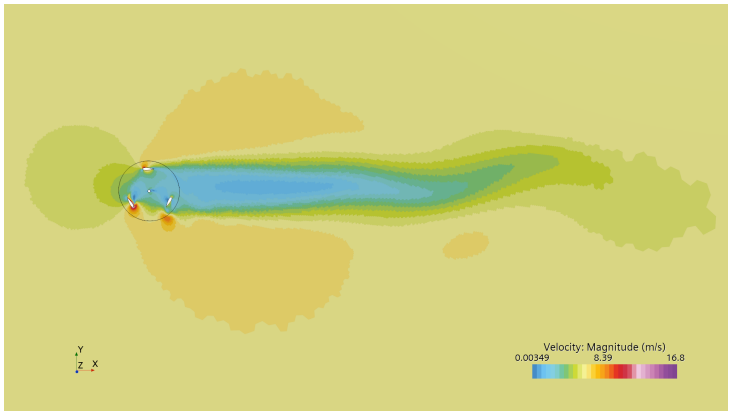

(b) $V_w = 6m/s$

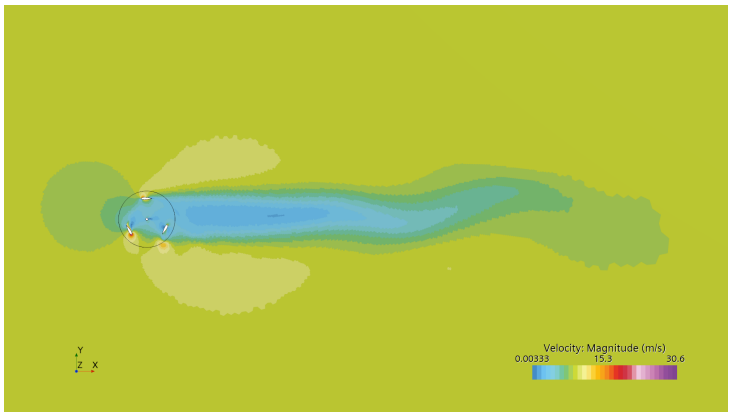

(c) $V_w = 9m/s$

Figure 6.7.: Velocity field

All cases present the same salient characteristics, specifically a rapidly dissipating wake with a slight upward[1] kick. The same asymmetry is evident in the expansion zones, both upstream and downstream. This can be qualitatively evidenced by the velocity deficit aft of the turbine in Fig. 6.8, captured roughly 5 diameters downstream.

[1]More properly the wake curves towards the left, but for clarity's sake a nomenclature coherent with the images was chosen.

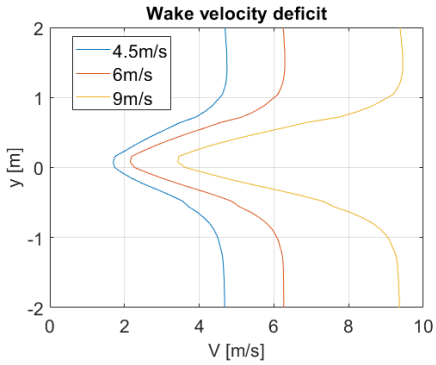

Figure 6.8.: Velocity deficit in the wake @ $x = 5m$

The asymmetry is readily justified by considering the turbine's motion, against the wind in the upstroke, while for the downstroke it adds to airflow momentum. The wake core is not centred, but instead is slightly raised with respect to the turbine central shaft. Similarly, flow in the downward region is slightly accelerated.

In Fig. 6.9 the Turbulent Kinetic Energy, in logarithmic scale can be observed.

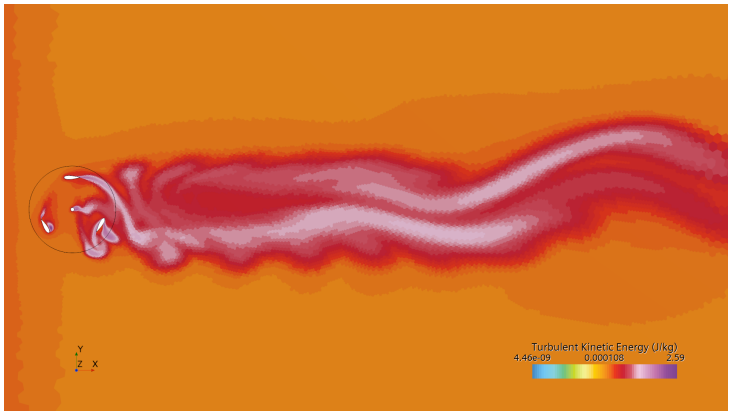

(a) $V_w = 4.5m/s$

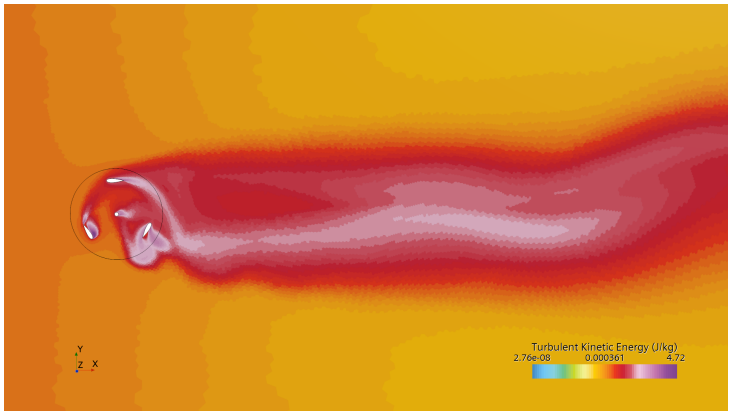

(b) $V_w = 6m/s$

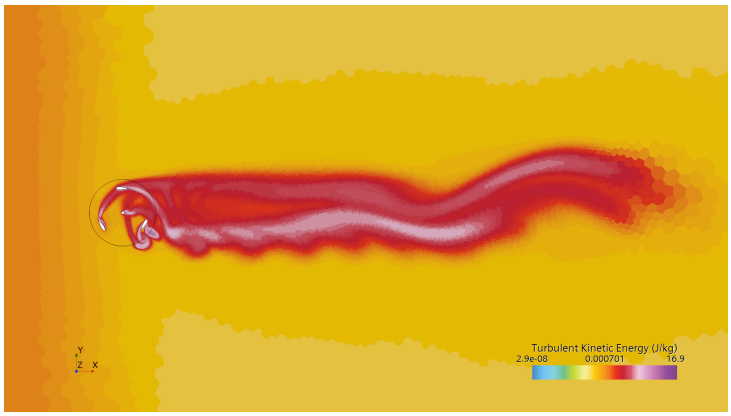

(c) $V_w = 9m/s$

Figure 6.9.: Turbulent Kinetic Energy

As predicted, simulations with $V_w = 9m/s$ show a significant increase in turbulence. The detailed view in Fig 6.10 show how, while for the blades located at $\theta = 0, 4\pi/3$ the vortex structure is similar between the three simulations, the vortices around the blade at $\theta = 2\pi/3$ are clearly affected by the upstream velocity.

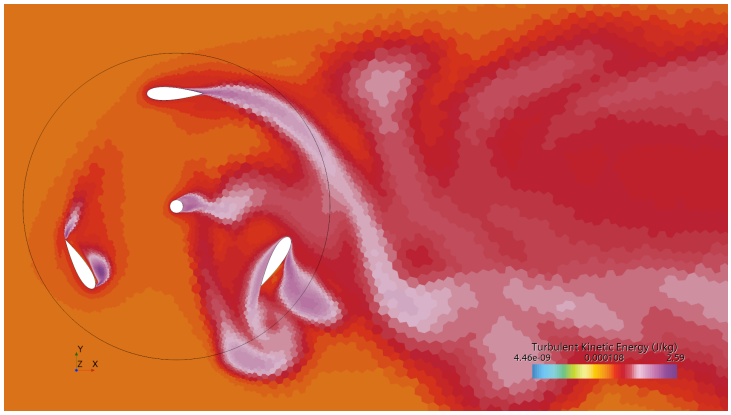

(a) $V_w = 4.5m/s$

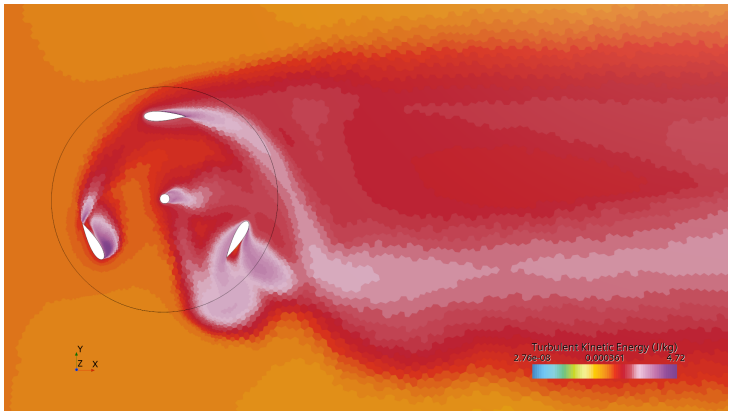

(b) $V_w = 6m/s$

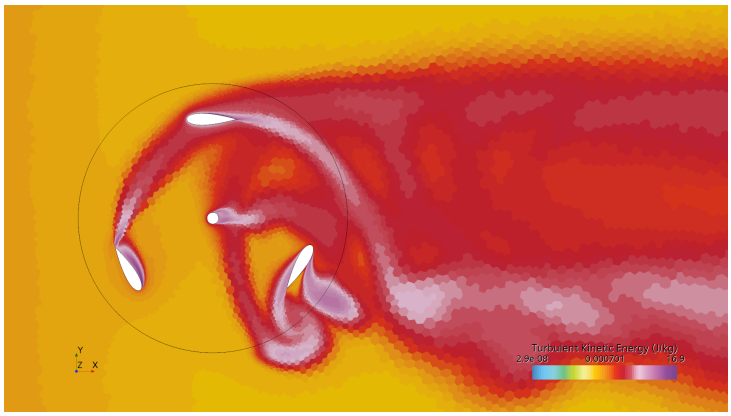

(c) $V_w = 9m/s$

Figure 6.10.: Turbulent Kinetic Energy - Detail

The leading edge vortex grows appreciably between $V_w = 4.5m/s$ and $V_w = 6m/s$ and the flow reattaches at $V_w = 9m/s$. On the other hand, trailing edge turbulence shows a constant increase, both in magnitude and extension, with wind speed. Fig.6.11.(a) shows how the streamtube containing the turbine visibly expands in the near wake region.

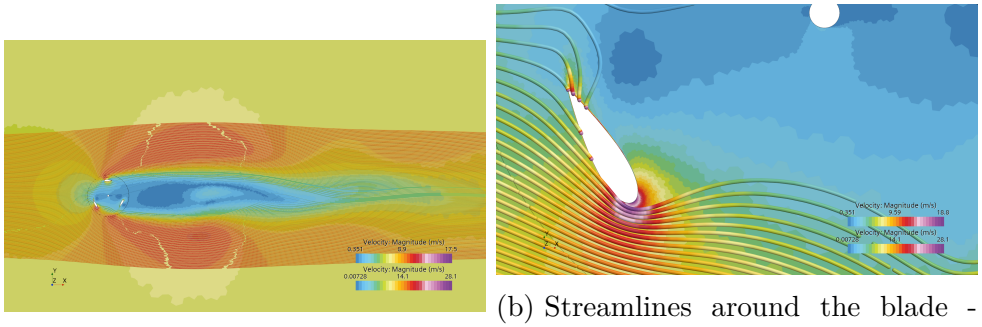

(a) Streamtube - $V_w = 9m/s$

(b) Streamlines around the blade - $V_w = 9m/s$

Figure 6.11.: Streamlines

As expected, the suction side of the airfoil @ $\theta = 2\pi/3$ is a recirculation zone, clearly evidenced in Fig. 6.12.(b), while in Fig. 6.12.(a) we can observe the absence of vortices, and a stagnation point detached from the airfoil and located in the suction side: indeed while the airfoil is symmetric and the apparent angle of attack is null, the presence of a rotating motion results in a translational velocity that, added to the in-flow, results in curved airflow.

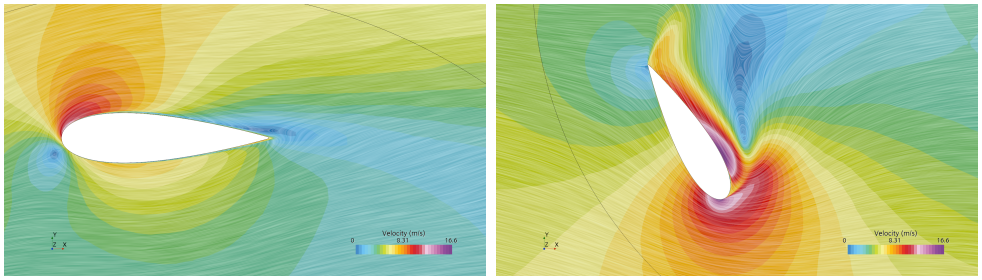

(a) Blade @ $\theta = 0$

(b) Blade @ $\theta = 2\pi/3$

Figure 6.12.: Velocity field, the lines are locally tangent to the direction of the velocity Vector

6.2.2. Flow-field characteristics - Rotation

In this section details of the flow-field in the rotor's disk are presented in the range $\theta = [0; 7\pi/12]$ with $\Delta\theta = \pi/12$. All cases are relative to $\lambda = 1.0$ and $V_w = 6m/s$. All consideration will be made taking as subject the blade initially in position $\theta = 0$ (i.e. the horizontal one), given the polar symmetry the other blades are used for the remaining part of the revolution.

Several observation can be made from Fig. 6.13:

- the stagnation point moves progressively toward the trailing edge until, for $\theta = 2\pi/3$, the flow enters the separation phase and an expansion zone begins to form at the leading edge, grows for $\theta = \pi/3$ until once the blade reaches $\theta = 13\pi/12$ this expansion zone detaches to form a wake vortex. At this point we have a new stagnation point;
- the central shaft sheds a regular Von Karmann wake with added cross-wise momentum due to its rotation;

- the wake starts toward the trailing edge as clearly visible in Fig. 6.12.(a) to then expand on the compression side of the blade until for $\theta = \pi/2$ the wake seems to start at the trailing edge. This is caused by the superposition of the two motions: the rotational motion generates the trailing component while the translational one gradually moves it down-wind until it separates and contributes to the low-velocity inner region.

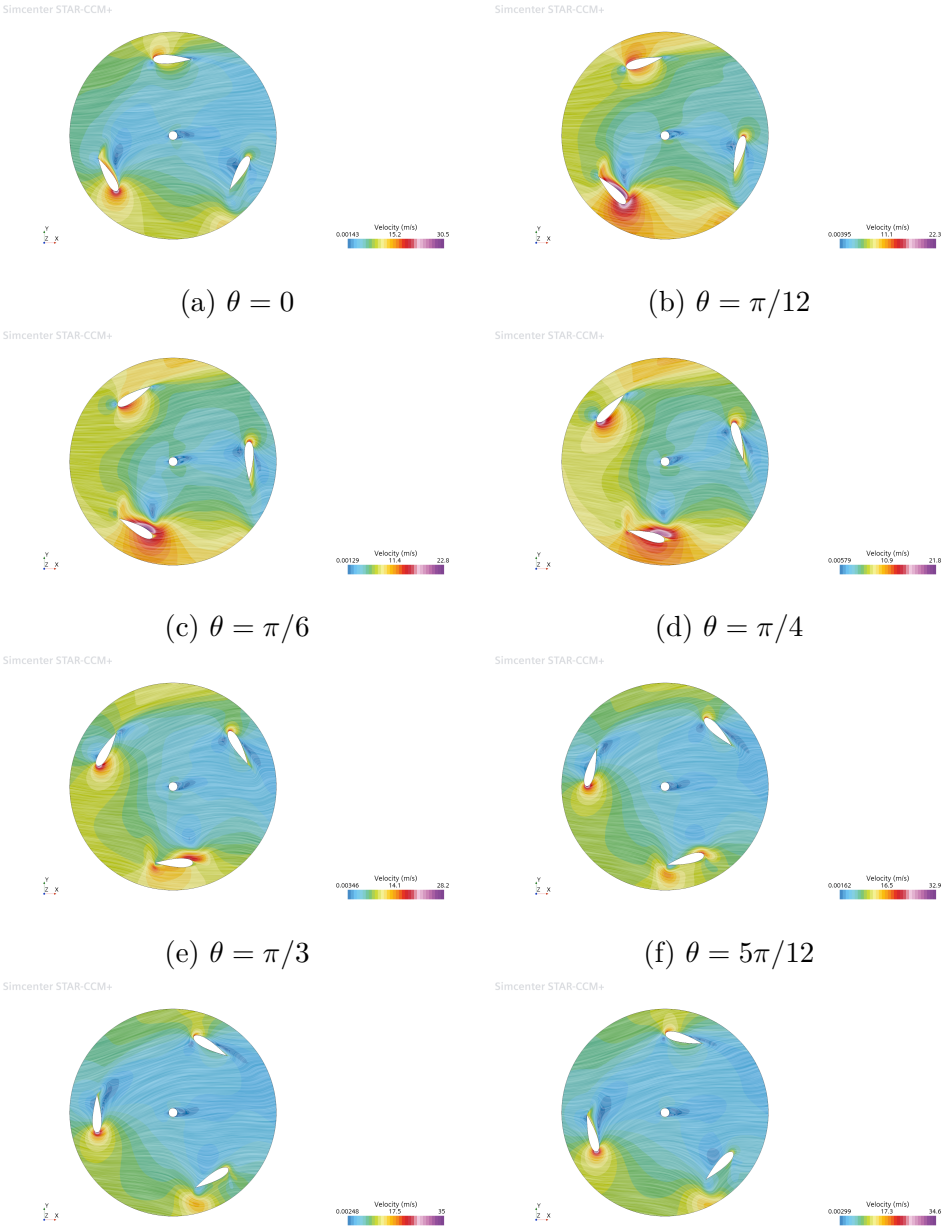

(a) $\theta = 0$ (b) $\theta = \pi/12$

(c) $\theta = \pi/6$ (d) $\theta = \pi/4$

(e) $\theta = \pi/3$ (f) $\theta = 5\pi/12$

(g) $\theta = \pi/2$ (h) $\theta = 7\pi/12$

Figure 6.13.: Velocity field in the rotating region

This is well corroborated in Fig. 6.14: the blade initially produces turbulence only in the leading edge area, a second high turbulence area starts to form in the inner part of the blade trailing edge that grows rapidly. Trailing edge turbulence starts to separate at $\theta = \pi$ to form the aforementioned wake vortex while leading edge turbulence gradually reattaches and moves toward the trailing edge to form the wake of the following revolution.

The strong interaction between the different blades' turbulent structures can be clearly seen: each blade starts the revolution in the preceding blade's wake; this wake, once properly developed interacts directly with the following blade wake and that of the shaft. This all contributes to the increase in turbulence in the flow-field.

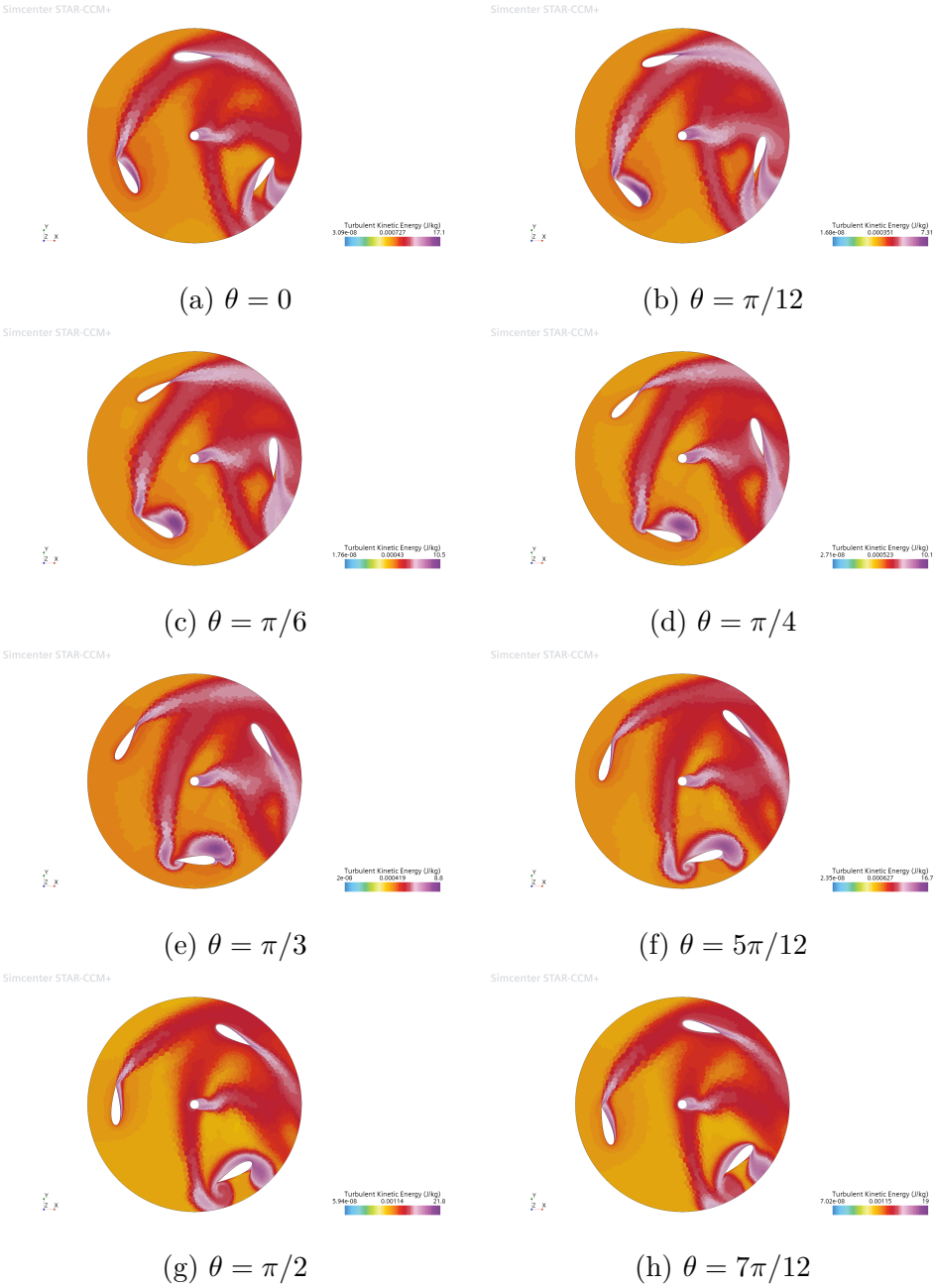

(a) $\theta = 0$ (b) $\theta = \pi/12$

(c) $\theta = \pi/6$ (d) $\theta = \pi/4$

(e) $\theta = \pi/3$ (f) $\theta = 5\pi/12$

(g) $\theta = \pi/2$ (h) $\theta = 7\pi/12$

Figure 6.14.: Turbulent kinetic energy field in the rotating region

6.2.3. Flow-field characteristics - Influence of TSR

In this section different TSRs will be considered for an upstream velocity of $6m/s$ in order to appreciate how this parameter directly influences the flow-field around the turbine.

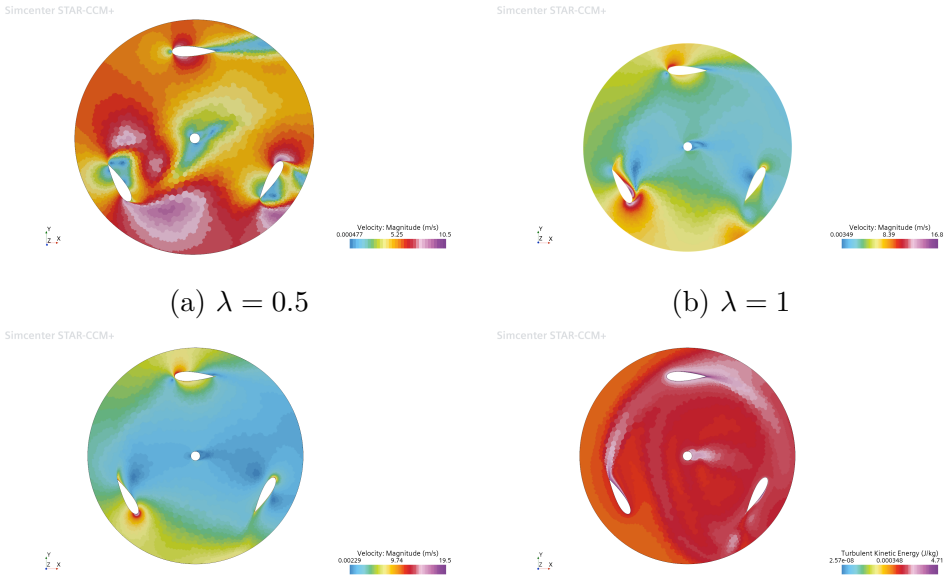

(a) $\lambda = 0.5$ (b) $\lambda = 1$

(c) $\lambda = 1.5$ (d) $\lambda = 1.5$ - T.K.E.

Figure 6.15.: Flow-field in the rotating region for different TSR conditions

As expected the airflow becomes progressively more regular as the TSR increases, expansion zones and wakes tend to decrease in extension; this may be due to the fact that as the rotational speed increases it tends to dominate the translational component. In any case the high gradients present in the velocity field in the case of $\lambda = 0.5$ can certainly be taken as a justification of the high instability. Comparison between Fig 6.15.(d) and Fig. 6.14.(a) shows a sharp decrease in turbulent kinetic energy both in magnitude and in extension of the turbulent zones.

Finally we note how the blade in position $\theta = 0$ in Fig. 6.15.(a) presents a stagnation point corresponding to an approximately null angle of attack contrary to what was observed before.

6.2.4. Flow-field characteristics - Comparison with 3D Simulation

After the 2D simulations were completed, a 3D simulation was run for the case ($\lambda = 1.0, V_w = 4.5m/s$). The same exact model was implemented in the 3D case, with a grid roughened by a factor of 10.

However, this wasn't a quantitative simulation: indeed it was found that with a grid of roughly $1.5e6$ cells each time-step took $50s$. Therefore it was not feasible to conduct a sensitivity analysis on the grid.

Nonetheless the simulation was run to convergence: as expected, given the low cell count, the result was unsatisfactory, resulting in $C_p = 0.06$ after convergence was reached, roughly one-third of the experimental datum. What was intended with this simulation was to shed some light on the extremity effects on the flow field.

Indeed we can see in Fig. 6.16 how there are significant differences in the flow-field. Some of these differences could be imputed to the absence of the central shaft, however the structures are significantly different:

- the flow-field around the blade in position $\theta = 0$ is completely different: the stagnation point in the 3D case moves toward the centre line, this causes a reduced

expansions and a more developed wake;

- the blade in position $\theta = 2\pi/3$ shows instead a more coherent behaviour: expansion zones and re-circulation bubble present similar shapes, even though in the tridimensional case they are significantly more developed, here the absence of the shaft is certainly felt on the shape and extension of the bubble;
- a similar behaviour is evident for the third blade;
- finally we note how the flow is significantly more accelerated in the bidimensional case.

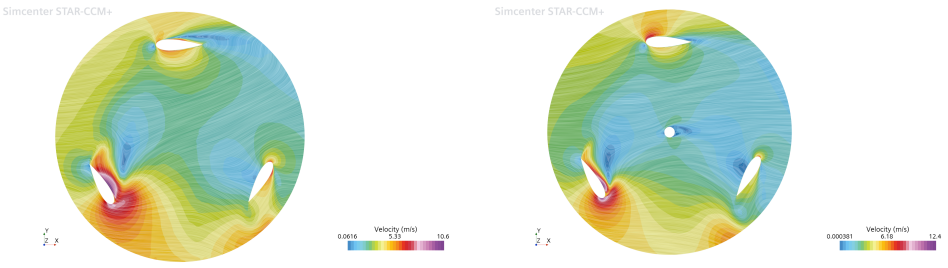

(a) 3D Simulation - Mid plane (b) 2D Simulation

Figure 6.16.: Comparison between 3D and 2D simulations: Velocity

This same can be observed by examining Fig. 6.17 where the turbulent kinetic energy is represented: here also we observe significantly more developed turbulent structures.

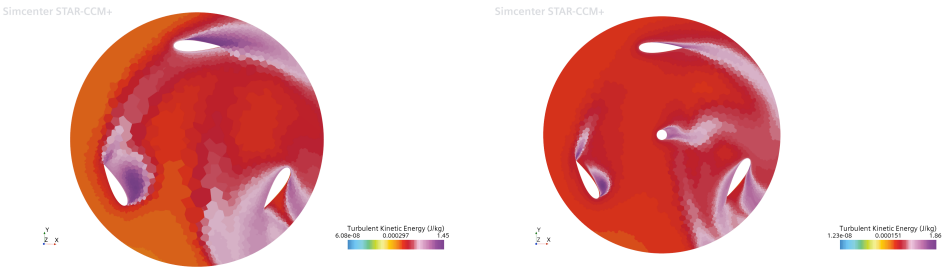

(a) 3D Simulation - Mid plane (b) 2D Simulation

Figure 6.17.: Comparison between 3D and 2D simulations: Turbulent Kinetic Energy

Finally in Fig. 6.18 we can observe how the flow-field developed vertically: in both cases an almost symmetrical behaviour was observed, the same structures present in the mid-plane are reproduced along the height of the blades, they are however reduced in size.

This is more evident in Fig. 6.18.(g) where a vertical section of the velocity field is presented: clearly the flow tends to expand further away from the mid-plane. Some other salient characteristics are also visible:

- the wake core is almost perfectly conical;
- wake and expansion bubble both interact with the boundary layer forming on the ground: while fore of the turbine we denote an destabilization of the former, aft of

it the interaction doesn't allow the flow to return to the undisturbed velocity, thus presenting an additional source of losses;

- shed vortices are clearly visible for two blades, they are, however, relatively small.

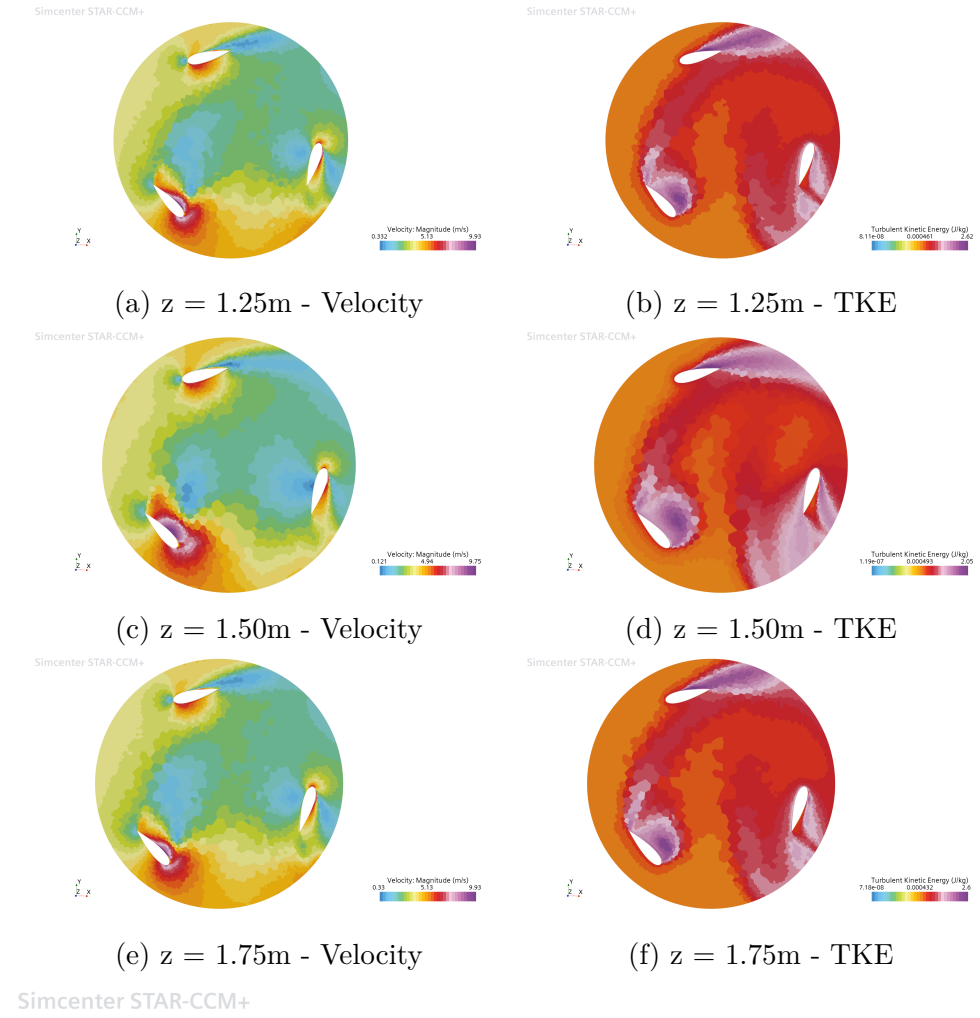

(a) z = 1.25m - Velocity

(b) z = 1.25m - TKE

(c) z = 1.50m - Velocity

(d) z = 1.50m - TKE

(e) z = 1.75m - Velocity

(f) z = 1.75m - TKE

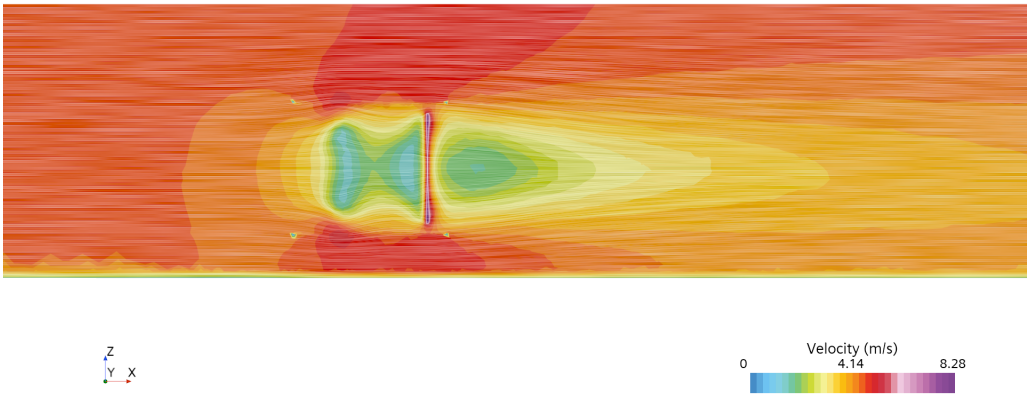

(g) y = 0m - Velocity

Figure 6.18.: Turbulent kinetic energy field in the rotating region

7. Conclusions

To conclude the simulations were found to be overall adequate:

- a remarkable agreement was found in the low-TSR regimes for both kind of simulations;
- the CFD model correctly captures the shape of the power curve but shows a consistent overshoot in C_p values for higher-TSRs;
- while QBlade simulation can be considerate fungible in low-TSR regimes, they completely fail for $\lambda > 1.0$ with a strong divergence from the empirical data and an overestimation of the operational range.

Additional empirical data may shed more light on the adequacy of the CFD model: we were able to present complete results only for $V_w = 4.5m/s$; while we can certainly extrapolate the behaviour from the data points available, more concrete evidence is needed. In any case for $\lambda < 1.0$ the difference between computed and measured data is negligible, especially considering the 1st-order discretization and the bi-dimensionality of the simulations. Indeed the overestimation can be in part attributed to the absence of extremity effects and the subsequent loss of efficiency.

In Fig. 7.1 and 7.2 the complete results are reported.

Fig. 7.1 clearly highlights the different models' strengths: while QBlade clearly captures the turbine performance at low TSR more accurately, as evidenced in Fig. 7.2, CFD simulations are a more apt predictor of the overall performance: they clearly minimize the deviation from empirical data while correctly capturing the curve shape.

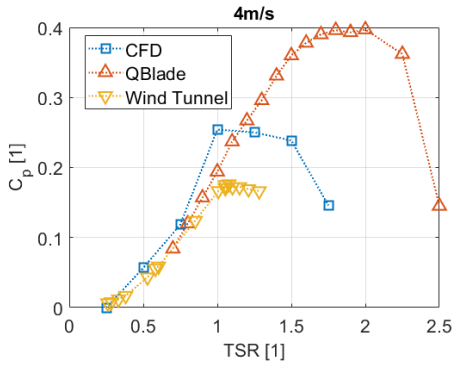

(a) $V_w = 4.5m/s$

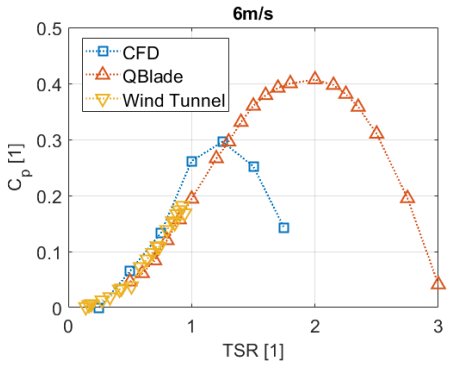

(b) $V_w = 6m/s$

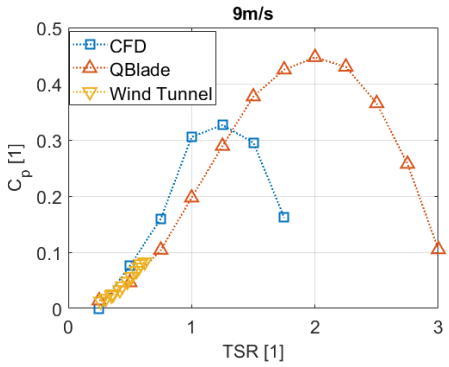

(c) $V_w = 9m/s$

Figure 7.1.: Complete results

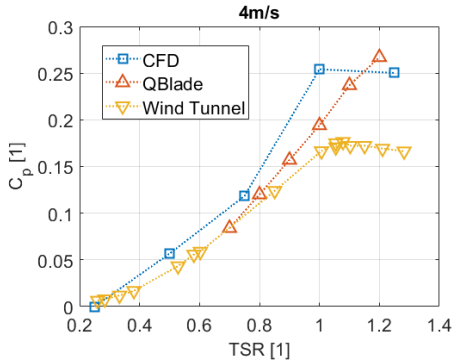

(a) $V_w = 4.5m/s$

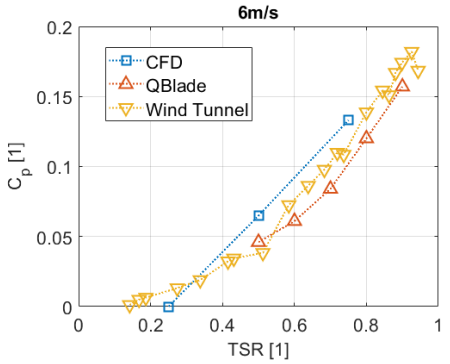

(b) $V_w = 6m/s$

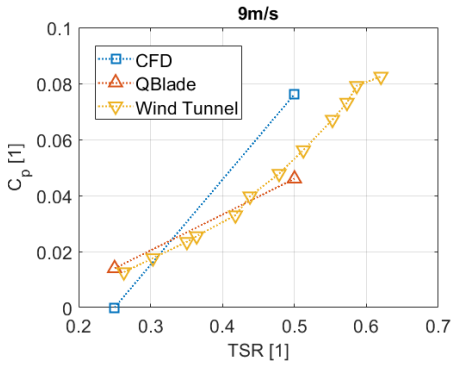

(c) $V_w = 9m/s$

Figure 7.2.: Simulation results limited to those regimes experimentally investigated

Therefore QBlade can, for the moment, be considered only an accurate predictor of the differences in performances between different conditions. However, small improvements in the simulation model can certainly increase results' accuracy, both in magnitude and overall behaviour. In order to achieve this, additional empirical data is needed for a calibration of different parameters. With this set of data an initial calibration would be based only on the first data-set, without additional information on the accuracy at higher wind speeds.

The CFD model on the other hand can be considered satisfactory: while from the literature review much more stringent requirements seem to be needed, we have found satisfying results with our model. A second analysis, using a 2nd-order discretization should in theory improve the quality of the result. There are however certain drawbacks:

- in order to properly reach convergence a finer discretization, both in time and space, would be needed, significantly inflating computation time;
- the flow field remains fully tri-dimensional: as we have seen in Section 6.2.2 turbulence plays an essential role in the turbine behaviour and therefore we can expect accurate results only from a 3D simulation. We weren't able to obtain an accurate 3D simulation, however the results reported in Section 6.2.4 clearly evidence the need for a tridimensional analysis in order to obtain complete results.

In any case this model can be considered as an accurate predictor of performance in the initial design phase.

Overall the turbine performance was found to be more than satisfying:

- excellent self-starting capabilities were found even at low speeds; this however depends on the initial position of the blades relative to the incoming airflow: it was found that positioning the blades as in Fig. 6.14h would always result in an auto-start, in this case a simple positional control would be needed in order to guarantee self-starting;
- the turbine operates mainly in the low-TSR regimes: while on one hand this significantly complicates the flow-field, on the other results in less stringent mechanical requirements, and therefore a longer service-life;
- maximum efficiency was reached in the condition $V_w = 6m/s$, $\lambda = 0.926$ resulting in $C_p = 0.182$, however this doesn't constitute a maximum point for that particular curve or overall, indeed by taking the behaviour observed in both CFD and QBlade simulations we expect this value to grow at higher TSRs and in-flow velocities.

A. Turbulence Models

A.1. Turbulent Viscosity Hypothesis

The turbulent viscosity hypotesis, introduced by Bussinesq in 1877, is a closure model for the Reynolds equations. According to it, the Reynolds stresses are directly proportional to the mean rate of strain, so that

$$-\rho u_i \bar{u}_j + \frac{2}{3}\rho k \delta_{ij} = \nu_T \left(\frac{\partial \bar{U}_i}{\partial x_j} + \frac{\partial \bar{U}_j}{\partial x_i} \right),$$

where ν_T is the turbulent, or eddy, viscosity. This allows to rewrite the Reynolds' momentum equation in an analogous form to that of the Navier-Stokes equation, with $\nu_{eff} = \nu + \nu_T$, which is of course a function of both time and space. It can be seen how this implies that the anisotropy tensor, $a_{ij} = u_i \bar{u}_j - \frac{2}{3} k \delta_{ij}$, is aligned with the mean rate of strain tensor, $\bar{S}_{ij}$. Therefore their components should be related by $a_{ij} = -2\nu_T \bar{S}_{ij}$.

The hypotesis doesn't have a general basis: if we consider homogeneous turbulence forced to pass in an axysimmetric contraction, it can be shown how the Reynolds stresses are determined by the total amount of mean strain experienced by the turbulence and not by its local value. Indeed the anisotropies generated in the contraction persist in the following straight section because they decay with the turbulence time-scale k/ϵ. However in flows where the turbulence characteristics and mean velocity gradients change very slowly, and the ratio of production to dissipation is close to unity, the Reynolds stresses are governed by local phenomena and the assumption can be considered valid. In order to extend the validity of the hypotesis, a non linear relation must be employed in order to account for the misalignement between a_{ij} and $\bar{S}_{ij}$.

If the hypotesis is nevertheless accepted as an adequate approximation, the turbulent viscosity can be written as a product of a charachteristic length and a charachteristic velocity (from simple dimensional analysis). The problem then becomes centered on the determination of this charachteristics dimensions.

A.2. $k - \epsilon$ Model formulation

The model solves transports equations for the two quantities, from these we can construct a length-scale, $L = k^{3/2}/\epsilon$, a time-scale, $\tau = k/\epsilon$, and all the derivative ones. The need for flow-dependent specification is then dealt with and the model is considered complete.

The standard $k - \epsilon$ model was first developed in 1972 by Jones and Launder [14], but it's in constant evolution. The current formulation of the *standard* $k - \epsilon$ model is as follow:

- turbulent kinetic energy:

$$\frac{\partial}{\partial t}(\rho k) + \frac{\partial}{\partial x_i}(\rho k u_i) = \frac{\partial}{\partial x_j}\left[\left(\mu + \frac{\mu_t}{\sigma_k} \frac{\partial k}{\partial x_j} \right) \right] + P_k + P_b - \rho\epsilon - Y_M + S_k;$$

- dissipation:

$$\frac{\partial}{\partial t}(\rho\epsilon) + \frac{\partial}{\partial x_i}(\rho\epsilon u_i) = \frac{\partial}{\partial x_j}\left[\left(\mu + \frac{\mu_t}{\sigma_\epsilon}\frac{\partial \epsilon}{\partial x_j}\right)\right] + C_{1\epsilon}\frac{\epsilon}{k}(P_k + C_{3\epsilon}P_b) - C_{2\epsilon}\rho\epsilon\frac{\epsilon}{k} + S_\epsilon;$$

where:

- μ_t is the turbulent viscosity, formulated as

$$\mu_t = \rho C_\mu \frac{k^2}{\epsilon};$$

- P_k is the production term,

$$P_k = \mu_t S^2,$$

  with S modeulus of the mean rate of strain tensor, $S = \sqrt{2S_{ij}S_{ij}}$;

- P_b accounts for buoyancy effects and can be negelected in isothermal flows;

The model constants are

- $C_{1\epsilon} = 1.44$;
- $C_{2_\epsilon} = 1.92$;
- $C_\mu = 0.09$;
- $\sigma_k = 1.0$;
- $\sigma_\epsilon = 1.3$;

Different formulations of this model exists, but are all based on the same basic idea. Notable ones are the *realizable* $k-\epsilon$ and the *Re-Normalization Group (RNG)* $k-\epsilon$.

A.3. SST Model

A.3.1. Transformed $k-\epsilon$

The SST model blends the $k-\epsilon$ and $k-\omega$ models. This requires a re-formulation of the standard $k-\epsilon$ model. Using the definition of ϵ and ω, one can be substitued to the other with some modifications. The resulting model is then:

- turbulent kinetic energy equation:

$$\frac{\partial}{\partial t}(\rho k) + \frac{\partial}{\partial x_j}(\rho u_j k) = \tau_{ij}\frac{\partial u_i}{\partial x_j} - \beta^*\rho\omega k + \frac{\partial}{\partial x_j}\left[(\mu + \sigma_{k2}\mu_T)\frac{\partial k}{\partial x_j}\right];$$

- specific dissipation rate equation:

$$\frac{\partial}{\partial t}(\rho\omega) + \frac{\partial}{\partial x_j}(\rho u_j \omega) = \frac{\gamma_1}{\nu_T}\tau_{ij}\frac{\partial u_i}{\partial x_j} - \beta_2\rho\omega^2 + \frac{\partial}{\partial x_j}\left[(\mu + \sigma_{\omega 2}\mu_T)\frac{\partial \omega}{\partial x_j}\right] + 2\rho\sigma_{\omega 2}\frac{1}{\omega}\frac{\partial k}{\partial x_j}\frac{\partial \omega}{\partial x_j}$$

The constants of the model are presented in the following section.

A.3.2. SST model's constants and definitions

The constants that appear in the model are blended in the same way as the variables $\phi = F_1\phi_1 + (1 - F_1)\phi_2$.

For the Wilcox $k - \omega$ model the constants are modified to be:

$$\sigma_{k1} = 0.85, \quad \sigma_{\omega 1} = 0.5, \quad \beta_1 = 0.0750, \quad a_1 = 0.31$$

$$\beta^* = 0.09, \quad \kappa = 0.41, \quad \gamma_1 = \beta_1/\beta^* - \sigma_{\omega 1}\kappa^2/\sqrt{\beta^*}.$$

while for the transformed $k - \epsilon$:

$$\sigma_{k2} = 1.0, \quad \sigma_{\omega 2} = 0.856, \quad \beta_2 = 0.0828,$$

$$\beta^* = 0.09, \quad \kappa = 0.41, \quad \gamma_2 = \beta_2/\beta^* - \sigma_{\omega 2}\kappa^2/\sqrt{\beta^*}.$$

$CD_{k\omega}$, employed in the defintion of arg_1, represents the positive portion of the cross diffusion term in the equation in ω and is formulated as

$$CD_{k\omega} = \max\left(2\rho\sigma_{\omega 2}\frac{1}{\omega}\frac{\partial k}{\partial x_j}\frac{\partial \omega}{\partial x_j}, 10^{-20}\right).$$

The modification of the eddy viscosity $\nu_t = \frac{a_1 k}{max(a_1\omega;\Omega F_2)}$, requires a second auxiliary function

$$F_2 = \tanh(\arg_2^2),$$

where

$$\arg_2 = \max\left(2\frac{\sqrt{k}}{0.09\omega y}, \frac{500\nu}{y^2\omega}\right)$$

A.4. $\gamma - Re_\theta$ Model

The model couples the formulation described in Section 3.3 with the two transport equations defined in Section 3.4. In the latter two equations there appears a number of additional definitions and constants which were omitted in the main text and are here reported. Additionally, the final formulation, where the transition modeling is coupled with the SST turbulence model, dictates a slight modification to the latter and is reported in Appendix A.4.2.

A.4.1. Definitions and constants

The function F_{onset} was used to trigger the intermittency production and is defined as

$$F_{onset} = \max(F_{onset2} - F_{onset3}, 0),$$

where:

- $F_{onset2} = \min[\max(F_{onset1}, F_{onset1}^4), 2.0]$;
- $F_{onset1} = \frac{Re_\nu}{2.193 Re_{\theta x}}$;
- $Re_\nu = \frac{\rho y^2 S}{\mu}$;

- $F_{onset3} = \max\left[1 - \left(\frac{R_T}{2.3}\right)^3, 0\right]$;
- $R_T = \frac{\rho k}{\mu\omega}$.

The function F_{turb} was used to disable the destruction/relaminarization sources outside of a laminar boundary layer and is defined as

$$F_{turb} = e^{-(R_T/4)^4}.$$

In the source term for the transition momentum thickness, $P_{\theta t}$, appears $t = \frac{500\mu}{pU^2}$, a time-scale utilized for dimensional reasons. The same term contains the blending function

$$F_{\theta t} = \min\left\{\max\left[F_{wake}e^{-(y/\delta)^4}, 1.0 - \left(\frac{y - 1/c_{e2}}{1 - 1/c_{e2}}\right)^2\right], 1.0\right\};$$

where $F_{wake} = e^{-[Re_\omega/(1E+5)]^2}$ and $Re_\omega = \frac{\rho\omega y^2}{\mu}$. The boundary layer dimension, δ, can be computed as

$$\delta = \frac{50\Omega y}{U}\delta_{BL},$$

where

$$\delta_{BL} = 7.5\theta_{BL} \quad \text{and} \quad \theta_{BL} = \frac{\widetilde{Re}_{\theta t}\mu}{\rho U}$$

The constatns employed, as calibrated by Menter, are:

$$c_{e1} = 1.0, \quad c_{a1} = 0.5.$$

$$c_{e2} = 50, \quad c_{a2} = 0.2, \quad \sigma_f = 1.0.$$

$$c_{\theta t} = 0.03, \quad \sigma_{\theta t} = 10.0$$

A.4.2. Coupling with SST Model

When the transition modeling is coupled with the SST turbulence model, the latter assumes a slightly different form.

- turblent kinetic energy:

$$\frac{\partial}{\partial t}(\rho k) + \frac{\partial}{\partial x_j}(\rho k u_j) = \frac{\partial}{\partial x_j}\left[\left(\mu + \mu_t * \sigma_k \frac{\partial k}{\partial x_j}\right)\right] + \tilde{P}_k - \tilde{D}_k;$$

- specific dissipation:

$$\frac{\partial}{\partial t}(\rho\omega) + \frac{\partial}{\partial x_j}(\rho\omega u_i) = \frac{\partial}{\partial x_j}\left[(\mu + \mu_t\sigma_k)\frac{\partial\omega}{\partial x_j}\right] + \alpha\frac{P_k}{\nu_T} - D_\omega + Cd_\omega;$$

where:

- P_k, D_k and D_ω are the production and destruction terms in the original SST model;

- $\tilde{P_k}$ and $\tilde{D_k}$ are modified production and destruction terms due to a reworking of intermittency and are defined as

$$\tilde{P_k} = \gamma_{eff} P_k,$$

$$\tilde{D_k} = \min\left[\max\left(\gamma_{eff}, 0.1\right), 1\right] D_k.$$

- It was observed how the original model tended to predict the reattachment following the separation of a laminar bubble too far downstream. Therefore the modification aims to allow k to grow rapidly once the flow separates, causing earlier reattachment.

  The effective intermittency is defined as

$$\gamma_{eff} = \max\left(\gamma, \gamma_{sep}\right),$$

  where γ_{sep} is

$$\gamma_{sep} = \min\left\{ s_1 \max\left[\left(\frac{Re_\nu}{2.193 Re_{\theta c}}\right) - 1, 0\right] F_{reattach}, 5 \right\} F_{\theta t},$$

  with $F_{reattach} = e^{-(R_T/15)^4}$. The parameter s_1 controls the size of the separation bubble.

Finally, the function F_1 was modified because, in the center of a laminar boundary layer, it could switch from 1.0 to 0.0. Therefore, defining

$$F_3 = e^{-(R_y/120)^8},$$

with $R_y = \frac{\rho y \sqrt{k}}{\mu}$, F_1 becomes:

$$F_1 = \max\left(F_{1,orig}, F_3\right).$$

B. Low-Order Analyses Results

B.1. Airfoil study

In this section are reported the aerodynamic characteristics obtained with STAR CCM+ as described in section 4.1. It is important to note here how the data was computed only for positive angles of attack. A symmetry study was conducted for $Re = 2.5 \cdot 10^5$ and the results were satisfactory. Therefore while the data was directly computed only for positive AoAs, the negative ones have opposite C_l and C_m and same C_d.

For each Reynolds number are reported firstly the tabulated data and then all relevant graphs.

B.1.1. Reynolds = 200000

$\alpha[^\circ]$	$C_l[1]$	$C_d[1]$	$C_m[1]$
0.00	0.00129676	0.03575902	0.00002293
5.00	0.31176154	0.04041619	-0.00275029
8.00	0.48141073	0.04953382	-0.00386679
10.00	0.55958205	0.05991929	-0.00438860
12.00	0.60370852	0.07552844	-0.00462225
14.00	0.58570465	0.09683629	-0.00470604
16.00	0.55276237	0.12391324	-0.00400844

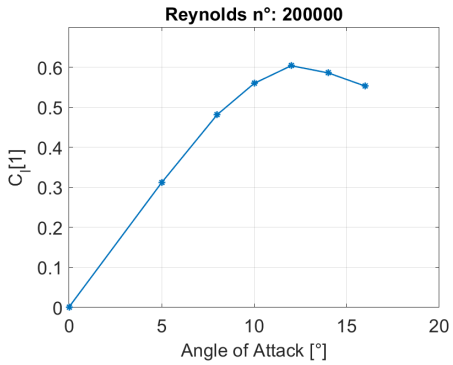

(a) C_l Polar

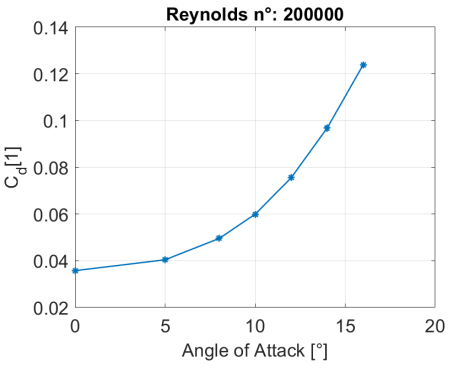

(b) C_d

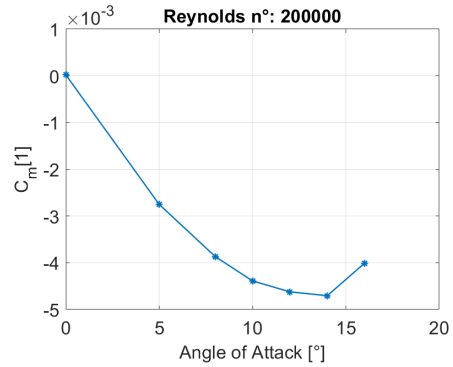

(c) C_m

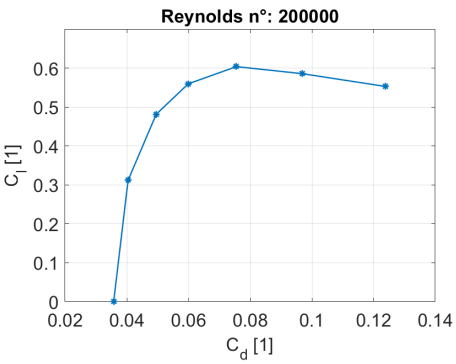

(d) $C_d - C_l$ polar

B.1.2. Reynolds = 250000

$\alpha[°]$	$C_l[1]$	$C_d[1]$	$C_m[1]$
0.00	0.00142612	0.03430214	0.00002537
5.00	0.31751747	0.03878701	-0.00275960
8.00	0.49094278	0.04755573	-0.00390635
10.00	0.57353323	0.05755700	-0.00444151
12.00	0.62425840	0.07293012	-0.00463468
14.00	0.60690317	0.09347036	-0.00484261
16.00	0.57349983	0.12063616	-0.00412767

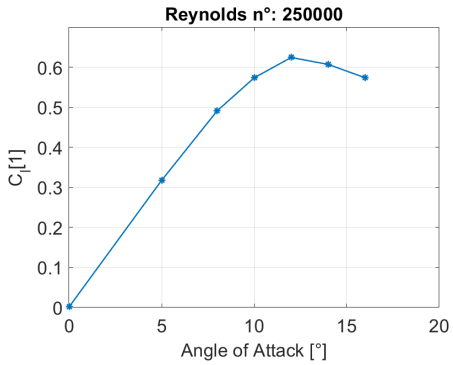

(a) C_l Polar

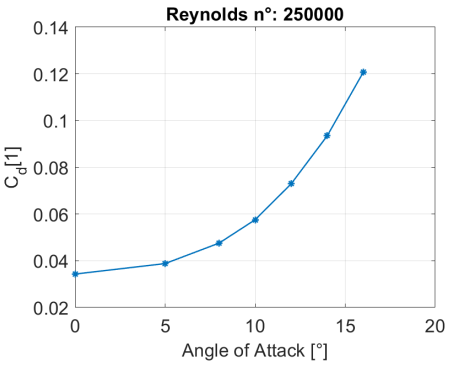

(b) C_d

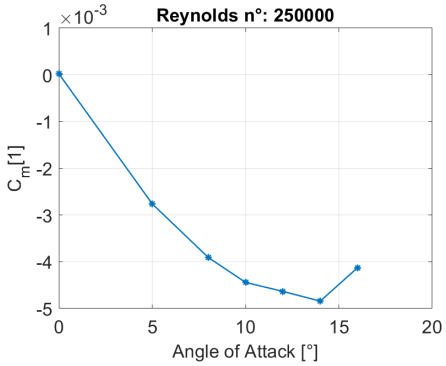

(c) C_m

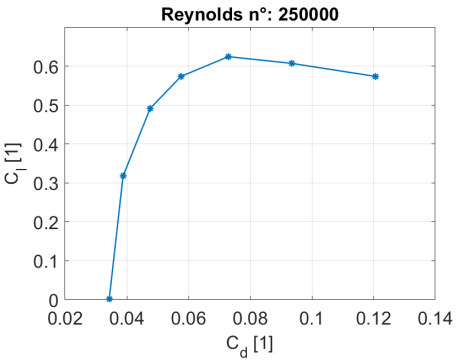

(d) $C_d - C_l$ polar

B.1.3. Reynolds = 300000

$\alpha[°]$	$C_l[1]$	$C_d[1]$	$C_m[1]$
0.00	0.00149545	0.03314852	0.00002647
5.00	0.32349369	0.03747269	-0.00274822
8.00	0.49094278	0.04755573	-0.00390635
10.00	0.58675687	0.05558623	-0.00447188
12.00	0.64056818	0.07036978	-0.00472975
14.00	0.62563626	0.09086631	-0.00491642
16.00	0.59401308	0.11794060	-0.00420719

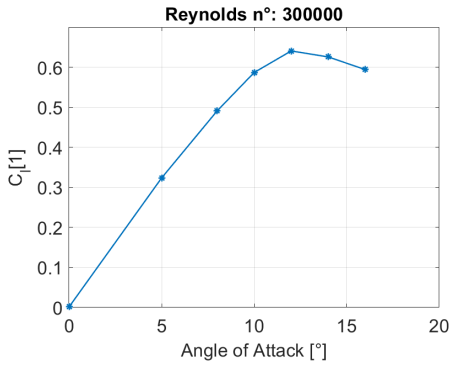

(a) C_l Polar

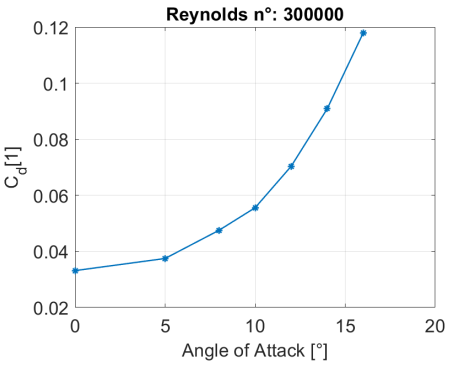

(b) C_d

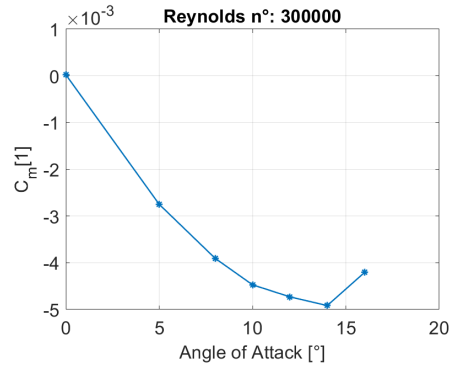

(c) C_m

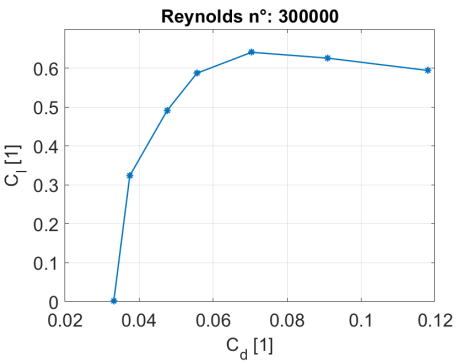

(d) $C_d - C_l$ polar

B.1.4. Reynolds = 350000

$\alpha[°]$	$C_l[1]$	$C_d[1]$	$C_m[1]$
0.00	0.00144261	0.03219352	0.00002568
5.00	0.32845976	0.03639827	-0.00273595
8.00	0.50816926	0.04461095	-0.00392835
10.00	0.59855017	0.05392660	-0.00448643
12.00	0.65403967	0.06843955	-0.00476979
14.00	0.64348377	0.08834405	-0.00499942
16.00	0.61468364	0.11531412	-0.00428553

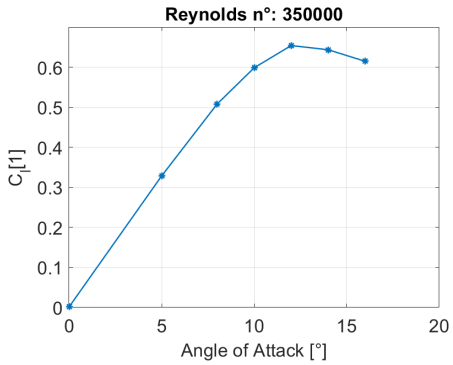

(a) C_l Polar

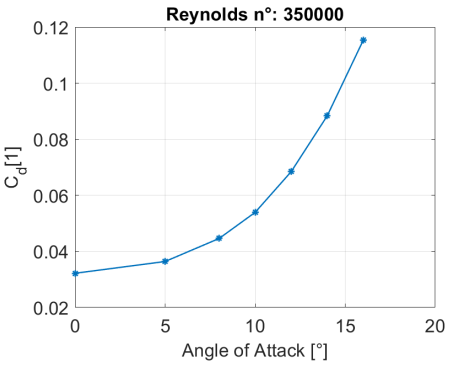

(b) C_d

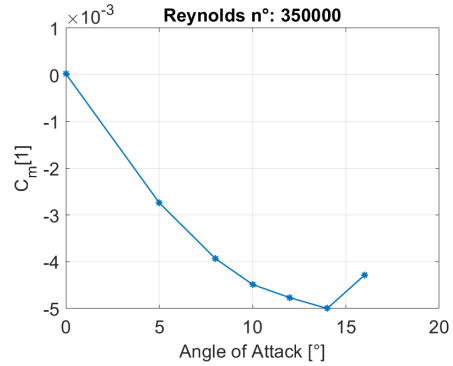

(c) C_m

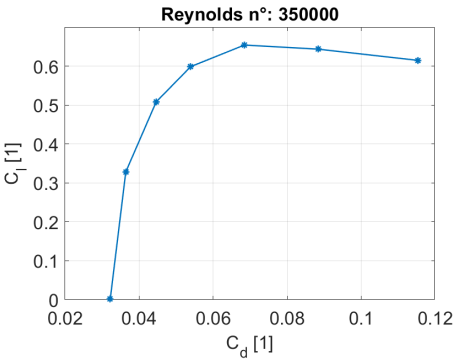

(d) $C_d - C_l$ polar

B.1.5. Reynolds = 400000

$\alpha[°]$	$C_l[1]$	$C_d[1]$	$C_m[1]$
0.00	0.00157413	0.03173265	0.00002774
5.00	0.33303032	0.03547563	-0.00272032
8.00	0.51588311	0.04344135	-0.00392462
10.00	0.61031028	0.05244457	-0.00448630
12.00	0.66765473	0.06659994	-0.00480524
14.00	0.68260202	0.08406112	-0.00512222
16.00	0.65340496	0.11083416	-0.00443857

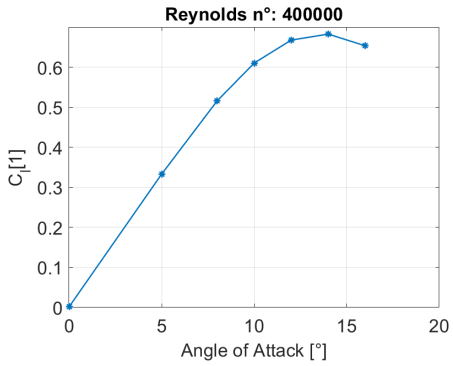

(a) C_l Polar

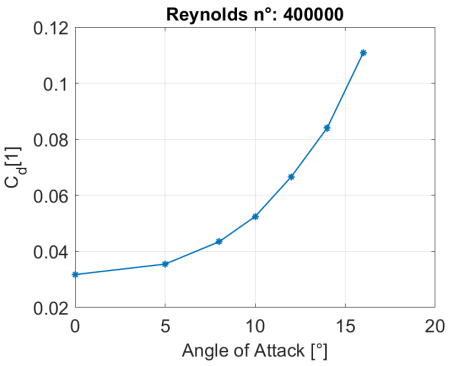

(b) C_d

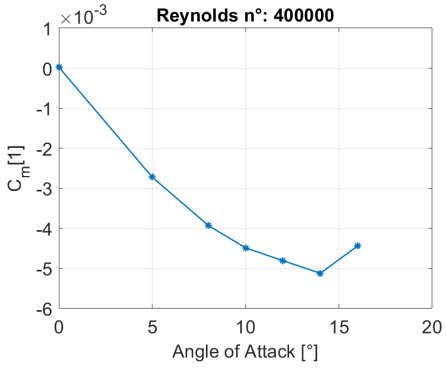

(c) C_m

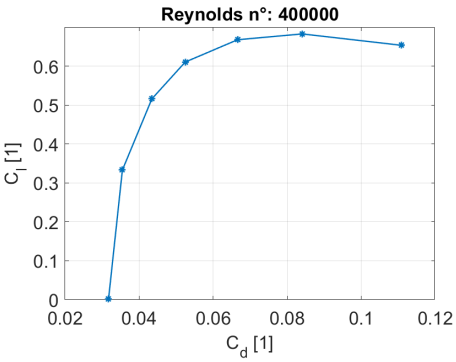

(d) $C_d - C_l$ polar

B.1.6. Reynolds Effect

In the interest of completeness, given the ready available data, it was considered proper to conduct a study on the effect of the Reynolds number on the aerodynamic characteristics.

It was found that the lift coefficient increases with the Reynolds number as expected, and so does the slope of the linear portion of the curve. Interestingly, for $Re = 400000$ there's a delay on stall to $\alpha = 14°$. This isn't entirely surprising, the flow is approaching its critical Reynolds number therefore the transition to turbulence probably caused the delay in separation.

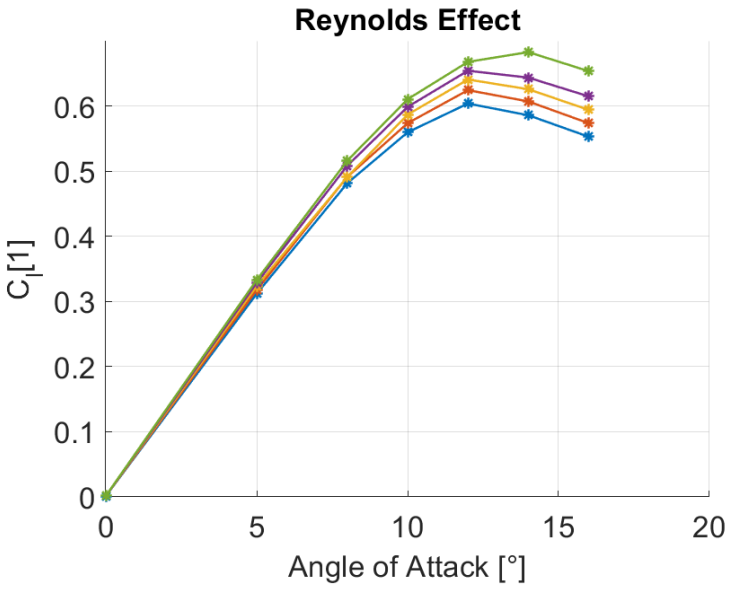

Figure B.6.: C_l

In the same vein, the drag coefficient decreases as the Reynolds number increases.

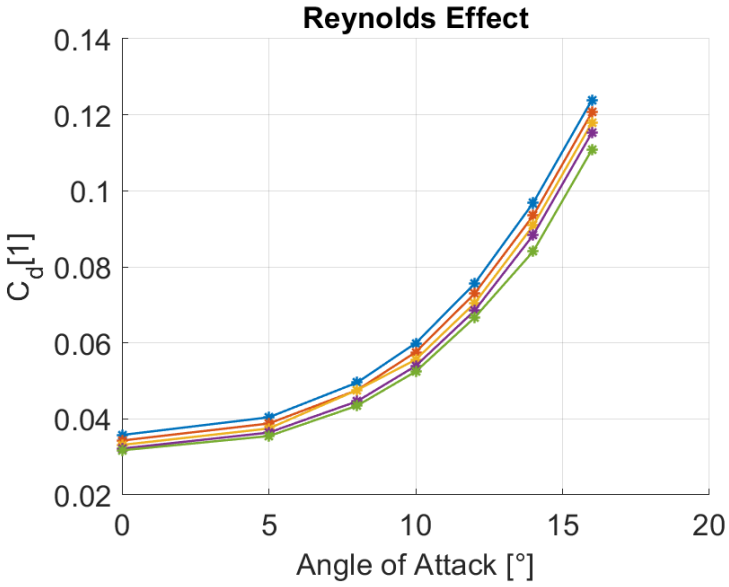

Figure B.7.: C_d

For the moment coefficient the behaviour is slightly different: up to $\alpha = 8°$ the Reynolds number seems to have no effect on the C_m, after that AoA, the curves fan and once again it was found how the value increases, in absolute value, with the Reynolds number.

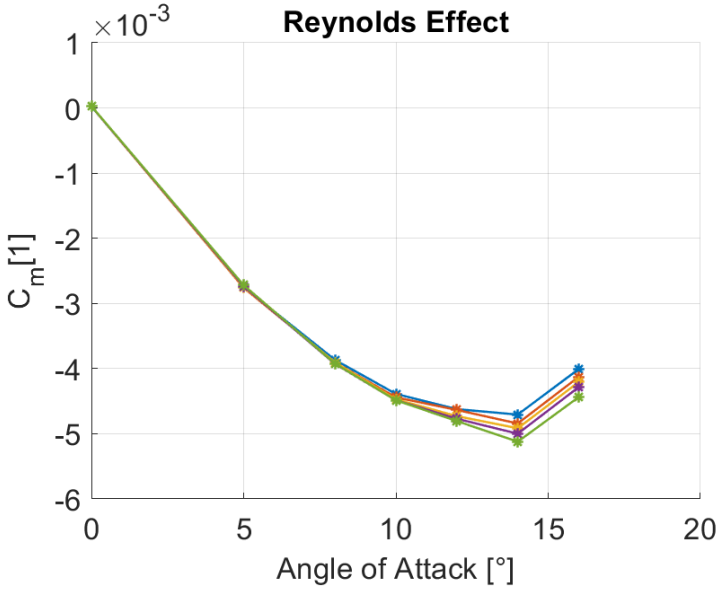

Figure B.8.: C_m

B.2. Operational range

4m/s	
λ [1]	C_p [1]
0.50	0.014
0.60	0.046
0.70	0.084
0.80	0.120
0.90	0.157
1.00	0.194
1.10	0.237
1.20	0.267
1.30	0.296
1.40	0.331
1.50	0.360
1.60	0.378
1.70	0.390
1.80	0.396
1.90	0.393
2.00	0.397
2.25	0.362
2.50	0.145

6m/s	
λ [1]	C_p [1]
0.50	0.046
0.60	0.061
0.70	0.084
0.80	0.120
0.90	0.157
1.00	0.194
1.20	0.266
1.30	0.296
1.40	0.331
1.50	0.360
1.60	0.379
1.70	0.392
1.80	0.400
2.00	0.407
2.15	0.397
2.25	0.381
2.35	0.358
2.50	0.310
2.75	0.195
3.00	0.041

8m/s	
λ [1]	C_p [1]
0.50	0.046
0.60	0.062
0.70	0.084
0.80	0.120
0.90	0.158
1.00	0.195
1.20	0.270
1.30	0.302
1.40	0.338
1.50	0.372
1.60	0.392
1.70	0.408
1.80	0.418
1.90	0.427
2.00	0.433
2.15	0.428
2.25	0.415
2.35	0.396
2.50	0.351
2.75	0.244
3.00	0.095

9m/s	
λ [1]	C_p [1]
0.25	0.014
0.50	0.046
0.75	0.104
1.00	0.197
1.25	0.289
1.50	0.377
1.75	0.425
2.00	0.447
2.25	0.430
2.50	0.365
2.75	0.257
3.00	0.105

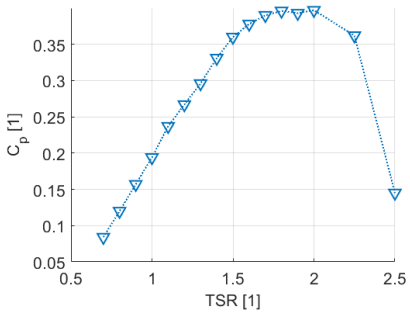

Figure B.9.: Power curve for 4m/s

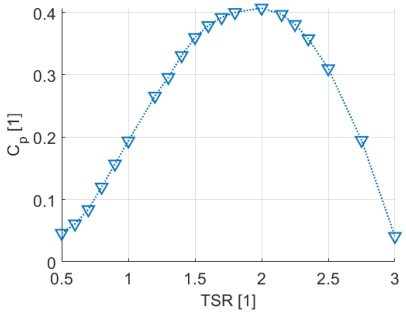

Figure B.10.: Power curve for 6m/s

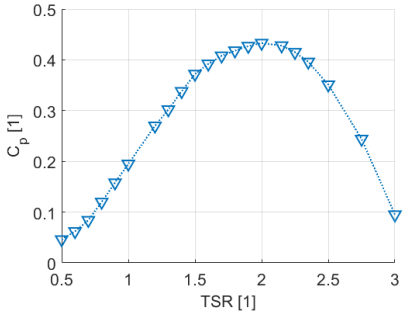

Figure B.11.: Power curve for 8m/s

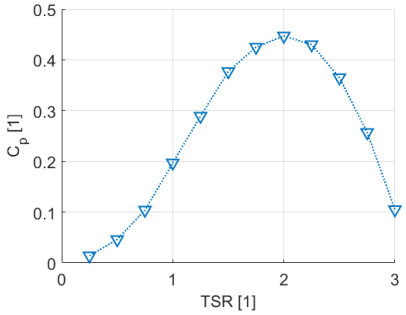

Figure B.12.: Power curve for 9m/s

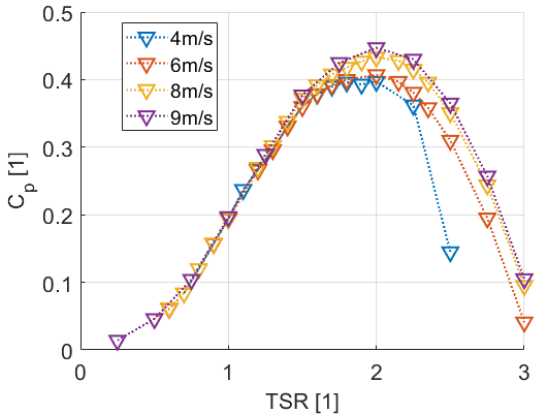

Figure B.13.: Combined results

Figure B.14.: Power curves obtained with QBlade

B.3. Comparison with wind tunnel data

4m/s		
λ [1]	C_p [1]	Relative Error [1]
0.2601	0.016	1.4845
0.2840	0.019	1.3931
0.3332	0.025	1.0970
0.3811	0.031	0.8357
0.5285	0.052	0.2001
0.5813	0.061	0.0941
0.6028	0.064	0.0871
0.8509	0.138	0.1128
1.0067	0.196	0.1770
1.0546	0.212	0.2108
1.0546	0.231	0.3529
1.0786	0.238	0.3488
1.1026	0.239	0.3878
1.1505	0.251	0.4575
1.2104	0.270	0.5954
1.2824	0.291	0.7495

6m/s		
λ [1]	C_p [1]	Relative Error [1]
0.1420	0.005	3.3265
0.1681	0.007	0.4049
0.1870	0.008	0.2444
0.2741	0.017	0.2903
0.3380	0.025	0.3161
0.4153	0.034	0.0522
0.4314	0.036	0.0469
0.5123	0.048	0.2510
0.5842	0.059	0.1861
0.6382	0.068	0.2118
0.6831	0.078	0.2026
0.7191	0.091	0.1717
0.7371	0.099	0.0875
0.8000	0.120	0.1348
0.8449	0.136	0.1186
0.8629	0.142	0.0594
0.8809	0.149	0.1075
0.8988	0.156	0.1042
0.9258	0.167	0.0823
0.9438	0.174	0.0329

8m/s		
λ [1]	C_p [1]	Relative Error [1]
0.2629	0.015	0.1851
0.3034	0.020	0.1320
0.3505	0.026	0.1075
0.3640	0.027	0.0589
0.4180	0.035	0.0613
0.4382	0.038	0.0440
0.4786	0.043	0.1004
0.5123	0.048	0.1459
0.5528	0.054	0.1952
0.5730	0.057	0.2208
0.5865	0.059	0.2549
0.6202	0.065	0.2120

10m/s		
λ [1]	C_p [1]	Relative Error [1]
0.2265	0.018	0.8187
0.2804	0.026	0.6810
0.2966	0.028	0.1817
0.3236	0.033	0.6931
0.3344	0.035	0.6648
0.3667	0.040	0.5650
0.3991	0.046	0.5265
0.4422	0.054	0.4469
0.4584	0.057	0.2464
0.4962	0.065	0.1649

C. Wind Tunnel Results

C.1. Tabulated Data

In this section the measured data, after post-processing, is reported in tabular form. The data is presented as acquired: it is not sorted by TSR, and the separation of the different test was maintained. The data was however rounded to the 4th decimal place.

4.5m/s - Test 1	
λ[1]	C_p[1]
0.0705	0.0083
0.1515	0.0125
0.1731	0.0161
0.2525	0.0330
0.3968	0.0475
0.5306	0.0809
0.7309	0.1384

4.5m/s - Test 2	
λ[1]	C_p[1]
0.7148	0.1521
1.0530	0.3779
1.0532	0.2716
1.3458	0.4217

6m/s - Test 1	
λ [1]	C_p [1]
0.0529	0.0035
0.1136	0.0053
0.1298	0.0068
0.1893	0.0139
0.2976	0.0201
0.3979	0.0341
0.5482	0.0584

6m/s - Test 2	
λ [1]	C_p [1]
0.5361	0.0642
0.7897	0.1594
0.7899	0.1146
1.0094	0.1779

6m/s - Test 3	
λ [1]	C_p [1]
0.4187	0.0363
0.4787	0.0766
0.6750	0.1465
0.6765	0.1033
0.6776	0.0911
0.7003	0.1763
0.7344	0.1161
0.8707	0.1629
0.9753	0.1839
1.0079	0.1922

8m/s		**10m/s**	
λ [1]	C_p [1]	λ [1]	C_p [1]
0.2051	0.0134	0.1811	0.0105
0.2876	0.0187	0.2546	0.0163
0.3162	0.0248	0.2676	0.0206
0.3582	0.0708	0.3048	0.0222
0.3794	0.0269	0.3279	0.0270
0.4353	0.0348	0.3408	0.0246
0.4434	0.0594	0.3408	0.0246
0.4579	0.0420	0.3523	0.0318
0.5117	0.0505	0.4161	0.0483
0.5125	0.0772	0.4161	0.0483
0.6369	0.0871	0.4463	0.0394
0.6413	0.0836	0.4553	0.0589

C.2. Standard Errors

In this section the Standard Errors are reported, first for the averaged power value used in computing C_p, then for the mean RPM value used in the first post-processing. Note that while in the main body the graphs refer to 50 standard errors, here the non-scaled value is reported in both instances.

C.2.1. Power Value

4.5m/s		
λ [1]	P [W]	SE [1]
0.2498	0.3706	0.0057
0.2573	0.3660	0.0040
0.3207	0.4587	0.0062
0.3970	0.7192	0.0039
0.4481	0.9707	0.0025
0.5024	2.4905	0.0060
0.6457	3.2051	0.0068
0.7180	3.3847	0.0067
1.0331	7.1334	0.0342
1.1742	9.4846	0.0134
1.1742	9.5716	0.0073
1.2701	10.0659	0.0052
1.2784	9.8146	0.0095
1.2943	10.1444	0.0062
1.3422	9.9007	0.0039
1.4033	9.8048	0.0032
1.4685	9.7302	0.0042
1.5577	9.5615	0.0058

6m/s		
λ [1]	P [W]	SE [1]
0.0529	0.4528	0.0057
0.1136	0.6792	0.0040
0.1298	0.8771	0.0078
0.1893	1.7954	0.0094
0.2976	2.5885	0.0180
0.3979	4.4027	0.0211
0.4187	4.6865	0.0143
0.4787	9.8802	0.0157
0.5361	8.2794	0.0141
0.5482	7.5328	0.0169
0.6750	18.9027	0.0121
0.6765	13.3309	0.0113
0.6776	11.7559	0.0140
0.7003	22.7520	0.0205
0.7344	14.9838	0.0102
0.7897	20.5728	0.0174
0.7899	14.7863	0.0122
0.8707	21.0266	0.0109
0.9753	23.7346	0.0089
1.0079	24.7992	0.0084
1.0094	22.9583	0.0087

8m/s		
λ [1]	P [W]	SE [1]
0.2051	4.0860	0.0274
0.2876	5.7047	0.0299
0.3162	7.5798	0.0279
0.3582	21.6673	0.0219
0.3794	8.2314	0.0244
0.4353	10.6474	0.0380
0.4434	18.1541	0.0178
0.4579	12.8347	0.0373
0.5117	15.4357	0.0285
0.5125	23.6208	0.0296
0.6369	26.6426	0.0269
0.6413	25.5728	0.0312

10m/s		
λ [1]	P [W]	SE [1]
0.1811	6.2550	0.0286
0.2546	9.7622	0.0365
0.2676	12.2920	0.6082
0.3048	13.2492	0.0343
0.3279	16.1253	0.0273
0.3408	14.6953	0.0708
0.3408	14.6953	0.0537
0.3523	19.0117	0.0537
0.4161	28.8546	0.0416
0.4161	28.8546	0.0333
0.4463	23.5445	0.0433
0.4553	35.2044	0.6082

C.2.2. RPM Value

4.5m/s		
λ [1]	RPM [1]	SE [1]
0.2498	18.5250	2.9581
0.2573	19.0867	2.2972
0.3207	23.7857	2.4947
0.3970	29.4427	2.1769
0.4481	33.2375	2.1413
0.5024	37.2606	3.7164
0.6457	47.8934	2.8523
0.7180	53.2514	2.0871
1.0331	76.6206	2.0427
1.1742	87.0918	6.4392
1.1742	87.0918	6.4392
1.2701	94.2058	3.0875
1.2784	94.8206	3.1077
1.2943	96.0000	4.0825
1.3422	99.5475	3.0620
1.4033	104.0816	3.1059
1.4685	108.9149	3.0671
1.5577	115.5366	3.0802

6m/s		
λ [1]	RPM [1]	SE [1]
0.0529	5.8837	2.3255
0.1136	12.6412	2.3556
0.1298	14.4444	2.6651
0.1893	21.0648	3.1950
0.2976	33.1103	2.4877
0.3979	44.2701	2.9987
0.4187	46.5824	3.0687
0.4787	53.2594	4.8035
0.5361	59.6462	6.6137
0.5482	60.9855	3.3686
0.6750	75.0945	2.4708
0.6765	75.2679	3.6367
0.6776	75.3891	3.0939
0.7003	77.9144	5.2996
0.7344	81.6993	2.8684
0.7897	87.8605	3.0821
0.7899	87.8788	4.5371
0.8707	96.8661	5.7125
0.9753	108.5100	3.0557
1.0079	112.1325	3.0713
1.0094	112.2944	3.3724

8m/s		
λ [1]	RPM [1]	SE [1]
0.2051	30.4269	3.6107
0.2876	42.6667	3.0937
0.3162	46.9043	4.4830
0.3582	53.1290	3.2088
0.3794	56.2814	3.1471
0.4353	64.5690	3.3383
0.4434	65.7762	3.0966
0.4579	67.9238	5.2035
0.5117	75.9109	6.3573
0.5125	76.0234	5.4780
0.6369	94.4771	3.1178
0.6413	95.1309	3.3171

10m/s		
λ [1]	RPM [1]	SE [1]
0.1811	33.5753	3.7336
0.2546	47.2176	3.2841
0.2676	49.6245	10.0928
0.3048	56.5107	3.6475
0.3279	60.8052	3.2371
0.3408	63.1912	4.2497
0.3408	63.1912	4.3417
0.3523	65.3333	4.3417
0.4161	77.1605	2.6019
0.4161	77.1605	3.9941
0.4463	82.7494	3.8062
0.4553	84.4278	10.0928

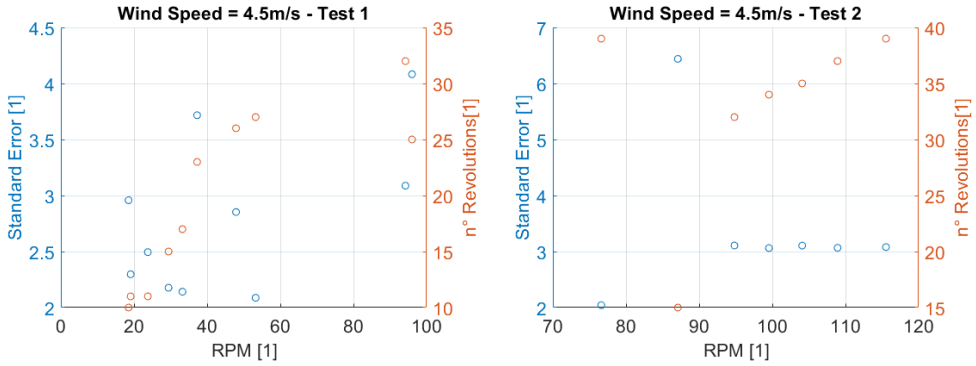

(a) Test 1 (b) Test 2

Figure C.1.: Number of revolutions and relative uncertainty for the different tests - 4.5m/s

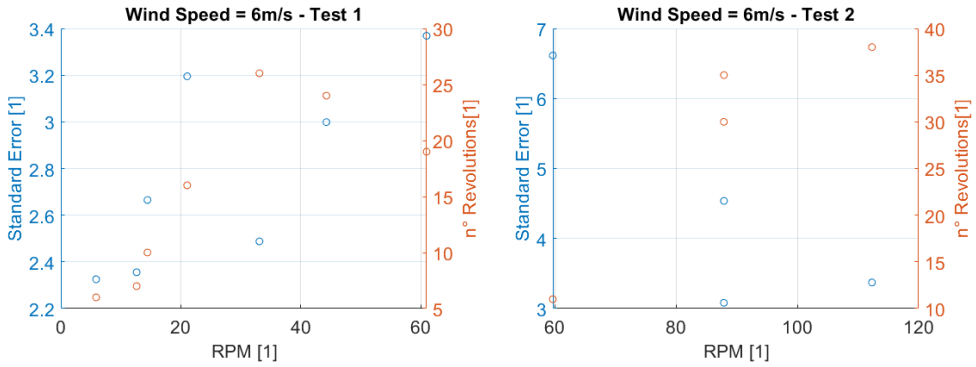

(a) Test 1 (b) Test 2

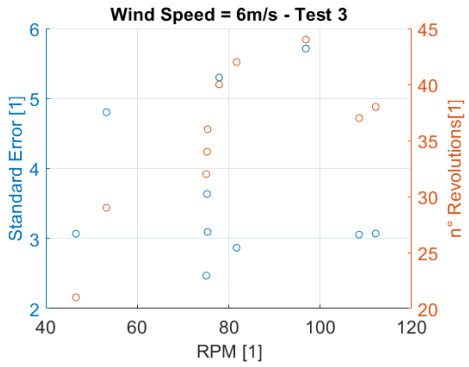

(c) Test 3

Figure C.2.: Number of revolutions and relative uncertainty for the different tests - 6m/s

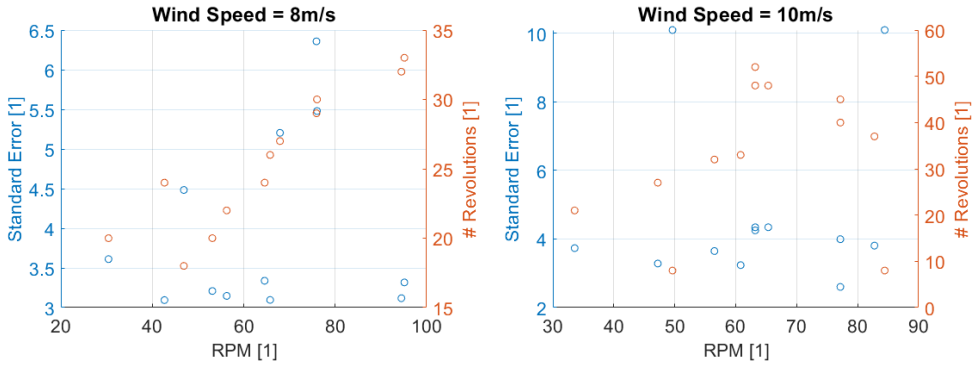

(a) 8m/s (b) 10 m/s

Figure C.3.: Number of revolutions and relative uncertainty for the different tests

C.3. Fitting Polynomials

The fitting polynomials used in section 4.3.1 are here reported. They are in the form

$$p = a_1 x^3 + a_2 x^2 + a_3 x + a_4.$$

V_w [m/s]	a_1 [1]	a_2 [1]	a_3 [1]	a_4 [1]
4.5	-0.2894	0.7901	-0.2451	0.03304
6.0	-0.4192	0.7710	-0.1836	0.01626
8.0	-2.5400	3.3010	-1.1460	0.13320
10.0	2.1120	-1.5260	0.4561	-0.03459

Bibliography

[1] Launders B.W and B.I. Sharma. "Application of the Energy Dissipation Model of Turbulence to the Calculation of Flow Near a Spinning Disc". In: *Letters in Heat and Mass Transfer* (1974).

[2] Francesco Balduzzi et al. "Critical issues in the CFD simulation of Darrieus wind turbines". In: *Renewable Energy* (2016).

[3] Galih Bangga, Steven Parkinson, and William Collier. "Development and Validation of the IAG Dynamic Stall Model in State-Space Representation for Wind Turbine Airfoils". In: *Energies* 16 (2023).

[4] Galih Bangga et al. "Improved double-multiple-streamtube approach for H-Darrieus vertical axis wind turbine computations". In: *Energy* (182 2019), pp. 673–688.

[5] Andrew Barnes, Daniel Marshall-Cross, and Ben Richard Hughes. "Towards a standard approach for future Vertical Axis Wind Turbine aerodynamics research and development". In: *Renewable and Sustainable Energy Reviews* (2021).

[6] Andrew Barnes, Daniel Marshall-Cross, and Ben Richard Hughes. "Validation and comparison of turbulence models for predicting wakes of vertical axis wind turbines". In: *Journal of Ocean Engineering adn Marine Energy* (2021).

[7] Albert Betz. *Introduction to the Theory of Flow Machines*. Pergamon Press, 1966.

[8] Marco Raciti Castelli, Alessandro Englaro, and Ernesto Benini. "The Darrieus wind turbine: Proposal for a new performance prediction model based on CFD". In: *Energy* (2011).

[9] Mohammed M. Elsakka et al. "Comparison of the Computational Fluid Dynamics Predictions of Vertical Axis Wind Turbine Performance Against Detailed Pressure Mesaurement". In: *International Journal of Renewable Energy Research* (2021).

[10] N. Franchina, G. Persico, and M. Savini. "Three-dimensional unsteady aerodynamics of a H-shaped vertical axis wind turbine over the full operating range". In: *Journal of Wind Engineering and Industrial Aerodynamics* (2020).

[11] Williams Froude. "The Elementary Relation between Pitch, Slip, and Propulsive Efficiency". In: *Inst. Naval Architects* (19 1878), p. 47.

[12] Jiao He et al. "CFD modeling of varying complexity for aerodynamic analysis of H-vertical axis wind turbines". In: *Renewable Energy* (2019).

[13] IRENA. "Renewable Energy Statistics 2024". In: *International Renewable Energy Agency* (2024).

[14] W.P. Jones and B.E. Launders. "The prediction of Lamminarization with a Two-Equation Model of Turbulence". In: *Internation Journal of Heat and Mass Transfer* (1972).

[15] A. N. Kolmogorov. "Local Structure of Turbulence in an Incompressible Viscous Fluid at Very High Reynolds Numbers". In: *Soviet Physics Uspekhi* (1941).

[16] R.B. Langtry et al. “A Correlation-Based Transition Model Using Local Variables - Part II: Test Cases and Industrial Applications”. In: *Journal of Turbomachinery* (2006).

[17] YAn Li et al. “A review on numerical simulation based on CFD technology of aerodynami characteristics of straight-bladed vertical axis wind turbines”. In: *Energy Reports* (2023).

[18] David Marten. *QBlade Guidelines v0.9*. July 2015. DOI: 10.13140/RG.2.1.3819.8882.

[19] David Marten et al. “Implementation, Optimization, and Validation of a Nonlinear Lifting Line-Free Vortex Wake Module Within the Wind Turbine Simulation Code QBLADE”. In: *Journal of Engineering for Gas Turbines and Power* (2016).

[20] F.R. Menter. “Performance of Popular Turbulence Models for Attached ans Separated Adverse Pressure gradient Flows”. In: *AIAA Journal* (1992).

[21] F.R. Menter. “Two-Equation Eddy-Viscosity Turbulence Models for Engineering Applications”. In: *AIAA Journal* (1944).

[22] F.R. Menter et al. “A Correlation-Based Transition Model Using Local Variables - Part I: Model Formulation”. In: *Journal of Turbomachinery* (2006).

[23] P.J. Moriarty and A.C. Hansen. *AeroDyn Theory Manual*. National Renewable Energy Laboratory, 2005.

[24] Stig Øye. “Dynamic stall simulated as time lag of separation”. In: *Proceedings of the 4th IEA Symposium on the Aerodynamics of Wind Turbines*. Vol. 27. 1991, p. 28.

[25] Stephan Pope. *Turbulent Flows*. Cambridge University Press, 2000.

[26] Abdolrahim Rezaeiha, Hamid Montazeri, and Bert Blocken. “On the accuracy of turbulence models for CFD simulations of vertical axis wind turbines”. In: *Energy* (2019).

[27] Abdolrahim Rezaeiha, Hamid Montazeri, and Bert Blocken. “Towards accurate CFD simulations of vertical axis wind turbines at different timp speed ratios and solidities: Guidelines for azimuthal increment, domain size and convergence”. In: *Energy Conversion and Management* (2018).

[28] P.A.C. Rocha et al. “A case study on the calibration of the k-w SST (shear stress transport) turbulence model for small scale wind turbines designed with cambered and symmetrical airfoils”. In: *Energy* (2016).

[29] P.A.C. Rocha et al. “k-w SST (shear stress transport) turbulence model calibration: A case study on small scale hrizontal axis wind turbine”. In: *Energy* (2014).

[30] H. Snel, R. Houwink, and W. J. Piers. *Sectional Prediction of 3D Effects for Separated Flow on Rotating Blades*. National Aerospace LAb., Amsterdam, 1992.

[31] G. Tescione et al. “Near wake flow analysis of a vertical axis winf turbine by stereoscopic particle image velocimetry”. In: *Renewable Energy* (2014).

[32] Larry A. Viterna and David C. Janetzke. *Theoretical and Experimental Power From Large Horizontal-Axis Wind Turbines*. National Aeronautics and Space Administration, 1982.

[33] D.C. Wilcox. “Reassessment of the Scale-Determining Equation for Advanceed Turbulence Models”. In: *AIAA Journal* (1988).

List of Figures